2022-01

Probabilistic Joint Inversion of Gravity and Magnetic Data with 3D Trans-Dimensional Earth and Noise Models

Ghaleh Noei, Emad

UNIVERSITY OF CALGARY

Probabilistic Joint Inversion of Gravity and Magnetic Data with 3D Trans-Dimensional Earth and Noise Models

by

Emad Ghaleh Noei

A THESIS
SUBMITTED TO THE FACULTY OF GRADUATE STUDIES
IN PARTIAL FULFILLMENT OF THE REQUIREMENTS FOR THE
DEGREE OF DOCTOR OF PHILOSOPHY

GRADUATE PROGRAM IN GEOMATICS ENGINEERING

CALGARY, ALBERTA
JANUARY, 2022

Abstract

Gravity and magnetic data resolve Earth models with variable spatial resolution, and Earth structure exhibits both discontinuous and gradual changes. Therefore, model parametrization complexity should address such variability, for example, by locally adapting to the spatial resolution of the data. The reversible-jump Markov chain Monte Carlo (rjMcMC) algorithm can be employed to explore Bayesian models with variable spatial resolution that is consistent with data information. To address non-uniqueness in joint inversion of potential field data, I employ novel hierarchical models that are based on irregular spatial partitioning and incorporate geological constraints about the subsurface as prior information. Spatial partitioning choices include nested Voronoi cells, linear interpolation and alpha shapes, and Voronoi cells and planes. These parametrizations partition the subsurface in terms of rock types, such as sedimentary rocks, rock salt and basement rocks. Therefore, meaningful prior information can be included in the inversion which reduces non-uniqueness. In addition, nonoverlapping prior distributions are used for density contrast and susceptibility between rock types. Another significant challenge for potential field data is unknown noise characteristics. In particular, poorly estimated noise characteristics can significantly change model spatial resolution and complexity. I consider empirical and hierarchical approaches to noise estimation that include theory and measurement errors. The empirical estimation of full data covariance matrices is based on residuals and an iterative scheme. The hierarchical approach employs a trans-D autoregressive noise model that quantifies the impact of spatial noise correlations on geophysical parameters. Both 1-D and 2-D spatial correlations are considered for 2-D and 3-D inversions, respectively. The method is applied to gravity and magnetic data to study salt and basement structures. This thesis demonstrates that meaningful partitioning of the subsurface into sediment, salt, and basement structures is achieved by these methods without requiring regularization. Multiple simulated- and field-data examples are presented. Simulation results show a clear delineation of salt and basement structures while resolving variable length scales. The field data results are consistent with observations made in the simulations. This work resolves geologically plausible structures with varying length scales and clearly differentiates salt structure and basement topography.

Preface

This is a manuscript-based thesis. The topics closely related to the research proposal were investigated in the three consecutive peer-reviewed journal papers, and based on these, this thesis is presented.

Paper I (Chapter 2 of this thesis) - published:

Ghalenoei, E., Dettmer, J., Ali, M.Y. & Kim, J.W. Gravity and magnetic joint inversion for basement and salt structures with the reversible-jump algorithm. *Geophysical Journal International*. doi:10.1093/gji/ggab251, 01 July 2021.

Paper II (Chapter 3 of this thesis) - submitted and under-review:

Ghalenoei, E., Dettmer, J., Ali, M.Y. & Kim, J.W. Joint Gravity and Magnetic Inversion with Trans-Dimensional Alpha Shape and Noise Models. under-review, 18 September 2021.

Paper III (Chapter 4 of this thesis) - submitted and under-review:

Ghalenoei, E., Dettmer, J., Y. Ali, M. & Kim, J.W. Trans-Dimensional Gravity and Magnetic Joint Inversion for 3-D Earth Models. under-review, 11 October 2021.

Acknowledgments

I would like to express my deepest gratitude to my research supervisors, Dr. Jeong Woo Kim and Dr. Jan Dettmer, for their guidance, supportive encouragement, and useful critiques of my thesis work.

I am also grateful to the members of my supervisory committee, Dr. Michael G. Sideris and Dr. Elena Rangelova, without whose knowledge and assistance this study would not have been successful. Special thanks to Dr. Mohammed Y. Ali and all internal and external examiners for sharing their knowledge and ideas.

Many thanks to the Khalifa University of Science and Technology for funding support of this project.

Finally, I would like to express my gratitude and love to my family for their constant support throughout this time.

Dedication

To my wonderful wife, Zara.

To my beloved parents and always present in my mind, Mohammad and Zahra.

Rest in peace dad, you are always loved and never forgotten.

To my siblings Mitra, Mina, and Arian.

Contents

List of Figures

List of Symbols, Abbreviations and Nomenclature

Symbol	Definition
U of C	University of Calgary
Trans-D	Trans-Dimensional
AR	Autoregressive
NV3	Nested Voronoi with 3 Parents
VP	Voronoi and Plane
LIAS	Linear Interpolation and Alpha Shape
McMC	Markov chain Monte Carlo
rjMcMC	reversible-jump Markov chain Monte Carlo
MHG	Metropolis–Hasting-Green
KNN	k-Nearest Neighbors
NN	Nearest Neighbors algorithm
PMD	Posterior Mean Distribution
PM	Posterior Mean
PPD	Posterior Probability Density
PT	Parallel Tempering
ML	Maximum Likelihood
MAP	maximum *a posteriori*
CI	Credible Interval
SGL	Sanders Geophysics Limited
TMI	Total Magnetic Intensity
DRTP	Differential-Reduced-to-the-Pole
IGRF	International Geomagnetic Reference Field
COV	Covariance
ACF	Autocorrelation Function
UP	Under-Parametrized
faiss	Facebook AI Similarity Search
OP	Over-Parametrized
MPI	Message Passing Interface
ADNOC	Abu Dhabi National Oil Company
SRTM	Shuttle Radar Topography Mission

E-W	East to West direction
N-S	North to South direction
M	Number of regular grid cells
x	Parameter defined for the location over x-axis
y	Parameter defined for the location over y-axis
z	Parameter defined for the location over z-axis
x_p, z_p	Location parameters for x and z defined for the Voronoi Parent nodes
x_c, z_c	Location parameters for x and z defined for the Voronoi Child nodes
$\Delta\rho$	Density contrast parameter
χ	Magnetic susceptibility parameter
$\boldsymbol{m}$	Model parameters
$\boldsymbol{d}$	Observed data
k	Number of nodes (e.g., Voronoi nodes or Nodes in Alpha Shapes)
$\mathbf{J}$	Jacobian matrix
$\boldsymbol{m}_k$	Trans-D model containing k nodes
$\boldsymbol{C}_d$	Data covariance matrix.
ξ	Hierarchical parameter for scaling the covariance matrix
$\boldsymbol{R}$	Correlation matrix
$\mathrm{g\ cm^{-3}}$	Unit of density contrast
mGal	Unit of gravity anomalies
nT	Unit of Magnetic anomalies
$\boldsymbol{m}^{\mathrm{AR}}$	AR model
$\boldsymbol{m}_p^{\mathrm{AR}}$	Trans-D AR model of order p
φ	AR coefficient
ε	Uncorrelated Gaussian noise
AR(0)	AR model with order 0
AR(1)	AR model with order 1
AR(2)	AR model with order 2
AR(3)	AR model with order 3
σ	Standard deviation of data-residuals
$\log_e$	Natural logarithm
N_{PT}	Number of Parallel Chains
T	Temperature value used in PT algorithm
ΔT	Temperature spacing
α	Alpha shape parameter

$\boldsymbol{m}_p^{\mathrm{2D,AR}}$	Trans-D AR model of order p for 2-D data
$\boldsymbol{ARx}$	Trans-D AR model for x direction
$\boldsymbol{ARy}$	Trans-D AR model for y direction
$\boldsymbol{ARxy}$	Trans-D AR model for xy direction

1 Introduction

Studies of dynamic processes in the Earth's interior and geophysical exploration can be aided by potential field observations, mainly gravity and magnetic, and their interpretation. Potential field studies can help understand the complexity of the Earth. Such complexity arises from the diversity in the composition of the Earth that can be described by variations of physical properties such as density and magnetic susceptibility.

Potential field methods are normally applied to study subsurface structures. Although some other geophysical methods can provide a better subsurface resolution and are increasing their role in exploring the Earth's interior, the potential field methods carry on their contribution due to providing information in deep and risky regions such as salt structures. In addition, potential field surveys are relatively cheaper and provide high quality and fine spatial resolution data.

Potential field inversions have received significant attention to date. Broadly speaking, they can provide density or magnetic susceptibility models in subsurface regions from potential field data. They can be used in different applications such as mining problems (Martinez *et al.* 2010, Kamm *et al.* 2015), crustal studies (Aitken *et al.* 2013), and exploring hydrocarbon traps (Jorgensen & Kisabeth 2000, R. Krahenbuhl & Li 2009, Silva Dias *et al.* 2011, Geng *et al.* 2020, Ghalenoei *et al.* 2021a). For example, oil and gas production is an essential need for our energy future, including the transition to low-carbon economies, causing the industry to expand its exploration in deeper water regions of the continental slope.

The principal goal of this thesis is to develop new inversion methods to permit probabilistic, nonlinear inversion of potential-field data in 3-D. To achieve this goal, I first introduce objective parametrizations for the spatial and noise models in 2-D (Chapters 2 and 3). These advances address non-uniqueness issues based on prior and data information and yield geologically plausible solutions. Finally, the resulting methods from Chapters 2 and 3 form the basis of a fully nonlinear, probabilistic method for 3-D inversion in Chapter 4.

1.1 Background of Inverse Problem

In this section, general definitions associated with geophysical inversions are introduced through the concepts of the forward problem and the inverse problem. Principle properties of the forward and inverse problems are highlighted by the key issues of *existence, uniqueness*, and *stability*.

A primary difficulty with the inversion of potential field is the inherent non-uniqueness, meaning that two different Earth models with different parameters can predict highly similar data and result in comparable data fit. The non-uniqueness arises from noisy and incomplete data and the governing physical laws.

Geophysical inversions can be viewed as the process to fit the response of a subsurface Earth model (i.e., predicted data) to noisy, incomplete observed data (Lines & Treitel 1984). The main scientific steps for the study of geophysical inverse problems can be categorized as follows (Tarantola 2005):

i. *Parametrization of the system:* Applying a parsimonious model parametrization which is consistent with data information without being overly complex. Note: A single optimal model may not be found. Rather, ensembles of models may be supported by data.

ii. *Forward modeling:* Applying physical laws (e.g., Newton's law) enables us to predict data for given values of the model parameters.

iii. *Inverse modeling:* Employ field data and the forward model to estimate the model parameters.

Predicting data for a given model and its parameter values is achieved by the mathematical formulation of physical laws. Forward problems in geophysics are generally *well-posed*, i.e., the solution exists, it is often unique, and generally stable (a small change in parameter value causes a small change in data; Pizlo, 2001).

The inverse problem is often *ill-posed* or *ill-conditioned*. In this case, a solution of the inverse problem may or may not exist, and existence depends on how well the model represents the physical system. The solution is also generally non-unique. Non-uniqueness results in two issues. First, the physics of the problem may be inherently non-unique, such as in the case of the inversion of gravity data. Second, problems in interpreting results arise since no single model can be found that explains noisy data. The non-uniqueness can be addressed by two common approaches:

i. **Construction**: Incorporating additional information or assumptions known as *prior* information or conditions, which are independent of the data (e.g., upper and lower depth limit for a salt-dome).

ii. **Uncertainty quantification**: Exploring the range of geologically acceptable models to estimate solution confidence. This is a highly popular and successful branch of Bayesian statistics and applied in my thesis.

1.2 Limitations of Current Studies

Important limitations exist in current studies that I aim to address with my research. Here, I give an overview of some shortcomings in the areas of spatial partitioning choice, treatment of correlations in data residuals, and computational burden.

First, spatial model choice in potential field inversions is often described by regular grid cells in 2-D and regular prisms in 3-D (Li & Oldenburg 1996, Boulanger & Chouteau 2001, Silva Dias *et al.* 2011, Uieda & Barbosa 2012, Martinez *et al.* 2013). These choices result in over-parametrized problems and require regularization (Li & Oldenburg 1998b, Pallero *et al.* 2017, Uieda & Barbosa 2017, Maag & Li 2018). However, global regularization parameters can mask local model features that may be crucial for interpretation purposes. In addition, the solution and its uncertainty may reflect the form of the chosen regularization (Hawkins & Sambridge 2015). In these problems, model spatial resolution is uniformly regular whereas data spatial resolution can be irregular. Therefore, irregular model partitioning can be an appropriate choice, however, it cannot be solved using linearization but requires numerical optimization and/or integration (Tarantola 2005).

Second, data measured on the Earth's surface can contain significant spatial error correlation. These correlations result in trade-offs with spatial resolution and should be included in model parametrization (Dettmer *et al.* 2007). Noise models including scale and correlation parameters are poorly studied in many potential field inversions to date. In addition, most geophysical inversions have focused on time series or 1-D spatial correlations (Bodin *et al.* 2012, Dettmer *et al.* 2012, Kolb & Lekić 2014). These methods are not able to capture spatial correlation in the 2-D data acquisition plane typical for potential-field data.

Third, considerable computational cost exists for numerical solutions to nonlinear problems (Brooks *et al.* 2011). For example, nonlinear Bayesian methods require numerical integration, where a large ensemble of posterior parameter vectors must be sampled, requiring 10^5 or 10^6 forward model evaluations. This burden can be prohibitive in 3-D inversions where a large amount of computer memory is required to store matrices and employ matrix operations.

1.3 Research Objectives

This thesis studies basement and salt structures in Ghasha oilfield located in the northwestern offshore Abu Dhabi area using high-resolution aeromagnetic and aerogravity data with 1 km griding space (Fig. 1.1). The offshore region of Abu Dhabi is particularly interesting due to the large extent and variety of salt structures in the presence of basement topography. These data reflect the composite effects of density and susceptibility changes within the basement, as well as salt diapers and the sedimentary section. Rock types of the crystalline basement are poorly known (Ali *et al.* 2017). In addition, because of thick sedimentary layers, the basement and salt have not been imaged by seismic and well data (Khattab 1995, Ali *et al.* 2017). Therefore, aeromagnetic and aerogravity data can help to study deep subsurface structures in this case study. The research objectives of this thesis are:

- Apply 3D joint gravity and magnetic inversion and demonstrate the spatial resolution of salt diapirs in the presence of basement topography and resolve both shapes and density/susceptibility values in the subsurface. Obtained models must be consistent with geological knowledge about shape, and knowledge about physical properties (density contrasts and magnetic susceptibilities). I meet these objectives by applying advanced Bayesian inference methods and by treating the inverse problem as nonlinear, without any linearization.
- I aim to overcome classical regularization requirements, such as smoothest or flattest model constraints. Instead, I will employ self-parametrized models based on irregular grids that treat the number of unknowns as unknown. These methods are commonly referred to as trans-dimensional (trans-D) models (Green 1995) and are based on Bayesian statistics. This thesis meets this objective by presenting nonlinear Bayesian inversion methods combining trans-D partitioning of space and trans-D noise models.
- Since nonlinear probabilistic 3-D inversion is a research frontier, I present novel irregular spatial partitioning (e.g., Voronoi and alpha shape) for 2-D inversions first. Then, the advantages and disadvantages of these 2-D inversions are demonstrated to form an efficient and new 3-D parametrization.
- As mentioned, trade-offs exist between spatial model resolution and noise correlation, this thesis includes the noise model to parametrization. The main objective here is to efficiently parametrize 2-D data residuals correlation in 3-D inversion.

- The computational cost for 3-D inversion is addressed by applying wavelet compression (Li & Oldenburg 2003) and parallel computing techniques.

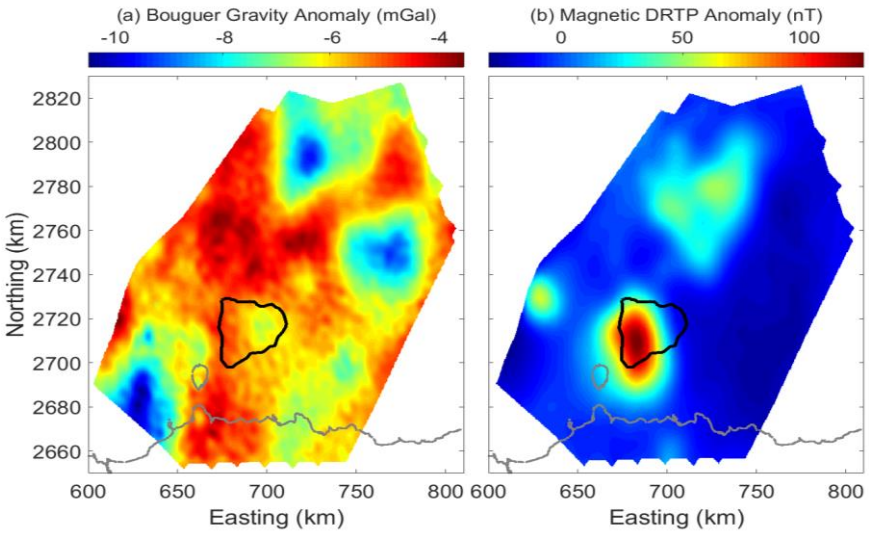

Figure 1.1. (a) Bouguer gravity anomaly, (b) magnetic DRTP anomaly. Coastlines (grey) and outlines of the Ghasha oilfield (solid black) are also shown. The map coordinates are in UTM Zone 39 N, WGS84.

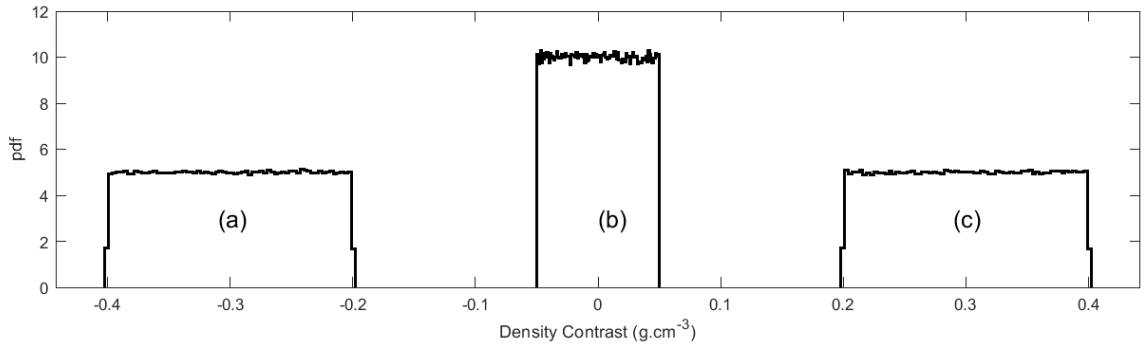

Figure 1.2. Nonoverlapping prior distributions for (a) salt, (b) sediment, and (c) the basement rock types.

1.4 Thesis Outline

In chapter 2, my thesis applies the reversible-jump Markov chain Monte Carlo (rjMcMC) algorithm that provides trans-D models with variable spatial resolution, which is consistent with data information. To address the non-uniqueness in joint inversion of potential field data, this study employs a novel spatial partitioning with nested Voronoi cells that is explored by rjMcMC sampling. The nested Voronoi parametrization partitions the subsurface in terms of rock types, such as sedimentary, salt and basement

rocks. Therefore, meaningful prior information can be specified for each type, which reduces non-uniqueness. Nonoverlapping prior distributions are applied for density contrast and susceptibility between rock types. In addition, this work adopts empirical estimation of full data covariance matrices that include theory and observational errors to account for spatially correlated noise. The method is applied to 2-D gravity and magnetic data to study salt and basement structures. This study shows that meaningful partitioning of the subsurface into sediment, salt, and basement structures is achieved by these advances without applying regularization. Multiple simulated- and field-data examples are presented. Results from multiple simulated- and field-data examples show a clear delineation of salt and basement structures while resolving variable-length scales.

In chapter 3, I present a hierarchical model that treats both spatial and data noise parametrizations as trans-D to better incorporate trade-offs between noise and structure into uncertainty quantification. This includes hierarchical spatial partitioning (LIAS) that provides advantages for the inversion of potential field data. The trans-D AR noise model quantifies the impact of correlated noise on geophysical parameter estimates. This study compares this partitioning with nested Voronoi partitioning, which shows an improvement in data fitting and parsimony of model parameters. Studies on simulated data show well-resolved structures and successful decorrelations of data residuals with a more objective and parsimonious parametrization. The inversion of field data resolves structures broadly consistent with previous studies but with improved data-fit and resolution of smaller details that are consistent with independent geological knowledge.

In chapter 4, this work presents a 3-D nonlinear Bayesian inversion with trans-D VP partitioning and trans-D estimation of the data covariance matrix. The addition of planes permits the introduction of prior information which reduces non-uniqueness. The covariance matrix estimation uses a trans-D AR noise model to quantify correlated noise on 2-D potential-field data. We address computational cost by wavelet compression in the forward problem and by basing susceptibility on an empirical relationship with density contrast. The method is applied to simulated data and field data from off-shore Abu Dhabi. With simulated data, this study demonstrates that subsurface structures are well-resolved with the trans-D model that applies hierarchical VP partitioning. In addition, the model locally adapts based on data information. The method is also successful in reducing 2-D error correlation via trans-D AR models in 2-D. From field data, the inversion efficiently resolves basement topography and two distinct salt diapirs with a parsimonious and data-driven parametrization. Results show a considerable reduction in 2-D spatial correlations of field data using the proposed trans-D AR model.

Finally, chapter 5 includes a summary of the presented methodology and results, as well as conclusions and limitations from current research and recommendations for future studies.

1.5 Statement of Contribution

This thesis takes the form of a "manuscript-based" structure. The body of the text includes a collection of three papers submitted or accepted in peer-reviewed journal publications. Therefore, each chapter contains full sections of a research paper. The author of this thesis is the main author of the papers and has done most of the writing, theoretical formalism, computational work, and programming. Dr. Jan Dettmer is a co-author who verified and supervised the methodology and results of this work. Dr. Jeong Woo Kim and Dr. Mohammed Y. Ali are also co-authors who supervised the project and contributed to the interpretation of the results. All authors provided critical feedback that helped shape the research, analysis, and manuscripts.

As a leading author of the 3 papers, my contributions include, but are not limited to, developing study ideas and study design, implementation of algorithms, application of algorithms to simulated and field data, computational analysis of results, interpretation of results.

Here, details of the co-authors' contributions are summarized:

- 1st co-author Dr. Jan Dettmer (Co-advisor): Contributed to study design, aided interpretation of results.
- 2nd co-author Dr. Mohammed Ali (Khalifa University of Science and Technology, Abu Dhabi, UAE): Provided and processed field data and aided in geological interpretation of Abu Dhabi 3-D model.
- 3rd co-author Dr. Jeong Woo Kim (Advisor): Organized a supporting project as a PI, provided and processed field data, and aided in interpretation of results.

2 Paper I: Nested Voronoi Partitioning

In this chapter, the peer-reviewed paper entitled “Gravity and magnetic joint inversion for basement and salt structures with the reversible-jump algorithm” published in *Geophysical Journal International* (DOI https://doi.org/10.1093/gji/ggab251) are presented.

This chapter studies trans-D irregular spatial partitioning using Voronoi cells to resolve basement and salt structures in 2-D joint gravity and magnetic. In addition, I adopt an empirical estimation of full data covariance matrices that include theory and observational errors to account for spatially correlated noise. This chapter demonstrates that Voronoi partitioning needs to be objectively constrained in order to provide geologically plausible solutions. This can be an essential need for the 3-D problem with higher non-uniqueness issues.

2.1 Introduction

Joint gravity and magnetic inversions are commonly applied in geophysical exploration for minerals and hydrocarbons (Pilkington 2006, Lin & Zhdanov 2018, Gross 2019, Fregoso *et al.* 2020) and can provide a better construction of subsurface models than independent inversions (Darijani *et al.* 2021). Inverting these potential field data provides quantitative information about geophysical quantities, such as density, susceptibility, and structural boundaries in the subsurface. Resolution of these quantities requires sufficient information content in the data to discern changes as a function of space. Depending on how model parameters are defined, density inversion is a linear problem when geometries of bodies are assumed known and densities are unknown, conversely, an interface inversion is a nonlinear problem where geometries of bodies are treated as unknown (Jorgensen & Kisabeth 2000, Hajian *et al.* 2012, Pallero *et al.* 2015, X. Chen *et al.* 2018, Galley *et al.* 2020). Interface inversions rely on appropriate prior information about density values for specific structures such as diapirs (R. A. Krahenbuhl & Li 2005). Most works to date apply simple geometries such as spheres, cylinders, or layered half spaces (Jiang *et al.* 2008, Hajian *et al.* 2012, Biswas 2015). A common criticism of this approach is that the specification of known density values can cause errors and biases, in particular where *in situ* measurements of density are not available (Camacho *et al.* 2000).

In contrast, density and susceptibility inversions can produce complex geometries but require constraints. In particular, due to the limited depth resolution of gravity and magnetic data and non-uniqueness issues, regularization (Li & Oldenburg 1998b, Ye *et al.* 2018, Kabirzadeh *et al.* 2019, Maag-Capriotti & Li 2019) and truncated singular value decomposition (SVD) are often applied with parameters that trade off model complexity and data misfit (Zhao & Chen 2011). These deterministic inversions typically apply regular mesh-based parametrizations and minimize objective functions including a data misfit and model-objective or regularized terms (Lelièvre *et al.* 2019).

Nonlinear Bayesian inference has received increasing attention since it addresses some limitations of deterministic inversions. In Bayesian inference, prior information represents information about parameters that is independent from data information. Bayes' theorem (Bayes & Price 1763) is applied to update prior information with data information (Tarantola 2005). In Bayesian approaches, model parameters are treated as random variables and probabilities are interpreted as degrees of belief (Jaynes 2003). In this framework, nonlinear inverse problems can be solved by employing numerical sampling such as Markov chain Monte Carlo (McMC) methods. In Bayesian inversion, the solution to the inverse problem is given by the posterior probability density, typically a high-dimensional distribution. Bayesian gravity and magnetic inversions often apply regular prism parametrizations with constraints (e.g., Barnoud *et al.* 2019, Fregoso *et al.* 2020, Hightower *et al.* 2020). However, theoretical considerations for Bayesian inference show that results depend strongly on model parametrization choice. Fortuitously, objective choices can be made to overcome this subjectivity (MacKay 2003). In practice, model choices include the types of spatial partitioning (Sambridge *et al.* 2006a) or basis functions (Hawkins & Sambridge 2015). These approaches are commonly referred to as self parametrized.

Fixed regular grids typically require an over-parametrized model, where discretization is chosen to be below the data spatial resolution and regularization is applied to avoid over-fitting. Self-parametrized models can treat the number of unknowns as unknown, which is referred to as trans-dimensional (trans-D) models (Green 1995). The most common algorithm to study trans-D models is the reversible jump McMC algorithm (rjMcMC; Green, 1995; M. Sambridge et al., 2006). The rjMcMC algorithm was introduced to geophysical problems to invert zero-offset vertical seismic profiles (Malinverno 2002). A trans-D model was applied to gravity inversion (Luo 2010) with the particularly interesting approach of parametrizing density by trans-D polygons in two spatial dimensions, where the number of sides in the polygon is treated as unknown. This approach assumed that density values of the areas inside and outside the polygon are known.

Model parametrizations with variable numbers of Voronoi cells (Voronoi 1908) have been considered widely in geophysical inversion (e.g., Bodin *et al.* 2009, Dettmer *et al.* 2014, Ray *et al.* 2014, Galetti & Curtis 2018). However, we demonstrate that these are insufficient for potential field data, likely due to non-uniqueness issues and limited data information. We overcome this limitation by employing a novel trans-D model consisting of nested Voronoi cells that efficiently parametrizes typical diapir environments consisting of three rock types: sedimentary rocks, rock salt and basement rocks. The algorithm produces continuous rock units of simple shape with plausible depths that include both sharp and smooth transitions between units without the need to apply constraints and regularization. While posterior models are smooth, the smoothness is constrained directly by data information without the requirement to specify smoothing. In addition, the model can spatially adapt the parametrization to the data information so that structures of different length scales can be resolved. In addition to inferring the geometry of structures, this method also considers unknown but distinct density contrasts and susceptibilities of the three rock types. The coupling of parameters assumes that density contrast and susceptibility share structural boundaries. In the nonlinear parametrization, this is simply achieved by populating each Voronoi node with a parameter for density contrast and one for susceptibility. Finally, data noise is estimated in an empirical fashion and accounts for the full data covariance matrix for both gravity and magnetic data. The method is applied to simulated and field data. The field data are from aerogravity and aeromagnetic surveys collected in Abu Dhabi, United Arab Emirates (UAE). The offshore region of Abu Dhabi is particularly interesting due to the large extent and variety of salt structures in the presence of basement topography. We carry out the joint inversion over the Ghasha oilfield and demonstrate resolution of basement and salt diapirs with geologically plausible depths, shapes and physical properties (density contrasts and susceptibilities).

2.2 Geological Setting

Understanding of salt tectonics and the resulting structures plays a critical role for this study. Salt structures that originate in salt basins can harbour large hydrocarbon reservoirs (Jackson & Hudec 2017) but are also important tectonic structures in many sedimentary basins and crucial to the understanding of lithospheric evolution (McKenzie 1978, Hudec & Jackson 2007). Salt is an example of a rock that can undergo ductile deformation and flow due to gravity, its relatively low density (2.02-2.360 $\mathrm{g\ cm^{-3}}$), and low yield strength (Talbot & Jackson 1987). Salt flow is able to extrude from an original tabular formation into a large variety of salt structures, including salt diapirs, which intrude the overburden (O'Brien 1968) and can be exhumed in some cases. Such intrusions are typical for offshore Abu Dhabi, where some salt

structures are exhumed (Ali *et al.* 2017). Due to the abundance of diapir structures, the Abu Dhabi region is an ideal area to study advanced inversion methods to resolve salt structures.

The majority of rocks in diapirs in this region are from the Hormuz Complex with a clay-rich matrix that includes a variety of unusual clasts such as igneous, sedimentary and low-grade metamorphic rocks of the Arabian basement. These inclusions have been delivered to shallower depths from their origin that is deeper than 8 km (Thomas *et al.* 2015).

The basement of a salt basin is also important for hydrocarbon exploration since it can protrude into the overlying sedimentary rocks and affect the shapes of hydrocarbon traps and fluid flows (Hodgson 1965). In addition, the basement structure is part of tectonic processes that governs the basin architecture and alters source rock distributions, heat flows, trap timing, and sediment supplies (Palumbo *et al.* 1999). Therefore, it is critical to improve our understanding of basin tectonics to ultimately identify prospects and gain insight into optimal well sites.

The basement in the region was formed as part of the Neoproterozoic compression (from ~715 to ~610 Ma) of island-arc and microcontinent terrane accretion that created the Arabian margin of Gondwana (Al-Husseini 2000). This magnetized basement is overlain by ~8-10 km of Late Neoproterozoic to Phanerozoic sedimentary sequences (Ali *et al.* 2017). Surprisingly, little is known about the rock types of the crystalline basement. In addition, due to the thick sedimentary cover, the basement has not been imaged by seismic and well data. The basement is modeled to be deeper than about 8.5 km by regional magnetic survey data (Khattab 1995, Ali *et al.* 2017).

Offshore oilfields in Abu Dhabi were created in the Late Cretaceous by a compressional event, which was caused by the obduction of the Semail Ophiolite (Ali & Farid 2016). The compressional event caused regional stress, which mobilized Infracambrian Hormuz salt structures, folding of sedimentary layers, and created anticlinal oilfields. Subsequent lesser structural developments appeared during the Neogene.

2.3 Potential Field Data

The airborne gravity survey was carried out by Sanders Geophysics Limited (SGL) for ADNOC in 2007–2008. The data consists of 13,804 line km measured predominantly offshore Abu Dhabi at 250 m above sea level with 2-km line spacing and 10-km spacing of tie lines (Ali *et al.* 2017). Data processing included Eötvös, latitude, free air, Bouguer, curvature of the Earth, terrain, static, and levelling corrections with respect to the mean sea level. The terrain correction over land was applied assuming a density of 2.6

$\mathrm{g\,cm^{-3}}$ utilizing terrain-topographic data obtained from the Shuttle Radar Topography Mission. The seawater-depth correction was applied with a density of 1.02 $\mathrm{g\,cm^{-3}}$ over marine regions using bathymetric data taken from the Gridded Bathymetric Chart of the Oceans 1-minute grid. Long-wavelength regional effects were removed by applying a low-pass filter (3-km half-wavelength) and an upward continuation at 20-km elevation. This approximately removes the effect of sources below 10-km. Finally, data were provided on a regular grid with a cell size of 1 km. These data represent the total gravity effects of the basement and overlying structures including salt deposits and sediment strata.

Similarly, the total magnetic intensity (TMI) aeromagnetic data were acquired by SGL for ADNOC concurrent with the airborne gravity survey using Caesium optically pumped magnetometers with a sensitivity of 0.001 nT (1 Tesla = $\mathrm{kgs^{-2}A^{-1}}$) and sensor noise of 0.02 nT. Initially, International Geomagnetic Reference Field (IGRF) values were subtracted from the measured data. The TMI data processing included artifacts eliminations, correction of leveling errors, and base-station reductions which decrease diurnal variations (Salem & Ali 2016). Finally, the TMI data were transformed by differential reduced-to-the-pole (DRTP) to minimize inclination effects. The DRTP transform reduces magnetic anomalies to the pole by correcting regional variations in the inclination and declination. The DRTP data show symmetric anomalies centered on their causative structures, with no significant remanence in the magnetic anomaly, implying that all magnetization is induced (Arkani-Hamed 2006). The symmetric DRTP data can aid interpretation in terms of geological structures and have been previously used in magnetic inversions over the case study of this work (Geng *et al.* 2020).

2.4 Methodology

2.4.1 2-D Gravity and Magnetic Forward Models

We predict gravity anomaly data with a 2-D parametrization of M rectangular blocks with centers (x_j, z_j), horizontal and vertical dimensions of w and h, respectively, and density contrast values. The forward model is

$$\mathrm{dg}_i^{\mathrm{pre}} = \sum_{j=1}^{M} G_{i,j}^{g}\,\Delta\rho_j, \qquad i = 1,2,\dots,N \tag{2.1}$$

where $\mathrm{dg}_i^{\mathrm{pre}}$ are gravity predicted data at station i, $G_{i,j}^{g}$ is the gravity kernel of the jth grid cell and the ith datum, and $\Delta\rho_j$ is the density contrast ($\rho_j - 2.6\ \mathrm{g\,cm^{-3}}$) of the jth grid cell. Details are found elsewhere

(e.g., Last & Kubik, 1983). Magnetic predicted data $\mathrm{dT}_i^{\mathrm{pre}}$ are computed in an analog fashion for susceptibilities χ_j, and the magnetic kernel $G_{i,j}^{T}$ (Telford *et al.* 1990, Hinze *et al.* 2013). Details can be found in the Appendix A.

2.4.2 Bayesian Inference with Trans-D Models

Let $\boldsymbol{m}$ be a vector containing M model parameters (e.g., density contrast values and grid-node locations) and $\boldsymbol{d}$ a vector containing N data observations (e.g., gravity anomaly values in space). Bayes' rule (Bayes & Price 1763, Jaynes 2003) can be written

$$P(\boldsymbol{m}|\boldsymbol{d}) = \frac{P(\boldsymbol{d}|\boldsymbol{m})\,P(\boldsymbol{m})}{P(\boldsymbol{d})}, \tag{2.2}$$

where $\boldsymbol{m} \in \mathcal{R}^M$ and $\boldsymbol{d} \in \mathcal{R}^N$ are random variables. The posterior probability density (PPD) is $P(\boldsymbol{m}|\boldsymbol{d})$, $P(\boldsymbol{d}|\boldsymbol{m})$ is the likelihood function, hereafter abbreviated as $\mathcal{L}(\boldsymbol{m})$, $P(\boldsymbol{m})$ is the prior distribution, and the normalizing constant $P(\boldsymbol{d})$ can be ignored for the parameter inference considered here (e.g., Sambridge *et al.* 2006). Equation (2.2) represents how prior information about model parameters is updated by data information. Numerical approaches using McMC sampling (Gilks *et al.* 1995, David G. T. Denison *et al.* 2002, Sambridge & Mosegaard 2002, Brooks *et al.* 2011) are often applied to estimate the PPD in Bayesian inversion. McMC methods have been applied to many geophysical data, including geoacoustic data (Belcourt *et al.* 2020), resistivity data (Galetti & Curtis 2018), seismic data (Ray *et al.* 2018), fault rupture data (Shi *et al.* 2018, Amey *et al.* 2019), and gravity and magnetic data (Bosch *et al.* 2006). McMC sampling generates a sequence (chain) of models called samples. Each new sample ($\boldsymbol{m}'$) is based on a perturbation of the current sample ($\boldsymbol{m}$). Perturbations are generated by a proposal distribution $Q(\boldsymbol{m}'|\boldsymbol{m})$ that only depends on $\boldsymbol{m}$. In practice, the chain includes two periods. The initial burn-in period represents a non-stationary random walk and is associated with finding regions of high probability in the model space. Subsequently, the sampling period records models that represent a stationary random walk through high probability regions of the model space. The burn-in is discarded and inferences are based on the posterior sampling period. Estimates obtained from the sample include the posterior mean model, marginal distribution, and credible intervals.

Importantly, use of Eq. (2.2) for geophysical inversion requires the formulation of a forward model which includes a choice of parametrization for the Earth and data noise, and various assumptions about the physics used to describe the Earth's response. This model specification is subjective and inversion results

can depend strongly on these choices. To reduce subjective assumptions, Bayesian model selection (MacKay 2003) can be applied. A trans-D model is one approach to including model selection in the inverse problem. The trans-D framework causes natural parsimony (avoiding under and/or over-parametrized models) by employing a hierarchical model in terms of indexing parameter k. This index can be used to include multiple model choices in the inversion, e.g., the number of layers or nodes in an Earth model. Bayes' theorem for trans-D models is

$$P(\boldsymbol{m}_k, k|\boldsymbol{d}) = \frac{P(\boldsymbol{d}|\boldsymbol{m}_k, k)\, P(\boldsymbol{m}_k|k)P(k)}{\sum_{k' \in K} \int_{\mathcal{M}_k} P(\boldsymbol{d}|\boldsymbol{m'}_{k'}, k')\, P(\boldsymbol{m'}_{k'}|k')P(k')d\boldsymbol{m'}_{k'}} \quad , \tag{2.3}$$

where K is a countable set of model choices, $k \in K$ indexes possible choices of models, $P(k)$ is the prior over the K models to be considered and the integration is over the state space $\mathcal{M}_k$. Such models can be sampled by the rjMcMC algorithm (Green 1995). The rjMcMC algorithm can *jump* between various indexed models ($\boldsymbol{m}_k$) and provides samples from the joint distribution of parameters for various k. Jumps must satisfy detailed balance which is achieved by the Metropolis–Hasting-Green (MHG) algorithm (Metropolis et al., 1953; Hastings, 1970; Green, 1995). The MHG algorithm provides an acceptance probability, $\alpha(\boldsymbol{m'}_{k'}|\boldsymbol{m}_k)$, for a step from the current model $(k, \boldsymbol{m}_k)$ to a proposed model $(k', \boldsymbol{m'}_{k'})$. To accept the proposed model, a random number r on [0, 1] is generated. If $r \leq \alpha(\boldsymbol{m'}_{k'}|\boldsymbol{m}_k)$, the proposed model ($\boldsymbol{m'}_{k'}$) is accepted, otherwise it is rejected, and the current model ($\boldsymbol{m}_k$) is recorded again. The acceptance probability is expressed as

$$\alpha(\boldsymbol{m'}_{k'}|\boldsymbol{m}_k) = \min\left[1, \frac{P(\boldsymbol{m'}_{k'})}{P(\boldsymbol{m}_k)} \times \frac{\mathcal{L}(\boldsymbol{m'}_{k'})}{\mathcal{L}(\boldsymbol{m}_k)} \times \frac{Q(\boldsymbol{m}_k|\boldsymbol{m'}_{k'})}{Q(\boldsymbol{m'}_{k'}|\boldsymbol{m}_k)} \times |\mathbf{J}|\right], \tag{2.4}$$

where the product shows, from left to right, the prior ratio, the likelihood ratio, and the proposal ratio. The term $|\mathbf{J}|$ is the determinant of the Jacobian matrix for a transformation from $\boldsymbol{m}_k$ to $\boldsymbol{m'}_{k'}$. Appendix B shows that $|\mathbf{J}| = 1$ for the cases considered here.

2.4.3 Simple Voronoi Partitioning

Forward models are straightforward to formulate for gravity and magnetic inversions when density contrasts and susceptibilities are given on regular grids. However, the spatial resolution of geophysical parameters in the subsurface is generally not uniform or regular. This issue is often addressed by choosing a grid spacing that is much smaller than the expected length scales resolved by the data. Such spacing leads to over-parametrized models, that is, models that include many more parameters than can be

resolved by the data. To avoid conditioning issues in the inverse problem, regularization or other forms of stabilizing the problem are commonly applied (Oldenburg & Li 1994, Farquharson & Oldenburg 1998, Farquharson *et al.* 2008, Menke 2012, Sun & Li 2014, Aster *et al.* 2016, Fournier & Oldenburg 2019). These approaches are computationally efficient for linear and linearized problems but have limitations such as the same model smoothness being applied throughout the region of study.

Unstructured meshes have been applied to many geophysical problems including triangular 2-D and tetrahedral 3-D meshes (Stenerud *et al.* 2009, Lelièvre & Farquharson 2013), and inversion of resistivity data with unstructured tetrahedral meshes (Rücker *et al.* 2006). Irregular grids (Sambridge *et al.* 1995) have been proposed to more objectively describe geophysical parameters and to overcome some limitations of regularization (Bodin *et al.* 2009) at the cost of additional computational burden due to required numerical sampling caused by the parametrization. The irregular resolution of parameters is closely linked to the non-uniqueness of inverse problems which stems from the incomplete and noisy nature of data. One practical implementation of irregular grids is to partition space with Voronoi cells and associate parameters (density contrast and/or susceptibility) with the cells. In its simplest form, Voronoi cells apply nearest neighbour partitioning and partition an underlying regular grid, with fine grid spacing, that is convenient for computing data predictions.

A further generalization of irregular grids can be achieved by trans-D Voronoi partitioning (Bodin & Sambridge 2009), where the number (k) of Voronoi nodes is treated as unknown. This simple Voronoi partitioning is efficient for 2-D parametrizations, requiring far fewer Voronoi nodes compared to regular grid nodes to describe typical geophysical models. This is because a small number of nodes can model regions with little variability in geophysical parameters.

In our application, irregular Voronoi cells are efficiently mapped to regular grids by the k-nearest neighbors (KNN) algorithm (Fix & Hodges 1989, Altman 1992) for conveniently solving the forward model, Eq. (2.1). In this procedure, we compute the gravity and magnetic kernels only once for the regular grid and then store them for forward modeling. Hence, there is no need to compute kernels for irregular Voronoi cells.

However, this simple trans-D Voronoi partitioning does not provide reasonable results for diapirs in the presence of basement topography. Issue arises from poor depth sensitivity of gravity and magnetic kernels, and non-uniqueness. We will demonstrate that spurious structures often arise for simple Voronoi partitioning. For example, rock-salt densities may be incorrectly imaged below the basement.

2.4.4 Nested Voronoi Partitioning

We overcome limitations of simple Voronoi partitioning by employing two levels of partitioning for 2-D inversion of potential field data: k Voronoi *child nodes* of a trans-D model are partitioned by three Voronoi *parent nodes*. Parent nodes represent rock types: basin rocks, rock salt, and basement rocks. The number of parent nodes is fixed to three but their positions are unknown and constrained by data. Child nodes can be added, deleted, and moved. Hence, the number and positions of child nodes are constrained by data. Child nodes are assigned rock types (i.e., density contrast and susceptibility) by the parent nodes using a nearest-neighbor algorithm (e.g., KNN). This nested Voronoi parametrization produces partitioning of the model space in terms of sediments, salt, and the basement, with geologically plausible geometries based on data. In addition, the trans-D child nodes adapt the discretization based on data information. In total, the parametrization includes 6 coordinate parameters for the three parent nodes and $[x, z, \Delta\rho, \chi]$ for each child node, resulting in $6 + 4k$ parameters. Since $\Delta\rho$ and χ are assigned to each child node, both density contrast and susceptibility models have the same spatial partitioning. We apply MHG sampling for this parametrization with three types of proposals:

(i) Adding a Voronoi child node to the current model.

(ii) Deleting a Voronoi child node that is randomly chosen from the current model.

(iii) A parameter is chosen (uniformly random, considering all Voronoi nodes) and perturbed by a Cauchy proposal distribution (N. L. Johnson *et al.* 1995), which is similar to a Gaussian distribution near the mean but includes heavier tails for occasional large steps (Beaty *et al.* 2002).

It is important to set the same probability for choosing proposal types (i) and (ii). Here, the three types are assigned equal probability of 1/3. When $k = k^{\min}$, probabilities are 1/3 for (i) and 0 for (ii), and 2/3 for (iii). When $k = k^{\max}$, (i) has 0 probability, (ii) has 1/3, and (iii) 2/3.

Prior distributions in this study are bounded and uniform. A reasonable choice for prior width, which is the difference between the upper or lower bounds, is important but generally not difficult: If chosen wide, the acceptance of new Voronoi child nodes is reduced, if chosen narrow, the posterior distribution of the solution may be truncated. A reasonable trade-off is typically straightforward to find empirically. Note that we set prior distributions as nonoverlapping uniform distribution for each of the three rock types which aids in resolving compact structures and reduces non-uniqueness. Subscripts p and c refer to parent and child nodes, respectively. The p nodes index the rock types as $p = 1$ for sediment, $p = 2$ for

salt, and $p = 3$ for the basement. Defining model parameters as $(\boldsymbol{m}_k, k) = \{\boldsymbol{x}_p, \boldsymbol{z}_p, \boldsymbol{x}_c, \boldsymbol{z}_c, \boldsymbol{\chi}_c, \boldsymbol{\Delta\rho}_c, k\}$, and using the chain rule, the prior is written

$$P(\boldsymbol{m}_k, k) = P(\boldsymbol{x}_p, \boldsymbol{z}_p)\, P(\boldsymbol{x}_c, \boldsymbol{z}_c|k)\, P(\boldsymbol{\chi}_c|k) P(\boldsymbol{\Delta\rho}_c|k)\, P(k), \tag{2.5}$$

where $P(k)$ is the uniform prior distribution for index k

$$P(k) = \begin{cases} \dfrac{1}{k^{\max} - k^{\min} + 1} = \dfrac{1}{\Delta k} & \text{if } k^{\min} \le k \le k^{\max} \\ 0 & \text{else} \end{cases}, \tag{2.6}$$

where superscripts min and max represent the lower and upper bounds of the uniform distribution. Prior distributions $P(\boldsymbol{\Delta\rho}_c|k)$ and $P(\boldsymbol{\chi}_c|k)$ are for density contrast and susceptibility of child nodes, given the number of child nodes k, respectively. When temporarily assuming the numbers of child nodes in sediment, salt, and the basement to be k_1, k_2, and k_3 , respectively, with $k = k_1 + k_2 + k_3$, then

$$P(\boldsymbol{\Delta\rho}_c|k) = \begin{cases} (\Delta\rho_1)^{-k_1}(\Delta\rho_2)^{-k_2}(\Delta\rho_3)^{-k_3} & \text{if } \Delta\rho^{\min} \le \Delta\rho_c \le \Delta\rho^{\max} \\ 0 & \text{else} \end{cases}, \tag{2.7}$$

where $\Delta\rho_1, \Delta\rho_2$, and $\Delta\rho_3$ are the widths of uniform prior distributions for density contrasts in sediment, salt, and basement, respectively. Similarly, for the susceptibility we have

$$P(\boldsymbol{\chi}_c|k) = \begin{cases} (\Delta\chi_1)^{-k_1}(\Delta\chi_2)^{-k_2}(\Delta\chi_3)^{-k_3} & \text{if } \Delta\chi^{\min} \le \chi_c \le \Delta\chi^{\max} \\ 0 & \text{else} \end{cases}, \tag{2.8}$$

where $\Delta\chi_i$ represent the widths of uniform susceptibility priors of sediment, salt, and basement. The prior $P(\boldsymbol{x}_p, \boldsymbol{z}_p)$ is for the positions of parent nodes. We temporarily assuming that a 2-D regular grid space consists of M rectangular blocks (Bodin & Sambridge 2009), which leads to

$$P(\boldsymbol{x}_p, \boldsymbol{z}_p) = \frac{1}{\binom{M}{3}}, \tag{2.9}$$

where $\binom{M}{3}$ is 3-combination of M. The prior $P(\boldsymbol{x}_c, \boldsymbol{z}_c|k)$ is for the positions of k Voronoi child nodes,

$$P(\boldsymbol{x}_c, \boldsymbol{z}_c|k) = \frac{1}{\binom{M}{k}}. \tag{2.10}$$

Combining Eq. (2.6) to (2.10), in Eq. (2.5) results in

$$P(\boldsymbol{m}_k) = \frac{(\Delta\rho_1\Delta\chi_1)^{-k_1}(\Delta\rho_2\Delta\chi_2)^{-k_2}(\Delta\rho_3\Delta\chi_3)^{-k_3}}{(\Delta k)\binom{M}{3}\binom{M}{k}}. \tag{2.11}$$

Appendix B shows that the regular grid assumption (M) cancels and the inversion becomes independent of this temporary assumption. It also shows that prior and proposal ratios in Eq. (2.4) cancel. Therefore, the acceptance probability for all moves in the MHG algorithm simplifies to the likelihood ratio in our specific case.

2.4.5 Likelihood Function and Data Errors

The likelihood function $P(\boldsymbol{d}|\boldsymbol{m}_k, k)$, abbreviated as $\mathcal{L}(\boldsymbol{m}_k)$, describes the data-error statistics. Formulating a likelihood function requires making assumptions about data noise. A common assumption supported by the central limit theorem is that noise is Gaussian distributed. Such assumptions should be tested quantitatively to examine their validity (Dettmer *et al.* 2007). Assuming Gaussian-distributed noise leads to

$$\mathcal{L}(\boldsymbol{m}_k) = \frac{1}{\sqrt{(2\pi)^N|\boldsymbol{C}_d|}}\exp\left(-\frac{1}{2}\boldsymbol{r}^T\boldsymbol{C}_d^{-1}\boldsymbol{r}\right), \tag{2.12}$$

where N is the number of data, $\boldsymbol{r} = \boldsymbol{d}^{\text{obs}} - \boldsymbol{d}(\boldsymbol{m}_k)$ are the data residuals, and $\boldsymbol{C}_d$ is the data covariance matrix. To ensure numerical stability when evaluating Eq. (2.12), its logarithm is generally evaluated.

The likelihood function plays a critical role in McMC sampling since it contains both data residuals ($\boldsymbol{r}$) and assumptions about their statistics ($\boldsymbol{C}_d$). Data residual errors contain both measurement errors (e.g., ambient noise, instrument noise) and theory errors due to model assumptions or simplifications (e.g., 1-D or 2-D models, idealized physics) and the two often cannot be separated in practice. Hence, the specific form of residual-error distribution is unknown and we estimate it here during the inversion (Dettmer et

al., 2007). Although simplifying assumptions are often applied, we estimate the full covariance matrix including covariances from the residual errors. Covariances are particularly important for potential field data with high spatial sampling and long signal wavelengths.

This work estimates $\boldsymbol{C}_d$ iteratively in three phases (Dettmer *et al.* 2007): Phase 1 applies rjMcMC sampling assuming uncorrelated errors of unknown standard deviation. This phase is not used for posterior estimation but provides residuals to compute an initial estimate of the covariance matrix. Phase 2 applies the covariance matrix from phase 1 and updates it periodically (e.g., every 1000 rjMcMC steps) until $\boldsymbol{C}_d$ converges. Note that $\boldsymbol{C}_d$ is computed from a maximum likelihood model that may not be representative for all members of the trans-D model in the whole inversion but is taken from the most probable subspace indexed by *k*. Therefore, $\boldsymbol{C}_d$ is scaled by a hierarchical parameter (ξ) for each chain (Dettmer *et al.* 2014). We apply a uniform prior for ξ with lower and upper bounds of 1 and 10, respectively. We conservatively choose the lower bound of 1 to not diminish the initial covariance estimate. It is also important to examine the residual errors *a posteriori* by standardizing with the Cholesky decomposition of the covariance estimate (standardized residuals). Phase 3 applies the converged covariance estimate from phase 2 without further changes but permits scaling by ξ. Here, sampling ensues. Phases 1 and 2 are considered as burn-in and samples are not retained for inference.

For joint gravity and magnetic inversion, Eq. (2.12) is applied for gravity and magnetic data. The joint likelihood, assuming independent noise between data sets, is given by the product of the gravity and magnetic terms. Importantly, no data weights are subjectively assigned. Rather, the weights are provided by the $\boldsymbol{C}_d$ estimates for each data type which are based on data information. Appendix C shows a simple simulation to validate the correctness of the algorithm.

2.5 Simulation Study

This section considers simulated data for 2-D models consisting of sediments, salt, and basement. The models are on grids of 100 by 103 regular cells in the x and z directions, respectively, corresponding to cell areas of 800 by 100 m. In the true model, two distinct positive density contrasts and two distinct susceptibility values exist in the basement. Salt structures include a sharp and a wide geometry with two distinct negative density contrasts. Sediments and salt regions are assumed to have susceptibilities of zero. Note that the true model is intentionally not generated by a Voronoi diagram and cannot be exactly represented by the model parametrization, which introduces theory errors. We employ this discrepancy to show the ability of the algorithm to study realistic structures that are unlikely representable exactly by Voronoi cells.

Data are contaminated by correlated zero-mean Gaussian noise with a standard deviation of 4% of the maximum of the true gravity data and 1% of the true magnetic data. True covariance matrices were constructed from a Toeplitz correlation matrix ($\boldsymbol{R}$) with diagonal scaling from 1 to nearly zero based on an attenuated cosine. This $\boldsymbol{R}$ was multiplied by σ^2 to obtain the true covariance matrix.

Prior distributions for the density contrast of rock salt and basement rocks are uniform over $(-0.4, -0.03)$ g cm^{-3}, and $(0.1\ , 0.5)$ g cm^{-3}, respectively. The susceptibility prior of basement rocks is uniform between 0.004 and 0.008 SI. The sediment density contrast and susceptibility, and the rock salt susceptibility are assumed to be zero. The sensitivity of inversion results with respect to prior choice is considered in the Appendix D for a narrower rock salt prior of $(-0.4, -0.15)$ g cm^{-3}.

The inversion is initialized with a random model from the prior distribution. Parallel tempering (PT, Geyer 1991, Dettmer & Dosso 2012, Sambridge 2014) was applied with 12 chains including 4 chains at $T = 1$, and a temperature spacing of $\Delta T = 1.2$. Acceptance swap rates between neighboring chains were monitored and showed an acceptable range of 40% to 60%. The full covariance matrices for gravity and magnetic data ($\boldsymbol{C}_d^{\mathrm{g}}$ and $\boldsymbol{C}_d^{\mathrm{T}}$) were estimated by 3 iterations which each consist of 1000 rjMcMC steps. Convergence was examined by monitoring the difference of posterior mean models for the first and last 1/3 of recorded models (Dettmer *et al.* 2014). When these two estimates are within a pre-defined threshold, the inversion is deemed to have converged (Appendix E). The sampling produced 80,000 samples once convergence was achieved.

The observed data are well fit by the predictions (Fig. 2.1-a and b) without signs of over- and under-fitting. The number of child nodes required by the data represents model complexity and peaks at 25 nodes (Fig. 2.1-c). This low number illustrates parametrization efficiency in comparison to regular-grid parametrizations. However, Fig. 2.1-c also quantifies uncertainty to be between 15 and 45 nodes, a manifestation of non-uniqueness and that the data cannot resolve the true model precisely.

Inversion results are shown in terms of posterior mean models and widths of 95% credibility intervals (CI) in Fig. 2.2. For reference, Fig. 2.2-a shows the true model. Figure 2.2-b shows results for the simple Voronoi parametrization and these poorly represent the true model. Specifically, the wide salt structure in the east is not captured well and the basement at x~60 km appears implausible with low-density rock appearing beneath a sliver of basement rock. Contrarily, the nested Voronoi parametrization produces posterior mean models that resolve the true model reasonably well, albeit without the sharp discontinuities (Fig. 2.2-c and g). Main features are resolved in position and shape, including a flat basement near the centre,

two basement edges at the sides, and two different salt structures (sharp in the west and wide in the east). The boundary between basement and salt represents ~0 $\mathrm{g\ cm^{-3}}$, which arises from both positive (basement) and negative (salt) density contrasts occurring in the ensemble of models for this region. The posterior mean model shows both smooth and sharp transitions since the parametrization can adapt complexity which is quantified based on the intrinsic parsimony of Bayes' theorem (MacKay 2003).

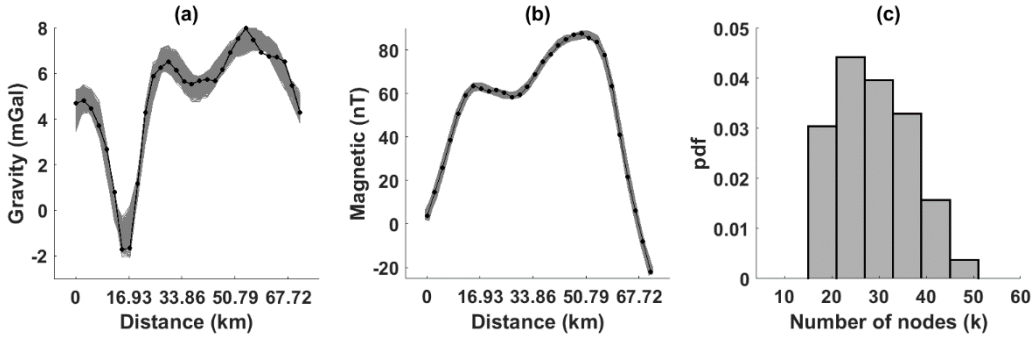

Figure 2.1. (a) Predicted gravity data (gray lines) for each recorded model and synthetic gravity data (dotted black line). (b) The same information for magnetic data. (c) The histogram of the number of nodes that peaked at ~25 nodes.

The 95% CI widths are considered as uncertainty estimates. The 95% CIs are taken to be the most narrow interval containing 95 percent probability at a point in space. Figures 2.2-d and h show 95% CI widths for density contrast and susceptibility, respectively. Higher values occur near boundaries between basement and salt structures since the ensemble of posterior models contains models with salt and models with basement rocks in these areas. When integrating the ensemble to obtain CI widths, large uncertainty occurs.

The maximum likelihood density contrast and susceptibility models for the peak in the *k* distribution are shown in Fig. 2.3. This figure illustrates the natural parsimony of the nested Voronoi parametrization. The parametrization avoids implausible structures that are observed for simple Voronoi partitioning (Fig. 2.3-b). In addition, the nested Voronoi parametrization provides compact structures at reasonable depths and adapts locally to structure complexity, depending on data information. For instance, the transparent sediment exhibits a low number of Voronoi nodes in a large area of sediments. In contrast, nodes concentrate near the sharp rock salt feature.

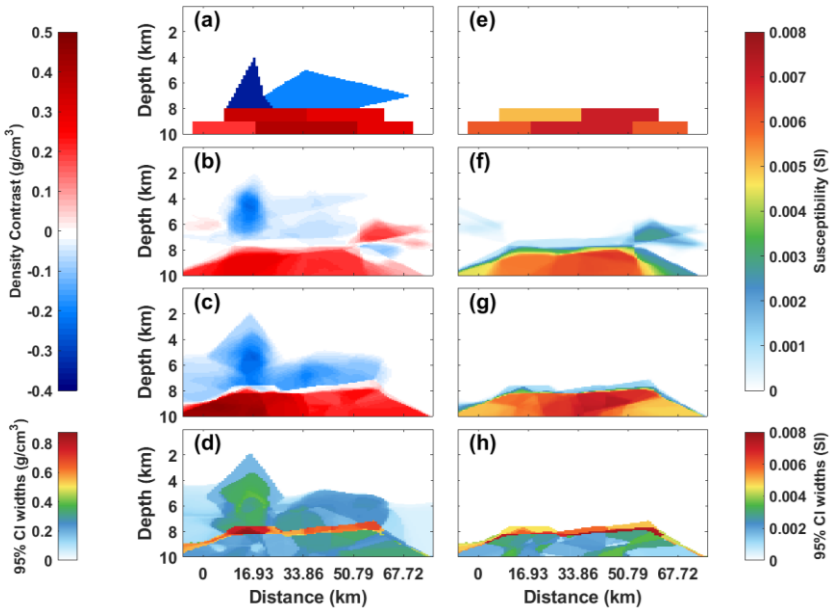

Figure 2.2. (a) True density contrast model for simulation, (b) posterior mean density contrast model for inversion with simple Voronoi partitioning, (c) posterior mean density contrast model for inversion with nested Voronoi partitioning, and (d) 95% CI widths for inversion with nested Voronoi partitioning. (e-h) The same information but for susceptibility.

The maximum likelihood density contrast and susceptibility models for the peak in the *k* distribution are shown in Fig. 2.3. This figure illustrates the natural parsimony of the nested Voronoi parametrization. The parametrization avoids implausible structures that are observed for simple Voronoi partitioning (Fig. 2.3-b). In addition, the nested Voronoi parametrization provides compact structures at reasonable depths and adapts locally to structure complexity, depending on data information. For instance, the transparent sediment exhibits a low number of Voronoi nodes in a large area of sediments. In contrast, nodes concentrate near the sharp rock salt feature.

Estimated noise covariance matrices are presented in Fig. 2.4-a, and e for gravity and magnetic data, respectively. These results represent the true covariance matrices well (Fig. 2.4-b, and f) in both shape and scale. Autocorrelation functions of raw and standardized residuals (Fig. 2.4-c and g) demonstrate that the estimated covariance matrices account for most correlations: Raw residuals exhibit a wide peak, and standardized residuals a sharp peak at zero lag. Histograms of raw and standardized residuals (Fig. 2.4-d and h) show that raw residuals exhibit overfitting (are highly peaked near zero), and standardized residuals are consistent with a standard normal distribution. Therefore, the iterative covariance estimation is considered successful.

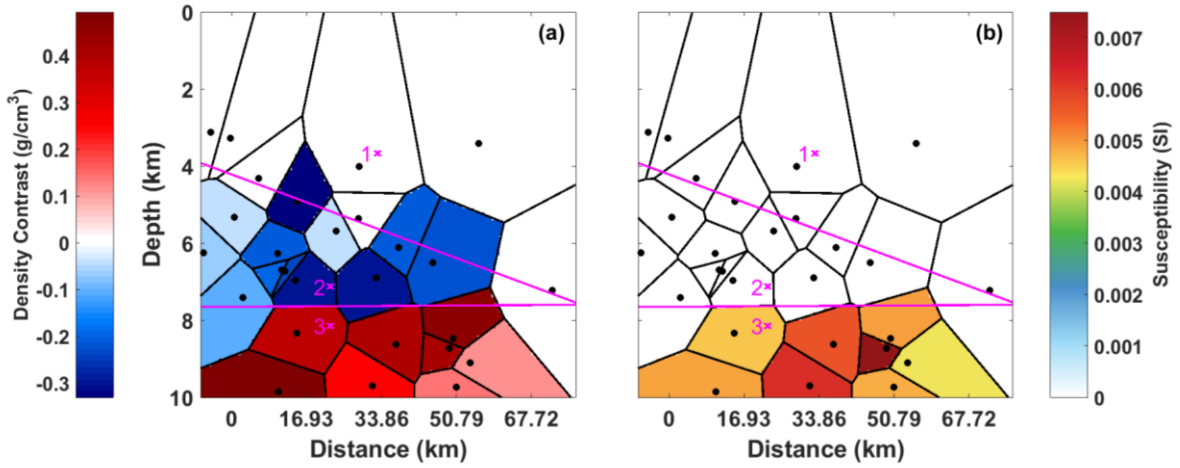

Figure 2.3. The maximum likelihood model, taken at the peak in the *k* distribution, for (a) density contrast and (b) susceptibility (colour scales). Parent nodes (numbered magenta crosses), child nodes (black dots), the parent Voronoi diagram (magenta lines), and the child Voronoi diagram (black lines) are shown.

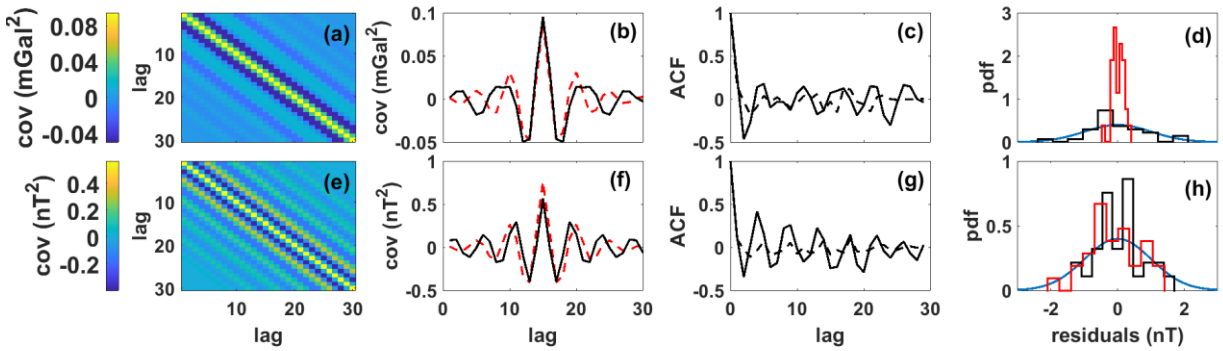

Figure 2.4. (a) Covariance matrix for gravity residuals, and (b) its 15th row (solid black line) with true values shown (dashed red line). (c) Autocorrelation function (ACF) of raw (solid black line) and standardized (dashed black line) gravity residuals. (d) Histograms of raw (red line) and standardized (black line) gravity residuals, and the standard normal distribution (blue line). (e-h) The same information for magnetic residuals.

2.6 Application to Field Data

This section considers application to field data from offshore Abu Dhabi, UAE. Since our algorithm is currently limited to 2-D, we select three 2-D profiles (AA', BB', and CC') from data around the Ghasha oilfield (Fig. 2.5). Profile AA' is chosen to include a likely area of basement uplift, based on interpretation of a peak in DRTP anomalies, and possible salt structures, based on negative gravity anomalies. Profiles BB' and CC' are lines intersecting AA' and selected to validate the results of profile AA'. Each profile includes 30 observations for gravity and magnetic anomalies. The horizontal model axis is extended by 6 km past the first and last datum, respectively, to minimize effects caused by structures beyond the data. The extent of the depth axis is 10 km, based on prior geological information indicating that the basement relief in the area has been inferred as deeper than 8 km (Salem & Ali 2016, Ali *et al.* 2017). The lower bound of the depth prior is 3 km since the salt body is unlikely shallower in this area.

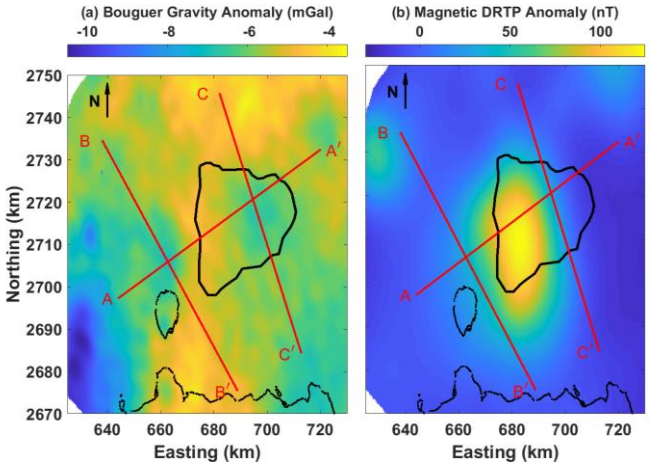

Figure 2.5. (a) Bouguer gravity anomaly and (b) magnetic DRTP data. Red lines show three profiles AA', BB', and CC', chosen for inversion. Coastlines (dotted black) and outlines of the Ghasha oilfield (solid black) are also shown.

We assume that sediments and salt have zero susceptibility, and the basement exhibits positive susceptibilities, giving rise to magnetic anomalies (Salem & Ali 2016, Ali *et al.* 2017). Despite the lack of direct observations of susceptibilities for basement rocks in the UAE, the susceptibility prior is set from 0.004 to 0.008 SI (Al-Garni *et al.* 2010, Shirman *et al.* 2015, Salem & Ali 2016, Ali *et al.* 2017). The sediment density is used as a reference value, resulting in salt with a negative density contrast and basement with a positive density contrast. Based on prior geological information (Geng *et al.* 2020), we set prior

distribution as uniform over 0.1 to 0.5 $\mathrm{g\,cm^{-3}}$ for the basement. The salt prior assumes -0.4 to -0.03 $\mathrm{g\,cm^{-3}}$.

The inversion for profile AA' applies the same procedure described for simulated data. The posterior probability density is approximated by an ensemble of 120,000 samples. The predicted data fit the observed data well (Fig. 2.6-a and b) without signs of over- or underfitting. The number of child nodes (Fig. 2.6-c) peaks at ~ 40. Separate histograms for each rock type are shown in the Appendix F. The posterior mean density contrast model (Fig. 2.7-a) has three main features: A convex basement structure, and two salt structures. The shallowest basement depth is 8 km. The two salt structures include a wide salt structure in the east of the profile (below Ghasha) and a piercing salt structure in the west. The posterior mean shows both sharp and smooth density changes. The wide salt structure has a compact body with denser salt (~-0.3 $\mathrm{g\,cm^{-3}}$) at a depth of ~6 km. Here, the boundary between salt and sediments is resolved at 5- and 6-km depth by smooth transitions from -0.1 $\mathrm{g\,cm^{-3}}$ to 0 $\mathrm{g\,cm^{-3}}$. The smooth transition is likely due to the limited resolution of these data given the small density contrast. The piercing salt structure's density contrast is most negative at 6-km depth (~-0.25 $\mathrm{g\,cm^{-3}}$) and gradually reduces to 0 $\mathrm{g\,cm^{-3}}$ at 4- to 5-km depth, which we interpret as the boundary of salt and sediments. To highlight this interpreted boundary, the isoline of -0.13 $\mathrm{g\,cm^{-3}}$ is marked. This value is taken from the Infracambrian Hormuz salt outcrops in the Jabal Dhanna peninsula and Sir Bin Yas island (Geng *et al.* 2020). Our interpreted boundary exhibits a mushroom shape for the piercing salt and illustrates the general shapes that can be resolved by the trans-D model.

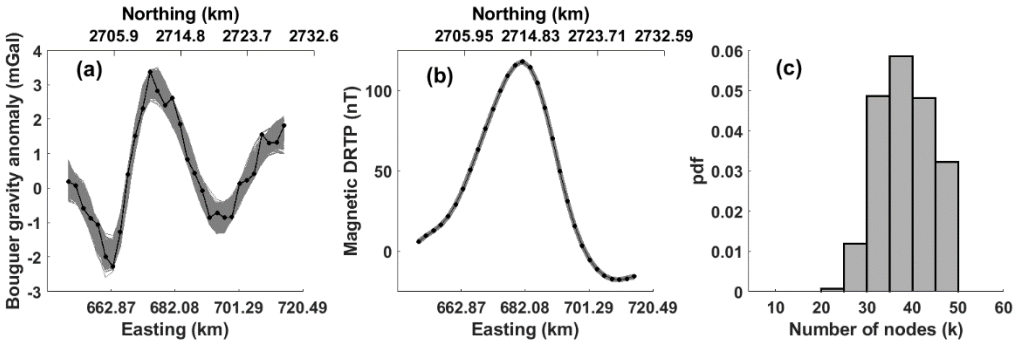

Figure 2.6. (a) Predicted (gray lines) and observed gravity data (dotted black line). Note that predicted data are shown for a large random subsample of all models in the posterior ensemble. (b) The same information for magnetic data. (c) Histogram of the number of child nodes.

The posterior mean susceptibility (Fig. 2.7-c) has values between 0.004 and 0.008 SI. The values are highest near the centre of the convex portion where uncertainties are low (Fig. 2.7-d). Considering that large values are often associated with granitic rocks, we interpret these results as evidence of granitic rocks intruded into more mafic igneous rocks. This implies that larger anomalies in the DRTP map may arise from both uplift and higher susceptibilities of basement rocks. Figures 2.7-b and d show 95% CI widths with higher uncertainty near the boundary between facies. The CI widths are zero at shallower depths since these regions contain no significant structure.

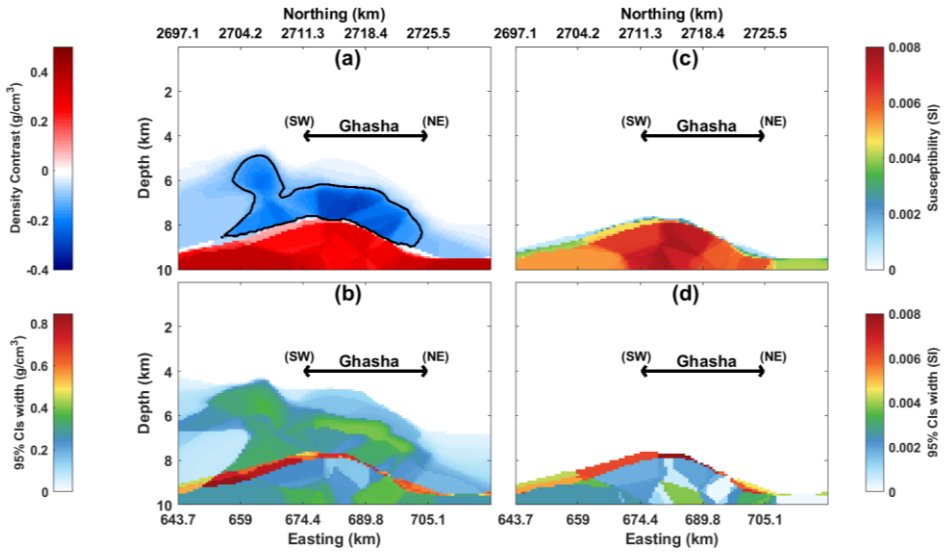

Figure 2.7. Main result: (a) The posterior mean density contrast model, the density contrast of -0.13 $\mathrm{g\,cm^{-3}}$ is shown by a black line. (b) The 95% CI widths for density contrast model. (c-d) The same information for susceptibilities.

Data covariance matrices estimated by the iterative procedure are shown in (Figs. 2.8-a and e). Raw residuals have strong serial correlation (Fig. 2.8-c and g), emphasizing the need for covariance estimation. Correlations in standardized residuals are significantly reduced. Similarly, standardized residuals significantly improve Gaussianity compared to raw residuals and compare favourably to the standard normal distribution (Figs. 2.8-d and h). In conclusion, the covariance estimation improves meeting the assumptions of the likelihood function which raises confidence in the inversion results.

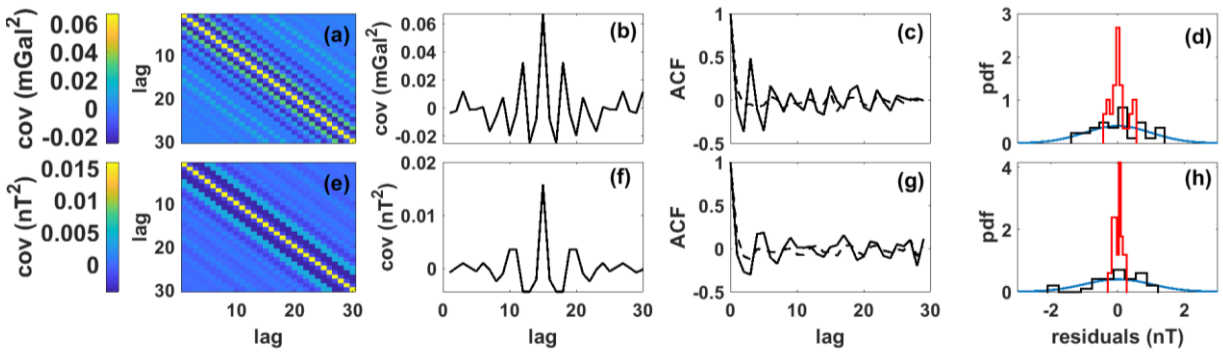

Figure 2.8. (a) Covariance matrix for gravity residuals, and (b) its 15th row. (c) ACF of raw (solid black line) and standardized (dashed black line) gravity residuals. (d) Histograms of raw (red line) and standardized (black line) gravity residuals, and the standard normal distribution (blue line). (e-h) The same information for magnetic residuals.

2.6.1 Comparison to Control Profiles $\boldsymbol{BB'}$ and $\boldsymbol{CC'}$

The same inversion was applied for profiles BB' and CC'. Here, this section considers intersections of salt regions and the basement for the three profiles (Fig. 2.9). Basements in profiles AA' and BB' match generally well. However, the top of the salt in CC' (~ 7,250 m) is deeper than in profile AA' (~ 6,450 m). The top of salt in profile BB' (~ 6,350 m) is considerably deeper than in AA' (~4,750 m). However, an interesting match of density contrasts on profiles AA' and BB' is observed. Intersections for the basement show close agreement for AA' and BB' (~8,750 m). But for CC', basement depth is estimated at ~9,350 m, versus ~8,850 m for AA'. There is agreement between the basement depth in this research and recent works (Ali *et al.* 2017, Geng *et al.* 2020). In addition, good agreement exists between the depth to the top of salt in Ghasha (~ 5,000 m) and a drilled well (Geng *et al.* 2020). Overall, the three profiles indicate acceptable agreement, considering that 2-D inversions are intrinsically limited when data are collected over 3-D structures.

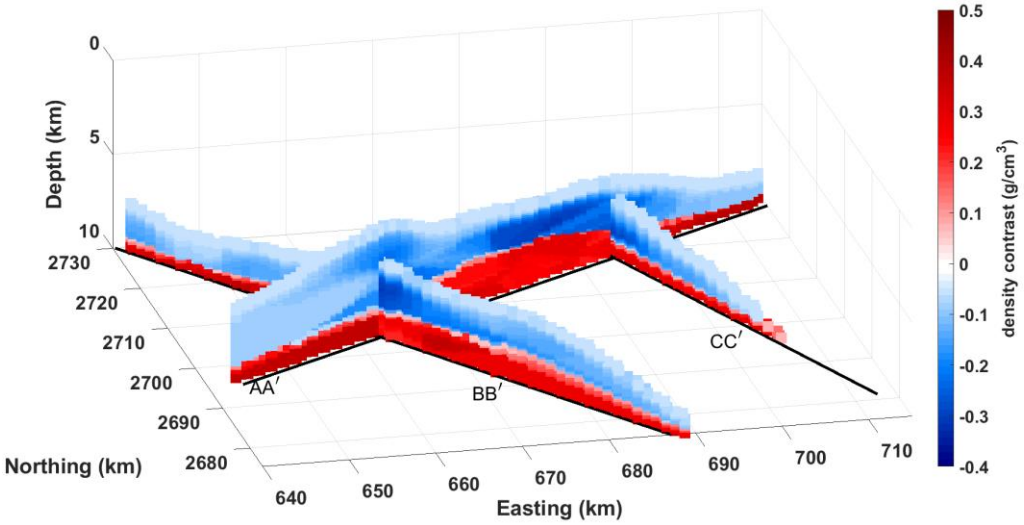

Figure 2.9. 3-D slices of profiles AA', BB' and CC' are represented by black lines. The corresponding 2-D posterior mean models are shown above each profile.

2.7 Discussion and Conclusions

We present a new trans-D joint gravity and magnetic inversion for subsurface structures including sediment, salt, and basement. The method can resolve geologically plausible structures by employing a nested Voronoi parametrization of parent and child nodes, nonoverlapping prior information, and covariance matrix estimation for data-residuals errors. The child nodes are based on a trans-D model that provides adaptable resolution that is not uniform in space but resolves structure in a spatially variable sense, based on data information. The approach requires no regularization, which leads to more objective inversion results and can improve resolution, albeit at a higher computational cost. The introduction of parent nodes permits nonoverlapping priors for density contrasts and susceptibilities of the rock types. Limitations of our method are generally related to the high computational cost, which currently limits us to consider only 2-D forward models. This requires that 3-D Earth structures can be reasonably approximated by 2-D gravity and magnetic profiles. We show that this is a limitation for the complex salt structures we consider.

With simulations, we demonstrated resolution of geologically plausible salt and basement structures in the presence of correlated data noise. Parametrization efficiency was evident since the number of Voronoi child nodes peaked at ~25, meaning that the complex model was described by only ~100 parameters. The

data covariance matrices were assumed as unknown and successfully estimated during the inversion. The choice of prior distribution widths can change solution compactness as demonstrated in the Appendix D. Setting the prior bounds on density contrast and susceptibility objectively can be difficult in the absence of independent geological information and is worthy of future research.

Application to data from offshore Abu Dhabi, UAE, resolved complex salt structures and a convex basement. The salt-dome in the Ghasha oilfield area is broad and a piercing salt structure is resolved in the west of Ghasha. The convex basement was well resolved and interpreted as an intrusion. In particular, we resolved spatial variability in basement susceptibility and density contrast, consistent with plutonic rocks. The three profiles were generally consistent. However, mismatches are found, likely due to approximating 3-D Earth structures with 2-D models. In addition, 2-D profiles are recommended to pass through the anomaly peaks and crossing anomalies perpendicularly (Hinze *et al.* 2013). However, this was not straightforward given the complex data at this site for profiles BB' and CC'. Improving the mismatch between these profiles is an important aspect of future work. In addition, the extension of three parent nodes can be also considered in further problems in which more than three rock types are interested in modeling.

3 Paper II: Trans-D Alpha Shape and AR Models

In this chapter, the paper entitled “Joint Gravity and Magnetic Inversion with Trans-Dimensional Alpha Shape and Noise Models” submitted to a peer-reviewed journal are discussed.

This chapter investigates trans-D irregular spatial partitioning using linear interpolation and alpha shape (LIAS) for 2-D inversion. Furthermore, the noise model is parametrized using trans-D autoregressive (AR) model for 1-D gravity and magnetic data. Here, important elements such as computational cost, data fitting, and efficiency of parametrization of LIAS are discussed and compared with the nested Voronoi partitioning to form a basis for the 3-D problem as an ultimate goal in chapter 4.

3.1 Introduction

Geophysical inverse problems are often ill-posed due to inherent non-uniqueness and model parametrization choices (Sambridge *et al.* 2006b, Aster *et al.* 2016). In general, we distinguish linear, weakly nonlinear, and non-linear inverse problems. Solutions to linear or weakly nonlinear problems can be obtained as closed-form expressions or with modest computational cost via linearization, respectively (Aster *et al.* 2016). Solutions to nonlinear problems require the application of numerical methods (Tarantola 2005). Inverse problems can be considered by deterministic or probabilistic (Bayesian) methods and may be over- and under-parametrized (OP & UP). The OP approach is typically applied to linear and weakly nonlinear problems and requires regularization (Tikhonov & Arsenin 1977). It assumes that a chosen spatial discretization is smaller than the resolution power of the data. Without regularization, this approach causes ill-posedness (Li & Oldenburg 1998b). Regularization over regular grids is a popular choice in inversion of potential field data (Li & Oldenburg 1998b, Pallero *et al.* 2017, Uieda & Barbosa 2017, Maag & Li 2018, Vatankhah *et al.* 2020). Examples of constraints for OP models are depth weighting (Li & Oldenburg 1998b), smoothness, and compactness constraints (Last & Kubik 1983). Drawbacks of such constraints include that the solution is controlled by global trade-off parameters (Sambridge *et al.* 2006b). In addition, uncertainties of parameters reflect the type of regularization choice (Hawkins & Sambridge 2015). Moreover, only one parametrization choice represents the solution while there may be other competing choices.

Bayesian methods consider parameters as random variables and represent the state of knowledge about parameters as probability distributions (Jaynes 2003). These methods can be applied to linear and nonlinear problems, and to OP and UP models. In the OP case, least-square solutions (LSQ) can often be obtained since the problem can be linearized (Reis *et al.* 2005, Fukuda & Johnson 2010). In the UP case, numerical methods, such as Markov chain Monte Carlo (McMC) methods (Gamerman & Lopes 2006) or sequential Monte Carlo samplers (Moral *et al.* 2006) can be applied.

Bayesian models can be generalized with trans-dimensional (trans-D) parametrizations where the number of unknowns is considered unknown (Green 1995). This is a data-driven form of model selection and often applied with non-uniform grids and does not require regularization (Bodin & Sambridge 2009, Dettmer *et al.* 2014). Instead, the approach produces intrinsically parsimonious parametrizations (Sambridge *et al.* 2006b) that are locally adaptive (Hawkins & Sambridge 2015). Nonetheless, limitations exist for trans-D models. For example, the dependence on the choice of discretization (e.g., Voronoi cells, wavelets) can cause artifacts and dampen some of model features. Sampling of trans-D models was introduced to geophysical inversion for seismic applications (Malinverno 2002), but has not been extensively considered for potential field data. Potential field examples include parametrizations of the geometry of a 2-D body by trans-D polygons (Luo 2010), assuming known density inside the polygon, inferring the interior mass distribution of a planet with a trans-D point-mass distribution (Izquierdo *et al.* 2020), and a hierarchical Voronoi model for salt-tectonic structures (Ghalenoei *et al.* 2021a).

The treatment of data noise can have a significant impact on parameter spatial resolution and uncertainty in inverse problems. Assuming known noise parameters is common in geophysical inference, but there are significant advantages to hierarchical noise estimation (Malinverno & Briggs 2004). In particular, hierarchical estimation can quantify the effect of limited knowledge about the noise parameters on geophysical parameters of interest. In model selection, the choice of noise parametrization can affect model complexity. While the estimation of the noise variance is often straightforward, estimation of covariances is less straightforward. For covariance estimation, nonparametric or parametric approaches exist.

Nonparametric approaches estimate covariances from data residuals (Dettmer *et al.* 2007, 2014), and can account for complex covariance matrices. However, nonparametric approaches depend on empirical damping and scaling. Parametric approaches include exponentially or normally decaying functions (Bodin *et al.* 2012, Dettmer *et al.* 2012), and sinc functions (Kolb & Lekić 2014, Mustać & Tkalčić 2016). However, some of these approaches are associated with higher computational cost for inverting the covariance

matrix during the computation of the likelihood function. Parametric models can be conveniently implemented with low computational cost by employing an autoregressive (AR) model (Dettmer *et al.* 2012, Steininger *et al.* 2013).

We propose a new parametrization that combines trans-D spatial and trans-D noise models which leads to more complete uncertainty quantification. The spatial partitioning is based on linear interpolation and alpha shapes (LIAS), and demonstrate advantages over Voronoi-based approaches (Ghalenoei *et al.* 2021a) for salt tectonic structures. The noise model is based on a trans-D AR model that provides objective model selection for covariance estimation. This generalized noise model has the potential for application with various geophysical data types, including spatial and time-series data. The parametrization is applied to simulated and field data. With simulations, we demonstrate the advantages of combining trans-D AR noise models with spatial trans-D models. Application to aerogravity and aeromagnetic field data from Abu Dhabi, United Arab Emirates (UAE), shows successful decorrelation of data residuals and resolution of basement and salt diapir structures with more detailed resolution and improved data fit.

3.2 Theory and Method

3.2.1 Trans-D Noise Parametrization

Since assumptions about data-error statistics are made to formulate the likelihood function $\mathcal{L}(\boldsymbol{m}_k, k)$, noise variances and covariances have significant impact on inferences. We propose a parametric noise model to estimate variance and covariances of residual errors in geophysical data based in an autoregressive (AR) process. Supported by the central limit theorem, we assume a Gaussian noise distribution resulting in the logarithm of the likelihood function

$$\log\mathcal{L}(\boldsymbol{m}_k, k) = -\frac{N}{2}\log_e(2\pi) - \frac{1}{2}\log_e(|\boldsymbol{C}_d|) - \frac{1}{2}\boldsymbol{r}^T\boldsymbol{C}_d^{-1}\boldsymbol{r}, \tag{3.1}$$

where N is the number of data, $\boldsymbol{r} = \boldsymbol{d}^{\text{obs}} - \boldsymbol{d}(\boldsymbol{m}_k)$ are the data residuals, $\boldsymbol{C}_d$ is the data covariance matrix, and $|\,|$ denotes the determinant of a matrix. Note that $\boldsymbol{C}_d$ can be represented by the dot product of multiple data noise covariance matrices that may be available from different sources. However, the total data covariance matrix is assumed in this work. Even though many geophysical applications assume uncorrelated residuals, significant correlations often exist, particularly for potential field data with signal wavelengths that are larger than the spatial sampling applied in the field. This is particularly the case for

airborne acquisition which we consider as a field example. A computationally efficient approach to address correlated errors is to apply an AR noise model in the likelihood function (Dettmer *et al.* 2012)

$$\log\mathcal{L}(\boldsymbol{m}_k, k) \propto -N\log_e(\sigma) - \frac{1}{2}\left(\frac{\boldsymbol{d}^{\text{obs}} - \boldsymbol{d}(\boldsymbol{m}_k) - \boldsymbol{\lambda}(\boldsymbol{m}^{\text{AR}})}{\sigma}\right)^T \left(\frac{\boldsymbol{d}^{\text{obs}} - \boldsymbol{d}(\boldsymbol{m}_k) - \boldsymbol{\lambda}(\boldsymbol{m}^{\text{AR}})}{\sigma}\right), \quad (3.2)$$

where σ is an unknown standard deviation, that can be implicitly obtained by $\sigma = \sqrt{\frac{||\boldsymbol{r}||^2}{N}}$, where $||\ ||$ is the *L2* norm. The terms $\frac{\boldsymbol{d}^{\text{obs}} - \boldsymbol{d}(\boldsymbol{m}_k) - \boldsymbol{\lambda}(\boldsymbol{m}^{\text{AR}})}{\sigma}$ are assumed to be uncorrelated, standardized residuals. The term $\boldsymbol{\lambda}(\boldsymbol{m}^{\text{AR}})$ represents a prediction of data residuals by an AR process. Previous work (Dettmer *et al.* 2012) applied an AR process of fixed order 1 (AR(1)) or 2 (AR(2)), which results in a noise model with unknown parameters σ and one or two unknown AR parameters. Note that AR(1) models are equivalent to a data covariance matrix with exponential covariance decay (Dettmer *et al.* 2012). Such simple decay is not commonly observed in geophysical problems (Dettmer *et al.* 2007), but often assumed for simplicity.

Here, we introduce an AR model with trans-D order between 0 and 3. This data-driven model can produce covariance matrices that are typical for geophysical data and accounts for the uncertainty in specifying the order of the process in inferences. Let vector $\boldsymbol{\lambda}(\boldsymbol{m}_p^{\text{AR}})$ represents serially correlated residuals (e.g., for a time series or a spatial transect) predicted from an AR model of order p, where $\boldsymbol{m}_p^{\text{AR}} = [\varphi_1, \varphi_2, \dots, \varphi_p]$, and $\boldsymbol{\lambda}(\boldsymbol{m}_p^{\text{AR}})$ can be written as (Shumway & Stoffer 2000)

$$\lambda_t(\boldsymbol{m}_p^{\text{AR}}) = c + \sum_{i=1}^{p} \varphi_i r_{t-i} + \varepsilon_t\,, \qquad t = 1, \dots, N, \quad (3.3)$$

where c is a constant (zero for unbiased residuals), and ε_t is uncorrelated Gaussian noise. For geophysical applications, it is reasonable to consider stationary conditions for the AR model. Details of stationarity are in the Appendix H. The stationary condition can be achieved by prior constraints on the AR model parameters. The general structure of an AR model is that higher orders require lower orders to be present (e.g., an AR(2) model can be created by adding an additional parameter to an existing AR(1) model). Therefore, we only add/delete AR coefficients at the end of the current AR model vector.

The MHG algorithm is applied to the trans-D AR model, with three moves, each applied with probability of 1/3:

(i) Add an AR coefficient to the end of the AR model vector, $\boldsymbol{m}_p^{\text{AR}} \rightarrow \boldsymbol{m}'^{\text{AR}}_{p+1}$.

(ii) Delete an AR coefficient from the end of the AR model vector, $\boldsymbol{m}_p^{\mathrm{AR}} \rightarrow \boldsymbol{m}'^{\mathrm{AR}}_{p-1}$.

(ii) Perturb an AR coefficient, chosen uniformly random, by a Cauchy proposal distribution, $\boldsymbol{m}_p^{\mathrm{AR}} \rightarrow \boldsymbol{m}'^{\mathrm{AR}}_{p}$.

Uncorrelated residuals can be represented by an AR(0) model (no coefficients), $\boldsymbol{m}_0^{\mathrm{AR}}$. The only proposal for this case is to add a coefficient, sampled from the prior distribution. In contrast, for $\boldsymbol{m}_1^{\mathrm{AR}}$ all three moves are possible. Therefore, the acceptance probabilities are

$$\alpha\left(\boldsymbol{m}'^{\mathrm{AR}}_1 \middle| \boldsymbol{m}_0^{\mathrm{AR}}\right) = \min\left[1, \frac{1}{3}\frac{\mathcal{L}(\boldsymbol{m}'^{\mathrm{AR}}_1)}{\mathcal{L}(\boldsymbol{m}_0^{\mathrm{AR}})}\right], \tag{3.4}$$

$$\alpha\left(\boldsymbol{m}'^{AR}_0 \middle| \boldsymbol{m}_1^{AR}\right) = \min\left[1, 3\frac{\mathcal{L}(\boldsymbol{m}'^{AR}_0)}{\mathcal{L}(\boldsymbol{m}_1^{AR})}\right], \tag{3.5}$$

$$\alpha\left(\boldsymbol{m}'^{AR}_{p'} \middle| \boldsymbol{m}_p^{AR}\right) = \min\left[1, \frac{\mathcal{L}(\boldsymbol{m}'^{AR}_{p'})}{\mathcal{L}(\boldsymbol{m}_p^{AR})}\right], \text{for all } p, p' \in [1, \dots, p^{\max}]. \tag{3.6}$$

For $p = p^{\max}$, the probabilities of *add*, *delete*, and *perturb* are 0, 1/3, and 2/3, respectively.

3.2.2 Spatial Partitioning

In conventional trans-D Voronoi partitioning, a regular grid is partitioned by k Voronoi nodes which define k Voronoi cells. The MHG algorithm is applied to consider a range of k values and permits transitioning between models for various choices of k. This approach applies little prior knowledge in the parametrization. However, geological constraints may exist. For example, in geophysical applications that aim to infer the spatial extent of rock types, geological constrains on depths and locations of rock types often exist. If such information is ignored, conventional Voronoi partitioning may poorly image rock types and adding an additional hierarchy of Voronoi partitioning (NV3) can improve images (Ghalenoei *et al.* 2021a). The NV3 partitioning was previously applied to joint gravity and magnetic inversion to partition the model space into three rock types (Ghalenoei *et al.* 2021a). The base model consists of k Voronoi child nodes and hierarchical partitioning of these is by three parent nodes.

Here, we propose the new LIAS parametrization which is not based on Voronoi cells and compare it to NV3. The LIAS parametrization combines linear interpolation with alpha shapes (Edelsbrunner *et al.* 1983) in a trans-D model. The linear interpolation uses a Delaunay triangulation (Delaunay 1934) of k nodes and interpolates values onto a regular grid. The alpha shape algorithm (Edelsbrunner *et al.* 1983) uses the

same Delaunay triangulation to generate a convex or concave hull that envelops the nodes. The shape of the hull depends on the alpha shape parameter (α) and the locations of nodes. As α approaches zero, the shape approaches the node set. As α increases, the shape approaches the convex hull of that set of nodes. Importantly, alpha shapes are not necessarily convex hulls, which is advantageous for structural models where convex and concave shapes may be plausible. The model parameters for LIAS are sampled with the MHG algorithm.

The nodes are assigned density contrast parameters ($\Delta\rho$). For the basement, susceptibility (χ) values are calculated from the density contrasts (Li & Oldenburg 1998b). Salt and sediment are assumed to have negligible susceptibility. Therefore, density contrast and susceptibility share the same structural boundary for the basement.

3.3 Application to Simulated Data

3.3.1 True Model and Assumptions

The true model includes three rock types in four structures: Two salt diapir structures located on top of a basement with two layers, and sediment in the remainder of the space (Fig. 3.1-a). The depths to the top of the two salt diapirs are 5 and 7 km, respectively, and the top of the basement is at 8-km depth. The regular discretization for the forward modeling uses 100 by 100 cells with a size of 800 by 100 m in the x and z directions, respectively. The prior distributions for density contrast for salt and basement are $(-0.4, -0.2)$ g cm^{-3} and $(0.2\ , 0.4)$ g cm^{-3}, respectively. The density of the sediment is assumed to be the reference value with 2.6 g cm^{-3} and the density contrast is assumed to be zero. We compute susceptibility for the basement based its density contrast by assuming a constant ratio of $\frac{\Delta\rho}{\chi} = 50$ (Geng *et al.* 2020, Kabirzadeh *et al.* 2021). The prior for the number of nodes is uniform between 6 and 50.

Gravity data are contaminated with correlated Gaussian noise with a standard deviation of 8% of the maximum of the true gravity data. The noise correlation is based on an AR(2) process with coefficients $\varphi_1 = 0.6$ and $\varphi_2 = -0.4$. To test the ability of the algorithm to also quantify uncorrelated residuals, we assume that the noise on magnetic data is uncorrelated Gaussian distributed with a standard deviation of 4% of the maximum of the true magnetic data. The prior pdfs for AR coefficients are assumed to be bounded, uniform, and meet the stationary condition (Appendix H). Prior bounds are $(-0.85, 0.9)$ for AR(1), $(-0.85, 0.1)$ for AR(2), and $(-0.25, 0.25)$ for AR(3). The prior for the AR order is uniform between 0 and 3. Empirically, the AR model converges faster than spatial parameters. Therefore, we apply MHG moves to the AR model during 20% of the steps, and MHG moves to spatial parameters during 80% of the

steps. In addition, we promote stability by assuming an AR(0) model during the first 30,000 steps (part of burn-in). This assumption avoids that the noise model fits major data features which can result in poor burn-in.

The starting model is randomly sampled from the prior. The MHG sampler is applied using parallel tempering (PT) (Geyer 1991, Sambridge 2014) with $N_{PT} = 20$ parallel chains including 10 chains at $T = 1$, and a temperature spacing of $\Delta T = 1.2$ for the remaining chains. The PT relaxes the likelihood function at higher temperatures which improves sampling efficiency for trans-D models (Dettmer & Dosso 2012). For interpretation, we consider posterior mean (PM) models after discarding the initial 2 million samples.

The inversion is carried out for the two hierarchical partitioning choices LIAS and NV3. Note that LIAS can be applied under the assumption that nodes only describe rock salt diapir and basement via the trans-D model. Outside the alpha shape, the rock is assumed to be sedimentary, resulting in an efficient parametrization. A horizontal line is applied to separate rock salt from basement rocks, adding an additional unknown to the parametrization. Prior for the horizontal line is the same as prior for z parameters. A uniform prior between 1 and 6 is assumed for the alpha shape parameter (α). In addition, the application of the NV3 choice is straightforward since each parent node is assigned one rock type.

3.3.2 Results

3.3.2.1 Spatial Model

We recorded one million posterior samples for each of the two partitioning choices. The convergence was considered by visual inspection of the sampling history of log-likelihood and k values (Dettmer *et al.* 2014). Figure 3.1 shows PM results for density contrast and susceptibility as well as uncertainties in terms of 95% credibility intervals (CIs) widths. For LIAS, both rock-salt structures and basement are imaged well (Fig. 3.1-b) and the solution exhibits significant uncertainty. The NV3 also images basement and salt well and results exhibit unrealistically low uncertainty. For example, the low uncertainty is problematic when considering that the sediment between the two rock salt structures is not imaged (Fig. 3.1-c). In addition, susceptibility values in LIAS are closer to the true model than NV3 (Fig. 3.1-d, e, and f).

The uncertainty values estimated for LIAS appear to be more realistic and help to avoid overinterpretation (Fig. 3.1-g). The highest uncertainties near boundaries between basement and salt are caused by positive and negative density contrast occurring at the same location in the ensemble of models. In general, structural boundaries exhibit higher uncertainties. The LIAS partitioning shows a higher flexibility by generating hulls, and uncertainty exists throughout the model space.

The maximum likelihood (ML) models for each choice are taken for the peak of the k distribution (Fig. 3.1-h-j). Note the locally adaptive nature with increased node density near salts structures and fewer nodes capturing the transparent sediments.

Figure 3.2 shows the posterior predictive distribution, i.e., the range of predicted data produced by the posterior ensemble, in terms of 95% CIs widths. Noisy simulated data are also shown. The LIAS parametrization fits gravity and magnetic data well (Fig. 3.2-a, b). For NV3 (Fig. 3.2-d, e) magnetic data are fit to a similar level as for LIAS. However, gravity-data fit is much poorer. Predictions do not fit significant data features which is often a sign of under-parametrization. This observation is consistent with the small uncertainties, which are a common for under-parametrized models. Marginal probability distributions for the number of nodes are shown in Fig. 3.2-c and f, with peaks at 22 and 12 nodes for LIAS and NV3, respectively. Although both parametrizations produced reasonable images of the true structure (Fig. 3.2), LIAS appears as superior with more realistic uncertainties and better data for gravity data.

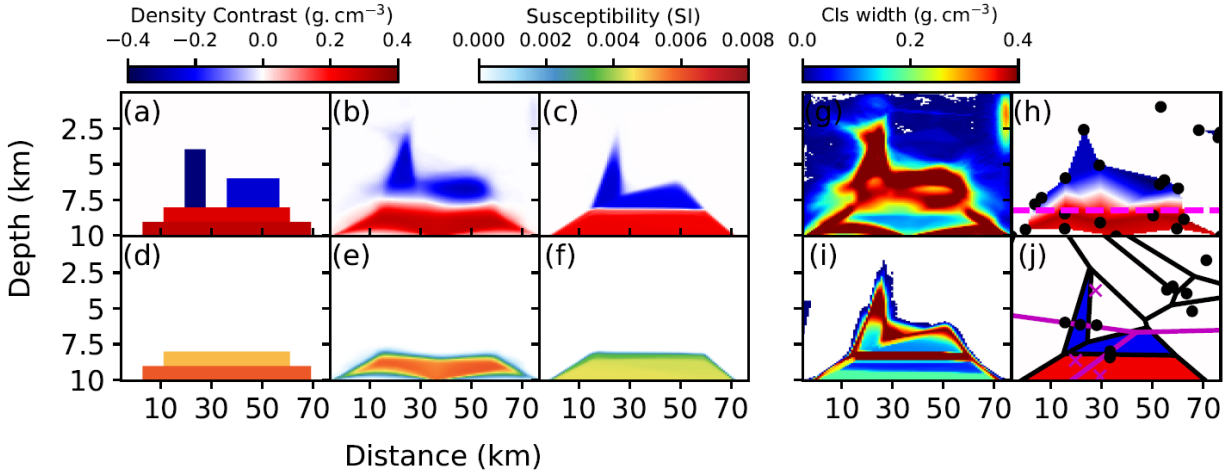

Figure 3.1. (a) True density contrast model. The PM model for density contrast using (b) LIAS, and (c) NV3. (d-f) susceptibility models, same as (a-c). The 95% CIs widths for density contrast using (g) LIAS, and (i) NV3. The ML models for (h) LIAS with nodes (black dots) and the line (dashed magenta line), and (j) NV3 with parent Voronoi diagram (magenta lines and crosses) and child Voronoi diagram (black lines and dots).

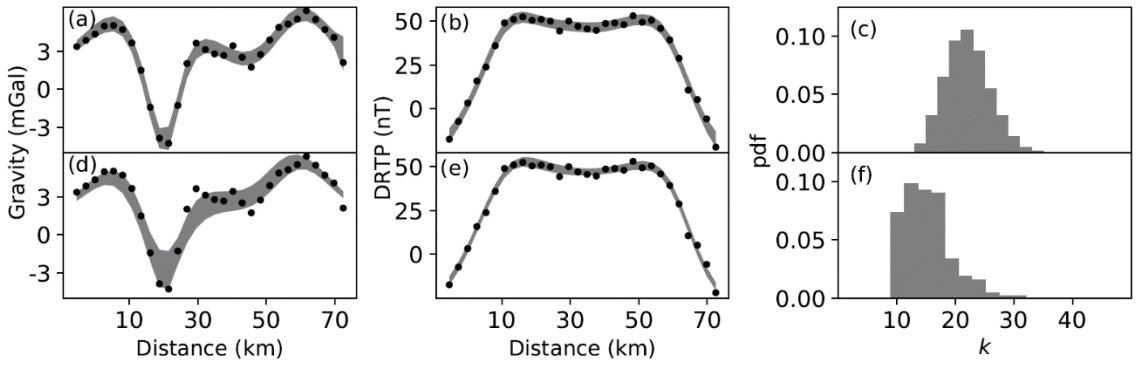

Figure 3.2. Fitted (a) gravity and (b) magnetic data, and (c) the marginal probability distribution of k are represented for LIAS. Simulated data are shown with black dots and 95% CIs widths of fitted data are shown by a grey color. Same information but for NV3 in (d)-(f).

3.3.2.2 Noise Model

Results for the noise model are only presented for the superior LIAS partitioning. Figure 3.3 summarizes posterior results for the noise model in terms of marginal densities for AR parameters and representative rows of the equivalent covariance matrix for illustration purposes. Marginal distributions for gravity AR orders (Fig. 3.3-a) shows AR(2) as the most probable order, which is consistent with the true model. Marginals for the AR coefficients (Fig. 3.3-b-e) are also consistent with the true model. In particular the marginals for the two AR(2) coefficients are consistent with true models.

An AR model can be converted to a covariance matrix (Lee & Sung 2014) and Fig. 3.3-f-i show some covariance matrices for corresponding AR models. Interestingly, AR(3) is nearly as well supported as AR(2) in Fig. 3.3-a, which makes sense when considering that the resulting covariance structures (Fig. 3.3-h and i) are highly similar. Figure 3.3-h and i also show that a higher-order AR models produce more complex covariance matrices.

For magnetic residuals (Fig. 3.3-j-r), AR(0) is the most probable, matching the true model. However, significant probability exists for AR(1), AR(2), and AR(3). This suggests that data information to resolve noise parameters in detail is limited.

The ability of the trans-D AR model to quantify noise characteristics can be tested by residual analysis (Dettmer *et al.* 2007). Raw residuals are defined as those obtained without applying AR models, and standardized residuals account for correlations and are expected to be distributed as uncorrelated Gaussian with unit standard deviation. Figure 3.4-a shows the autocorrelation of raw gravity residuals

with considerable correlations at lags near zero. However, the autocorrelation of standardized residuals indicates no significant correlations. Results for magnetic data (Fig. 3.4-b) shows that both raw and standardized residuals largely uncorrelated. Histograms of standardized residuals for both data types agree well with the standard normal distribution, $N(0,1)$, in Fig. 3.4-c.

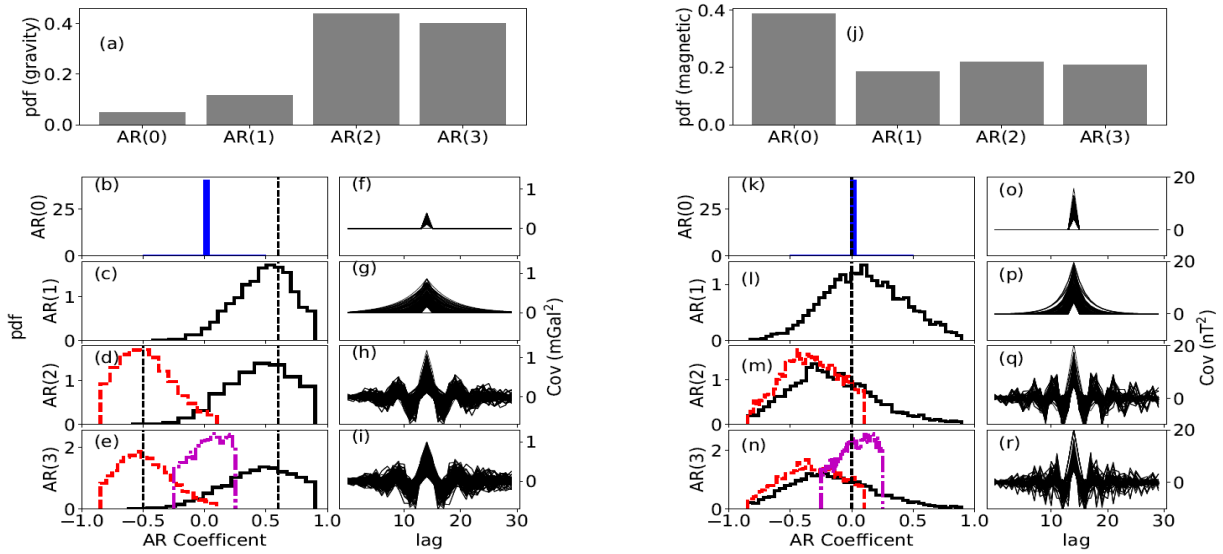

Figure 3.3. (a) The marginal probability distribution of AR model orders during the sampling is shown for gravity. The marginal probability distributions of AR coefficients at orders 0, 1, 2, and 3 are shown for gravity in (b), (c), (d), and (e), respectively. The blue, black, red, and magenta distributions represent the zeroth, first, the second, and the third coefficient, respectively. The dashed black lines show true AR coefficients, which are [0.6, -0.5], used in the simulation. Selected random covariance matrices for AR models at orders 0, 1, 2, and 3 are shown for gravity in (f), (g), (h), and (i), respectively. Note that only the middle lag of the covariance matrix is shown here. The same information but for magnetic AR models are represented in (j)-(r).

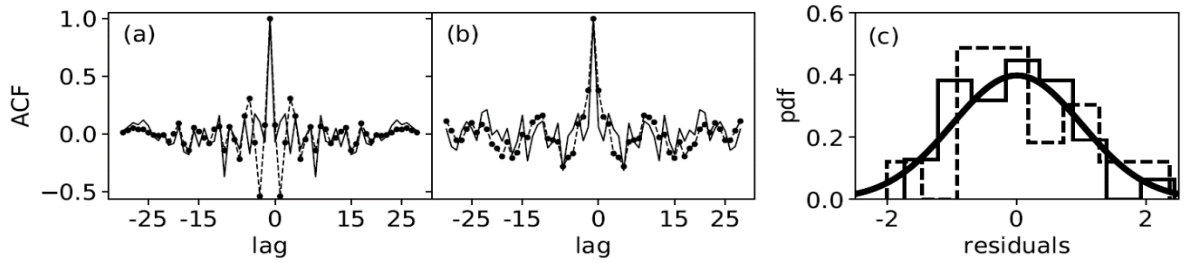

Figure 3.4. Autocorrelation of standardized residuals (solid black) and raw residuals (dot-dashed black) for (a) gravity and (b) magnetic residuals. (c) Histograms of standardized gravity and magnetic residuals are shown by a solid and dashed black line, respectively. The standard normal distribution is indicated by a solid black line.

3.4 Application to Potential Field Data

Here, LIAS and NV3 inversions are applied to aerogravity and aeromagnetic field data acquired by Sander Geophysics Ltd (SGL) in offshore Abu Dhabi, UAE. The survey area includes multiple complex salt diapirs and also exhibits basement topography which make it an ideal site to study our methods. We perform the joint inversion over the Ghasha oilfield and consider results in terms of resolution of basement and salts, and in terms of residual analysis.

The gravity and magnetic survey by SGL was carried out for ADNOC in 2007-2008. The data include 13,804 line km at 250 m above sea level with line spacing of 2-km and 10-km between tie lines (Ali *et al.* 2017). Data corrections were Eötvös, latitude, free air, Bouguer, the curvature of the Earth, terrain, static, and levelling corrections. The terrain correction assumes a density of 2.6 $\mathrm{g\,cm^{-3}}$ for land and terrain-topographic data from the Shuttle Radar Topography Mission (SRTM). In the seawater-depth correction process, a density of 1.02 $\mathrm{g\,cm^{-3}}$ was applied over marine areas utilizing bathymetric data obtained from the Gridded Bathymetric Chart of the Oceans 1-minute grid. Regional effects were calculated and subtracted by using a low-pass filter with a 3-km half-wavelength and upward continued to 20 km above sea level. Eventually, data were gridded at 1 km by 1 km.

The aeromagnetic survey used Caesium optically pumped magnetometers with a 0.001 nT (1 Tesla = $\mathrm{kg{\cdot}s^{-2}{\cdot}A^{-1}}$) sensitivity and sensor noise of 0.02 nT. Data processing included removal of the International Geomagnetic Reference Field (IGRF), leveling error corrections, and diurnal fluctuation corrections. Finally, differentially reduced-to-the-pole (DRTP) data were obtained (Salem & Ali 2016). These post-processed data (Fig. 3.5) show gravity and magnetic anomalies associated with the sediment, salt, and basement structures.

We consider a SW-NE profile (AA') across the Ghasha oil field with a negative Bouguer anomaly and a positive DRTP anomaly (Fig. 3.5). Profile AA' contains 30 data points each for gravity and magnetic data. The horizontal extent of the model space is based on profile AA' with 5 km of padding on each end to minimize the effects from structures beyond the data coverage. The vertical axis of the model space is

from 0- to 10-km depth. The settings for the field data inversion are identical to those for simulated data except that the prior distribution for rock salt that is uniformly over $(-0.4, -0.05)$ g cm^{-3} and the prior for k is uniform over $(6, 100)$.

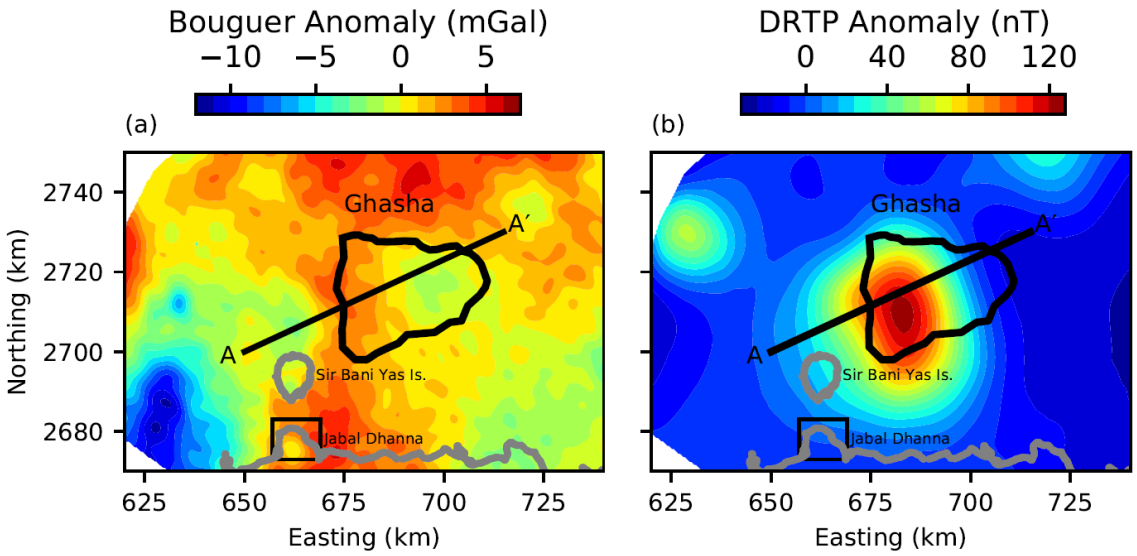

Figure 3.5. (a) Bouguer gravity anomaly and (b) DRTP-TMI magnetic anomalies. The black straight line indicates the profiles AA'. Coastlines (grey) and outlines of the Ghasha oilfield (solid black) are also represented.

The predicted data for both LIAS and NV3 fit the observed data well (Fig. 3.6) without indication of over- or underfitting. However, the marginal distributions for k show a peak of $\sim$20 nodes for LIAS and $\sim$40 nodes for NV3 (Fig. 3.6). Therefore, LIAS is the more parsimonious parametrization of the two.

The PM models (Fig. 3.7) for both parametrizations show significant basement topography. However, the basement for LIAS is located at shallower depth. In both cases, two salt structures are visible at eastings of $\sim$ 665 and 690 km, respectively. The smaller eastern structure appears as more piercing. In the case of LIAS, the smaller feature has a distinct, localized finger reaching to much more shallow depth. For additional interpretation, we indicated three contour lines at levels of -0.2, -0.13, and -0.01 g cm^{-3}. The level of -0.13 g cm^{-3} is that of the Infracambrian Hormuz salt outcrops in the Jabal Dhanna peninsula and Sir Bin Yas island (Geng *et al.* 2020). The level of -0.01 g cm^{-3} is interpreted as the edge of sedimentary rocks. The 95% CI widths (Fig. 3.7) indicate good resolution of the basement topography: The region of higher uncertainty due to integrating both positive and negative density contrasts in the same area is narrow.

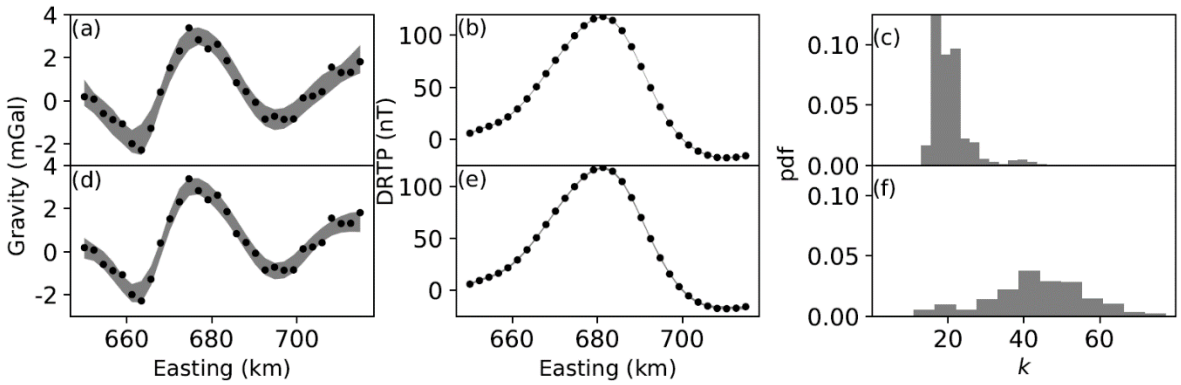

Figure 3.6. Data fit for (a) gravity and (b) magnetic data, and (c) marginal distribution of k for the LIAS parametrization. Observed data (black dots) and 95% CIs widths for predicted data (grey) are shown. (d - f) Same information for NV3.

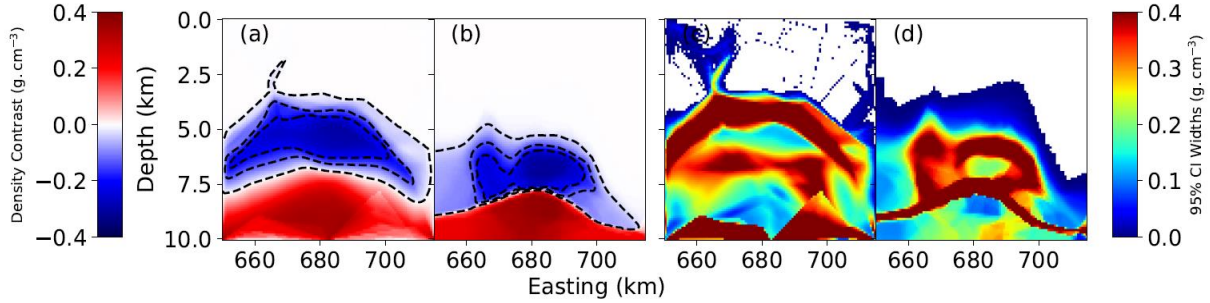

Figure 3.7. PM model for the density contrast using (a) LIAS, and (b) NV3 partitioning. The 95% CIs widths for density contrast using (c) LIAS, (d) NV3.

The trans-D AR model was applied for both parameterizations, but results are shown only for LIAS (Fig. 3.8). The most probable AR order is 3 for gravity and 2 for magnetic data. This implies that data are strongly correlated which is consistent with expectations for airborne data collection with high spatial sampling. Raw and standardized residuals (Fig. 3.9) show that strong correlations exist in raw residuals and that these are significantly diminished by the trans-D AR models. In addition, the standardized residuals significantly improve Gaussianity (Fig. 3.9).

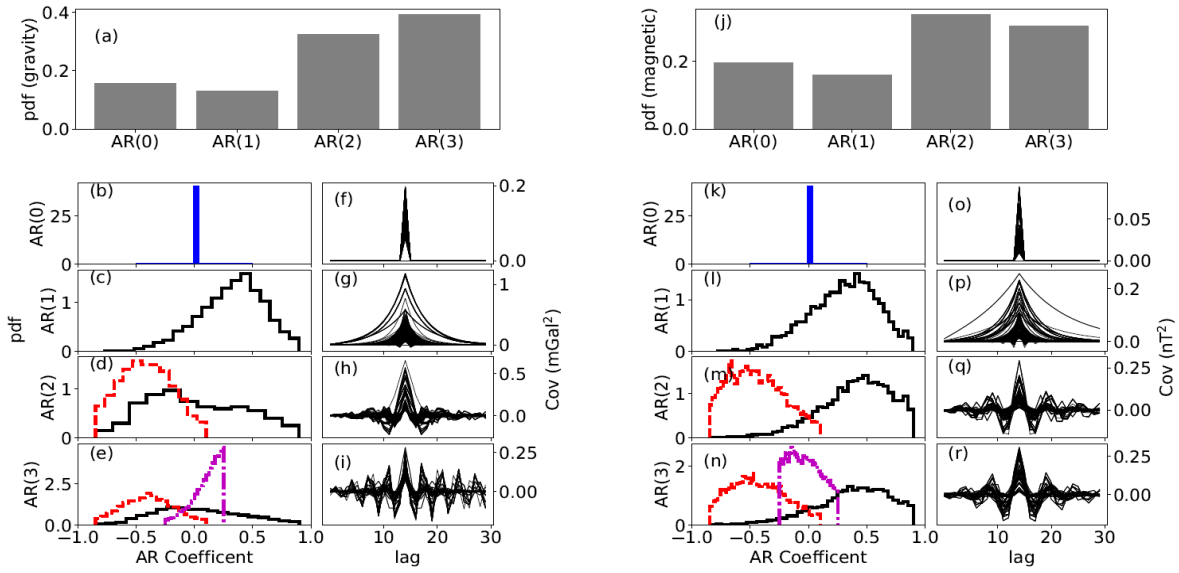

Figure 3.8. (a) The marginal probability distributions of AR model orders during the sampling are shown for gravity. The marginal probability distributions of AR coefficients at orders 0, 1, 2, and 3 are shown for gravity in (b), (c), (d), and (e), respectively. The blue, black, red, and magenta distributions represent the zeroth, first, the second, and the third coefficient, respectively. Selected random covariance matrices for AR models at orders 0, 1, 2, and 3 are shown for gravity in (f), (g), (h), and (i), respectively. Note that only the middle lag of the covariance matrix is shown here. The same information but for magnetic AR models are represented in (j)-(r).

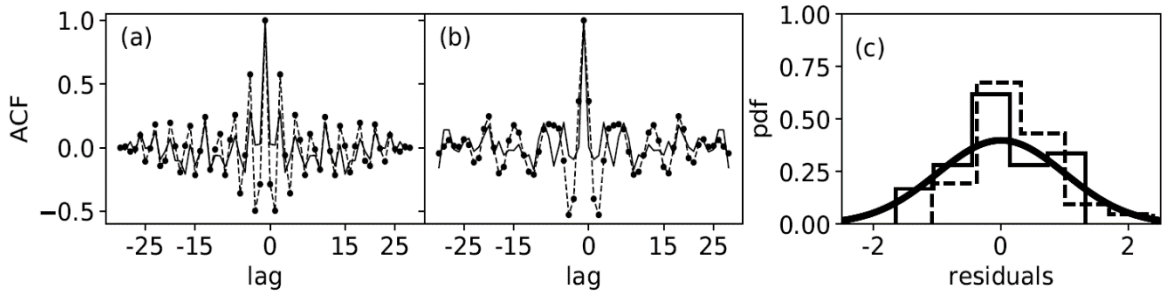

Figure 3.9. (a) Autocorrelation of standardized residuals (solid black) and raw residuals (dot-dashed black) for (a) gravity and (b) magnetic residuals. (c) Histograms of standardized gravity and magnetic residuals are shown by a solid and dashed black line, respectively. The standard normal distribution is indicated by a solid black line.

3.5 Conclusions

Objective partitioning for salt structures in gravity and magnetic data inversion is difficult because meaningful prior constraints for rock salt diapir and basement are required to reduce non-uniqueness. We studied two choices of spatial partitioning (LIAS and NV3), which permit meaningful prior constraints on rock type (sedimentary rocks, rock salt, and basement rocks) leading to better resolution of salt structures. In particular, the newly proposed LIAS parametrization captures complex shapes with few parameters and produces excellent data fits. In particular, LIAS locally adapts the model without the need for global or local smoothing/damping constraints. In addition, LIAS does not require any nodes for the background sediment, thus reducing the number of required nodes.

Further, we presented a trans-D AR model to decorrelate data residuals for gravity and magnetic data. A posteriori residual analysis demonstrated a significant reduction in the correlation of standardized residuals and residuals that are distributed more similar to a standard normal distribution. Importantly, the trans-D AR approach does not require empirical damping and scaling which are common for empirical covariance estimation. In addition, this hierarchical noise estimation can account for the limited knowledge about the data covariance matrix in uncertainty estimates for Earth structure. Finally, the AR-based noise model is computationally more efficient than other hierarchical approaches that require the inversion of covariance matrices for the evaluation of the likelihood function.

In conclusion, the trans-D LIAS-AR method has significant advantages over other Voronoi-based approaches and provides objective, data-driven uncertainty quantification for 2-D potential-field data.

4 Paper III: Trans-D Potential Inversion for 3-D Earth Models

In this chapter, the paper entitled “Trans-Dimensional Gravity and Magnetic Joint Inversion for 3-D Earth Models” submitted to a peer-reviewed journal are discussed.

2-D studies in chapter 2 demonstrated that the nested Voronoi partitioning shows signs of under-parametrization, which would not be ideal for the 3-D inversion. In addition, 2-D works in chapter 3 using LIAS show the significant computational cost that can be prohibitive for the 3-D problem. Therefore, this chapter applies a combination of Voronoi cells with six planes in 3-D model space to objectively introduce geological constraints and be computationally efficient. In addition, chapter 3 presented that parametrization of the noise model using trans-D AR noise models exhibits parsimonious parametrization with respect to full covariance matrices. Therefore, this chapter introduces trans-D AR noise models for 2-D gravity and magnetic data.

4.1 Introduction

Inversion of gravity and magnetic anomalies is widely used to map density and susceptibility structure in the Earth’s subsurface (Blakely 1995). The density and susceptibility anomalies are often used to identify subsurface structures, and targets appropriate for further studies in applications such as mining exploration (Martinez *et al.* 2010, Kamm *et al.* 2015), crustal structure (Aitken *et al.* 2013), and hydrocarbon exploration (Jorgensen & Kisabeth 2000, R. Krahenbuhl & Li 2009, Silva Dias *et al.* 2011, Geng *et al.* 2020, Ghalenoei *et al.* 2021a). In common 3-D potential field inversions, model space is parameterized by regular 3-D prisms (Li & Oldenburg 1996, Boulanger & Chouteau 2001, Silva Dias *et al.* 2011, Uieda & Barbosa 2012, Martinez *et al.* 2013) that over-parameterize the problem. Therefore, regularization is required to solve the inverse problem (Li & Oldenburg 1998a, Pallero *et al.* 2017, Uieda & Barbosa 2017, Maag & Li 2018). As a result, the solution and its uncertainty can reflect the constraints of the chosen regularization (Hawkins & Sambridge 2015). In such cases, the model spatial resolution is uniform while data spatial resolution is likely irregular. Therefore, irregular meshes provide advantages for model partitioning but cannot be solved via linearization. Various types of irregular meshes have been proposed for geophysical inversions, including tetrahedral 3-D meshes (Sambridge *et al.* 1995, Stenerud *et al.* 2009, Lelièvre & Farquharson 2013), adaptive-grids (Michelini 1995), deformable-layer and cell

tomography (Zhou *et al.* 2010), and Voronoi cells (Bodin *et al.* 2009). Notably, irregular meshes can significantly reduce the dimensionality of the model but may still require regularization.

Depending on geometry- and density-contrast assumptions, two types of inverse problem are commonly considered. The first type assumes known geometry but unknown density contrast or magnetic susceptibility (Li & Oldenburg 1998a, Portniaguine & Zhdanov 2002, Lelièvre *et al.* 2019). The second type assumes known density contrast but unknown geometries. The latter is commonly solved by nonlinear optimization (Camacho *et al.* 2000, R. Krahenbuhl & Li 2009, Uieda & Barbosa 2012). All these methods incur high computational cost for large kernel matrix and model vector multiplications. To reduce cost, some works suggested the fast Fourier transform for this multiplication (Wu 2016, L. Chen & Liu 2019). However, this approach requires data coverage to lie exactly above the model space, hence this is not generally applicable to gravity and magnetic inversions where model space is extended beyond data coverage to minimize edge effects. Alternatively, 3-D wavelet compression has achieved substantial gains in computational efficiency (Li & Oldenburg 2003).

To overcome regularization requirements, trans-dimensional (trans-D) sampling (Green 1995) has been applied in geophysics (Sambridge *et al.* 2006). In trans-D models, the number of parameters varies during sampling. Thereby, the method locally adapts the parametrization based on data information (Malinverno 2002, Bodin & Sambridge 2009). To date, many geophysical inversions have successfully applied trans-D models (Bodin & Sambridge 2009, Dettmer & Dosso 2012, Kolb & Lekić 2014, Piana Agostinetti *et al.* 2015, Pilia *et al.* 2020, Ray 2021), including some applications to potential-field data (Luo 2010, Izquierdo *et al.* 2020, Ghalenoei *et al.* 2021a, b).

An appropriate treatment of data noise is important for geophysical inference. In particular, correlated errors may be present (Dettmer *et al.* 2007), but noise is typically not known independently. To capture the effect of unknown, correlated noise on parameter uncertainties, a parametric noise model can be included in the inversion (Dettmer *et al.* 2012, Kolb & Lekić 2014). Parametric noise models can include scale and correlation parameters as unknowns in hierarchical Bayesian approaches. However, most previous studies are limited to correlations in 1-D.

We present a new parametrization that applies trans-D spatial and trans-D AR noise models to a 3-D non-linear joint gravity and magnetic Bayesian inversion. The spatial partitioning is constructed with a hierarchy of 3-D Voronoi cells and six planes (VP). Augmenting the Voronoi cells with six planes permits the introduction of additional prior constraints that reduce non-uniqueness. In particular, the planes are

employed to assign rock types to groups of Voronoi nodes (Ghalenoei *et al.* 2021a). Planes are chosen over other possible partitioning hierarchies, since the computational cost associated with partitioning by planes is small. Computational cost is also reduced by applying a wavelet transform to reduce the cost in evaluating the forward problem (Li & Oldenburg 2003).

The trans-D noise model is implemented by a 2-D autoregressive (AR) model with unknown AR orders for both gravity and magnetic data. The model can capture spatial correlation in the 2-D data acquisition plane. The correlations are described by two parameters for the horizontal directions and a third parameter for the diagonal direction.

The method is applied to simulated and field aerogravity and aeromagnetic data. Results for simulated data show benefits of trans-D AR models in 2-D combined with the VP partitioning. It demonstrates that various geometries of model features can be imaged. In addition, the true noise model is reasonably resolved using the proposed AR model. The field data are from offshore Abu Dhabi, United Arab Emirates (UAE), where complex salt tectonics are known to exist (Ali *et al.* 2017, Geng *et al.* 2020). The trans-D noise model is particularly suitable for these data since the high spatial sampling rates in aerial acquisition can lead to strongly correlated errors. The application demonstrates successful decorrelation of data residuals and resolution of basement and salt structures with excellent data fits.

4.2 Methods

4.2.1 Bayesian Approach and Trans-Dimensional Sampling

This section briefly reviews the Bayesian framework and the trans-D method used in this study. For more complete treatment, we recommend other works (e.g., Green 1995, Sambridge *et al.* 2006). Let $\boldsymbol{d} \in \mathbb{R}^{\boldsymbol{N}}$ be a random variable of N observed data. In addition, let $\boldsymbol{m}_k \in \mathcal{M}_k$ denote a vector of random variables. Importantly, $\boldsymbol{m}_k$ contains a choice of parametrization for spatial partitioning and data-residual noise, and various assumptions about the physics of the Earth model. Bayes' theorem (Green 1995) for a trans-D model $(\boldsymbol{m}_k|k)$ can be written

$$P(\boldsymbol{m}_k, k|\boldsymbol{d}) = \frac{P(\boldsymbol{d}|\boldsymbol{m}_k, k)\, P(\boldsymbol{m}_k|k)P(k)}{\sum_{k' \in K} \int_{\mathcal{M}} P(\boldsymbol{d}|\boldsymbol{m'}_{k'}, k')\, P(\boldsymbol{m'}_{k'}|k')P(k')d\boldsymbol{m'}_{k'}}, \tag{4.1}$$

where K is a countable set of model choices, $k \in K$ is the index of possible choices of models, $P(k)$ is the prior probability distribution function (pdf) for k, integration is over the state space $\mathcal{M}$, $P(\boldsymbol{m}_k|k)$ is the

prior for ($\boldsymbol{m}_k$) given k, $P(\boldsymbol{d}|\boldsymbol{m}_k, k)$ is the likelihood function, hereafter represented by $\mathcal{L}(\boldsymbol{m}_k, k)$, and $P(\boldsymbol{m}_k, k|\boldsymbol{d})$ is the posterior pdf of model parameters that represents the solution of the inversion. The posterior pdf can be estimated by numerical integration. For example, Green 1995 employs the Metropolis-Hastings-Green (MHG) algorithm, where a proposed model ($\boldsymbol{m'}_{k'}$) is generated by a proposal pdf $Q(\boldsymbol{m'}_{k'}|\boldsymbol{m}_k)$, and *jumps* between the various models indexed by k are permitted. Note that in this study, the Jacobian appearing in the MHG acceptance is unity and prior and proposal ratios cancel. Therefore, new states in the Markov chain are accepted or rejected based on only the likelihood ratio.

Here, three steps including *add, delete,* and *perturb* are applied in the trans-D sampling. The *add* and *delete* steps allow changing the number of model parameters. The *perturb* step keeps the model dimensionality and perturbs a parameter chosen uniformly random by a Cauchy proposal distribution.

4.2.2 Noise Parametrization with 2-D Spatial Covariance Estimation

We propose a noise model to address correlated data errors for spatial observations taken at the Earth's surface. The likelihood function $\mathcal{L}(\boldsymbol{m}_k)$ includes assumptions about data-error statistics and Gaussian noise assumptions are common, resulting in

$$\log\mathcal{L}(\boldsymbol{m}_k) = -\frac{N}{2}\log_e(2\pi) - \frac{1}{2}\log_e(|\boldsymbol{C}_d|) - \frac{1}{2}\boldsymbol{r}^T\boldsymbol{C}_d^{-1}\boldsymbol{r}, \tag{4.2}$$

where N is the number of data, $\boldsymbol{r} = \boldsymbol{d}^{\mathrm{obs}} - \boldsymbol{d}(\boldsymbol{m}_k)$ are the data residuals, and $\boldsymbol{C}_d$ is the data covariance matrix. For 2-D data, $\boldsymbol{C}_d$ includes spatial correlations in the horizontal directions. Note that these correlations can be described by dependence in the two horizontal directions and a diagonal direction. We introduce a trans-D AR model for 2-D data with the AR orders (p) estimated by data. As a result, posterior inferences include uncertainty due to the limited knowledge available for choosing the AR orders. The logarithm of the likelihood function for applying a trans-D AR model for 2-D is unchanged from the 1-D case (Dettmer *et al.* 2012)

$$\log\mathcal{L}(\boldsymbol{m}_k) \propto -N\log_e(\sigma) - \frac{1}{2}\left(\frac{\boldsymbol{d}^{\mathrm{obs}} - \boldsymbol{d}(\boldsymbol{m}_k) - \boldsymbol{\lambda}(\boldsymbol{m}_p^{\mathrm{2D,AR}})}{\sigma}\right)^T\left(\frac{\boldsymbol{d}^{\boldsymbol{obs}} - \boldsymbol{d}(\boldsymbol{m}_k) - \boldsymbol{\lambda}(\boldsymbol{m}_p^{\mathrm{2D,AR}})}{\sigma}\right), \tag{4.3}$$

where σ is an unknown standard deviation that can be implicitly computed by $\sigma = \sqrt{\frac{||\boldsymbol{r}||^2}{N}}$, where $||\ ||$ is the *L2* norm. The term $\boldsymbol{\lambda}(\boldsymbol{m}_p^{\mathrm{2D,AR}})$ are 2-D data residuals predicted by the AR process with order p and

$\frac{\boldsymbol{d}^{\mathrm{obs}} - \boldsymbol{d}(\boldsymbol{m}_k) - \boldsymbol{\lambda}(\boldsymbol{m}_p^{\mathrm{2D,AR}})}{\sigma}$ are residuals assumed to be uncorrelated due to application of the AR prediction, and standardized due to scaling by σ. The AR process produces 2-D correlations in the two horizontal (x and y) and diagonal (xy) directions. Hence, $\boldsymbol{m}_p^{\mathrm{2D,AR}}$ is decomposed into the three trans-D AR models $\boldsymbol{ARx}$, $\boldsymbol{ARy}$, and $\boldsymbol{ARxy}$. Each model is for one spatial dimension with $\boldsymbol{ARx} = \left[\varphi_1^x, \varphi_2^x, \dots, \varphi_{p_x}^x\right]$, $\boldsymbol{ARy} = \left[\varphi_1^y, \varphi_2^y, \dots, \varphi_{p_y}^y\right]$, and $\boldsymbol{ARxy} = \left[\varphi_1^{xy}, \varphi_2^{xy}, \dots, \varphi_{p_{xy}}^{xy}\right]$, where φ_j^i are AR coefficients. To implement this trans-D AR process for data stored in a 2-D array, we insert the AR coefficients as

$$\boldsymbol{m}_p^{\mathrm{2D,AR}} = \begin{bmatrix} 0 & \varphi_1^x & \varphi_2^x & \dots & \varphi_{p_x}^x \\ \varphi_1^y & \varphi_1^{xy} & 0 & 0 & 0 \\ \varphi_2^y & 0 & \varphi_2^{xy} & 0 & 0 \\ \vdots & 0 & 0 & \ddots & 0 \\ \varphi_{p_y}^y & 0 & 0 & 0 & \varphi_{p_{xy}}^{xy} \end{bmatrix}. \tag{4.4}$$

We assume the maximum orders for p_x, p_y, and p_{xy} to be 3. Therefore, $\boldsymbol{m}_p^{\mathrm{2D,AR}}$ is a square matrix of size 4 by 4. In cases where $\boldsymbol{ARx}$, $\boldsymbol{ARy}$, and $\boldsymbol{ARxy}$ have less than 3 coefficients (since the models are trans-D), zero is inserted for missing coefficients.

To apply this AR model in the inversion, it is included in the MHG sampling. For MHG updates, a direction is randomly chosen ($x, y,$ or xy), then an MHG step is randomly chosen (a*dd*, *delete*, or *perturb)* and applied to the appropriate AR coefficients. Note that an AR(0) model, $\boldsymbol{m}_0^{\mathrm{AR}}$, has no coefficient and represents uncorrelated residuals. In this case, MHG only permits an *add* step, which is sampled from the prior pdf. When the AR model reaches maximum order, no *add* step is possible and the probabilities of *add, delete, perturb* are 0, 1/3, and 2/3, respectively. In all other cases, MHG steps have equal probability of 1/3. Finally, $\boldsymbol{\lambda}(\boldsymbol{m}_p^{\mathrm{2D,AR}})$ for a proposed model is computed by

$$\lambda(\boldsymbol{m}_{\boldsymbol{p}}^{\mathrm{2D,AR}})\,(t_x, t_y) = \sum_{i=0}^{3}\sum_{j=0}^{3} m_p^{\mathrm{2D,AR}}(i,j)\, r(t_x - i, t_y - j) + \varepsilon(t_x, t_y)\,, \tag{4.5}$$

where t_x and t_y index the 2D-array data, ε is a 2-D array of uncorrelated Gaussian noise, and i and j index the matrix elements in Eq. (4.4). To maintain stationarity of the AR prediction, we define individual uniform bounded priors for the coefficients at each order. This is achieved by a preliminary test to show the appropriate prior bounds satisfy the stationarity. The stationary condition can be represented in terms of a polynomial lag with roots outside the unit circle (Mojiri *et al.* 2018). In addition, stationary AR models

require lower orders to be present before higher orders are introduced. Therefore, we apply *add* and *delete* steps for AR coefficients only at the end of the current AR model vector.

4.2.3 Hierarchical Spatial Partitioning with Voronoi Cells and Planes

Data predictions in this method are based on a grid of regular prisms, where the discretization is chosen to be smaller than the spatial resolution power of the data. To this grid, we apply 3-D Voronoi partitioning by k Voronoi nodes. The MHG sampling considers a range of k values and can jump between models indexed by the various k. For application to potential field data, the success of this approach depends on how physical properties (density contrast or susceptibility) are assigned to Voronoi cells. If little prior knowledge is applied, significant non-uniqueness can cause implausible depths and locations of rock formations. Previous works applied nested Voronoi partitioning and alpha shapes to improve the imaging of rock formations in 2-D (Ghalenoei *et al.* 2021a, b). However, nested Voronoi partitioning exhibited signs of under-parametrization when compared to alpha shapes. In addition, alpha shapes add computational burden which is currently not feasible in 3-D. Therefore, we propose a computationally efficient approach based on a hierarchy of Voronoi nodes and vertical and horizontal planes (VP) to consider the high-dimensional models for 3-D structures.

The VP parametrization is constructed from 3-D Voronoi partitioning in combination with six planes (two horizontal and four vertical) to introduce geological constraints by assigning three rock types (sedimentary rocks, rock salt, and basement rocks). This approach avoids fragmenting rock formations. The six planes are defined by six inversion parameters ($X1$, $X2$, $Y1$, $Y2$, $Z1$, and $Z2$). Each plane is parallel to an axis in 3-D cartesian coordinates. Therefore, the k Voronoi nodes are divided into 27 subspaces by the six planes (Fig. 4.1). A rock type can be assigned to each subspace. The main advantages of this approach are high computational efficiency and few parameters compared to nested Voronoi partitioning. The main disadvantage of the approach is that rock types must be assigned to the 27 subspaces which requires consideration of geological information and some experience. The prior distributions for the six plane parameters and Voronoi node locations $[\boldsymbol{x}, \boldsymbol{y}, \boldsymbol{z}]$ are bounded and uniform. The prior for density contrast is uniform over $\left(\Delta\rho^{\min}, \Delta\rho^{\max}\right)$, and the minimum and maximum bounds are distinct for rock types.

To limit parametrization complexity, basement susceptibilities are computed from density contrasts assuming an empirical ratio of $\Delta\rho/\chi$ (Li & Oldenburg 1998a). Sedimentary rocks and rock salt are assumed to have zero susceptibility. Therefore, density contrast and susceptibility models share the same structural boundaries in the joint inversion.

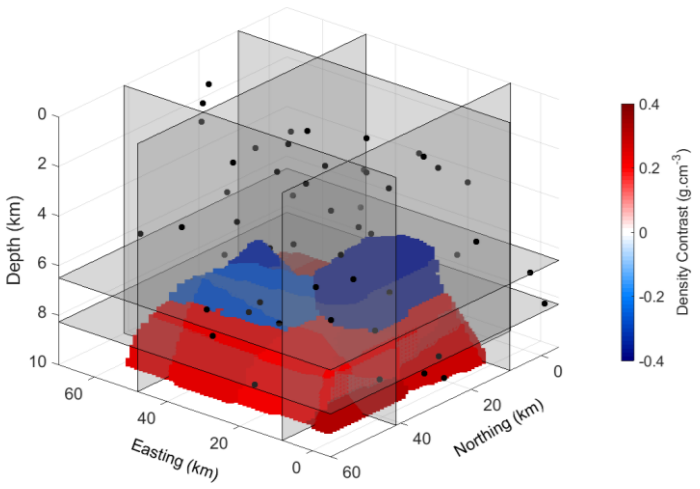

Figure 4.1. The VP parametrization. Six planes and Voronoi nodes are shown by grey planes and black dots, respectively.

4.2.4 Efficient Forward Model and Sampling

For computational efficiency, the 3-D Voronoi cells are mapped to fixed regular prisms by the nearest neighbours (NN) algorithm (Fix & Hodges 1989, Altman 1992). We use the open-source *faiss* library (J. Johnson *et al.* 2017) for an efficient NN search. In addition, the underlying regular grid permits straightforward data predictions. The gravity forward model for M regular prisms of density contrast $\Delta\rho$ is carried out by summing over the product of gravity kernel and density contrast (e.g., see Eq. 9.3 in Blakely 1995). In the same manner, magnetic anomalies are predicted from susceptibility values and the magnetic kernel (e.g., see Eq. 9.19 in Blakely 1995). Since the regular grid does not change, the kernel matrices are computed only once and saved for the inversion.

Although precomputed kernel matrices gain efficiency, large kernel matrices still cause a substantial memory and computational time burden. To overcome these issues, the matrix-vector multiplication can be performed in the wavelet domain (Li & Oldenburg 2003). In particular, by thresholding small wavelet coefficients and saving a sparse kernel matrix, memory and computational cost can be reduced significantly. The kernel matrix and model vector are transformed to the wavelet domain and multiplication makes predictions in the data domain. The efficiency gain of the wavelet compression depends on the level of wavelet transformation (sparseness) and thresholding value. The compression is applied row-wise to the kernel matrix. Hence, each row represents an approximation of the original kernel matrix. We considered various wavelets, levels, and threshold values and empirically chose the

Daubechies-4 wavelet, level 2, and threshold values of 0.001 for the gravity kernel and 0.7 for the magnetic kernel. These settings significantly speed up the matrix multiplication in the 3-D forward model by ~50x while the compression causes relative errors of 1.5%. In Fig. 4.2, data predication by the wavelet compression are compared with true data generated from a random 3-D model.

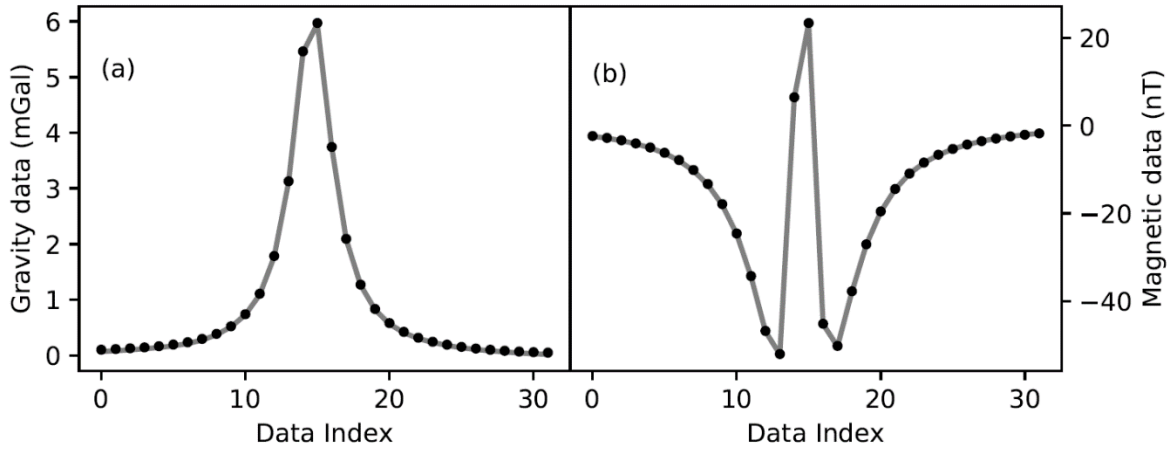

Figure 4.2. (a) A slice through gravity data computed from a sparse matrix based on wavelet compression (grey line) and true gravity data (black dots). (b) The same information for magnetic data.

The MHG sampling is combined with parallel tempering (PT; Geyer 1991, Sambridge 2014), which has been shown to improve sampling of trans-D models (Dettmer & Dosso 2012). The PT utilizes N_{PT} independent Markov chains for varies values of temperature and allowing to exchange model parameter between chains. This technique relaxes the likelihood function for large temperatures and increases the acceptance rate for model jumps. The PT is implemented via a master-worker structure with the Message Passing Interface (MPI) to parallelize the inversion. Each PT chain is run on an individual processor resulting in N_{PT} workers.

4.3 Results for Simulated Data

This 3-D simulation includes a basement and two salt bodies embedded in sedimentary rocks. The basement consists of two layers with density contrasts of $0.35\ \mathrm{g\,cm^{-3}}$ and $0.25\ \mathrm{g\,cm^{-3}}$. The two salt bodies include a pyramid and a cuboid with density contrasts of $-0.25\ \mathrm{g\,cm^{-3}}$ and $-0.35\ \mathrm{g\,cm^{-3}}$, respectively. Other regions are assumed to be sedimentary rocks with no density contrast (Fig. 4.3-a). The depths to the top of the pyramidal and cuboidal salts are 5 km and 6 km, respectively. The basement relief

has a depth of 8 km. The regular discretization for the forward model is by 64 prisms in the x, y and z directions (262,144 prisms). The size of each prism is 1,000 by 1,000 by 156 m. The density contrast priors for salt and basement are uniform over $(-0.4, -0.2)$ g cm^{-3} and $(0.2\ , 0.4)$ g cm^{-3}, respectively. We assume zero susceptibility for sedimentary rocks and salt bodies. The prior for the number of nodes (k) in the spatial discretization is uniform between 6 and 120.

Correlated Gaussian noise with a standard deviation of 4% of the maximum of the true gravity data is added to the true gravity data. The noise is correlated with $ARx = [0.6, -0.5]$, $ARy = 0.4$, and $ARxy = -0.2$. To examine the ability of the algorithm to resolve uncorrelated residuals, we assume that the noise on the magnetic data is uncorrelated Gaussian distributed with a standard deviation of 6% of the maximum of the true magnetic data. The prior pdfs for the AR coefficients are assumed to be bounded uniform and meet the stationary condition (Ghalenoei *et al.* 2021b). Bounds for the first order are $(-0.85, 0.9)$, for the second order $(-0.85, 0.1)$, and for the third order $(-0.25, 0.25)$. The prior for the AR order is uniform between 0 and 3. Empirically, AR parameters converge faster than spatial parameters. Hence, we sample the noise model at 10% of the MCMC steps. To improve burn-in, we assumed an AR(0) model during the first 5% of MHG steps. This avoids that AR parameters initially fit major data features and leads to faster convergence.

The inversion is started from a model whose parameters are randomly derived from the prior. We applied PT with 40 parallel chains including 20 chains with temperature of 1, and a temperature ratio of 1.2 for the remaining chains. During the initial *burn-in* phase, samples are not retained. During *sampling,* an ensemble of models is recorded for posterior inference. For interpretation, we consider the results in terms of averages of all recorded models (posterior mean – PM – model), various marginal distributions, and widths of 95% credibility intervals (CIs).

Our method requires assigning rock types to 27 subspaces. Here, we assign the central space as salt body, the bottom-center subspace as basement rocks, and the remaining 25 subspaces are assigned as sedimentary rocks. The inversion recorded 370,000 models.

Figure 4.3 shows the PM model for density contrast which represents the true model well with the pyramid and cuboid salt bodies clearly resolved. In addition, the basement is imaged with similar horizontal extent and at similar depth as the true model. Finally, the marginal distribution for the number of nodes (Fig. 4.3-c) peaks at 65 with uncertainty from 40 to 110. Therefore, the number of spatial

parameters used in this inversion ranges from ~160 and ~400, a significant dimension reduction over the underlying regular grid. This reduction is a key advantage of trans-D models.

Figure 4.4 represents 2-D northing and easting slices of the 3-D results for the true and PM models, 95% CI widths, and the maximum *a posteriori* (MAP) model. These slices illustrate that the two different salt geometries are both resolved by the trans-D VP parametrization. The PM slices show that the interior density contrast of the cuboid salt body is lower than that of the pyramidoid which agrees with the true model. Larger uncertainties can be found at boundaries of structures. For example, at the top of the basement where both rock salt and basement with a relatively large density contrast overlap in the ensemble of models. The MAP models are taken to be the maximum likelihood models for the peak of the k-distribution and indicate a close representation of the true model, although with sharp Voronoi polygons. These polygon shapes disappear in the PM model due to the ensemble averaging. Figure 4.5 shows the noisy simulated data, the mean of the posterior predictive distribution, and 1-D slices though the 2-D data. Both gravity and magnetic predictions fit the data closely. Note that residual correlations are visible for the gravity data. These correlations are accounted for in the by the trans-D AR model.

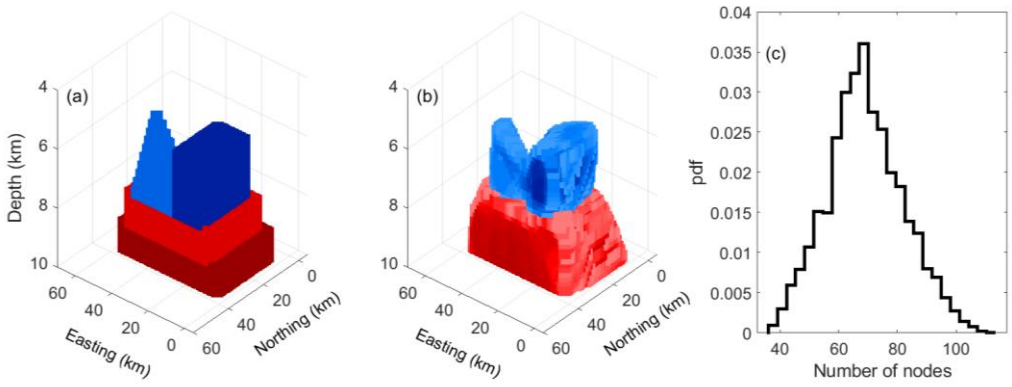

Figure 4.3. (a) True and (b) PM models. (c) Marginal distribution of the number of Voronoi nodes.

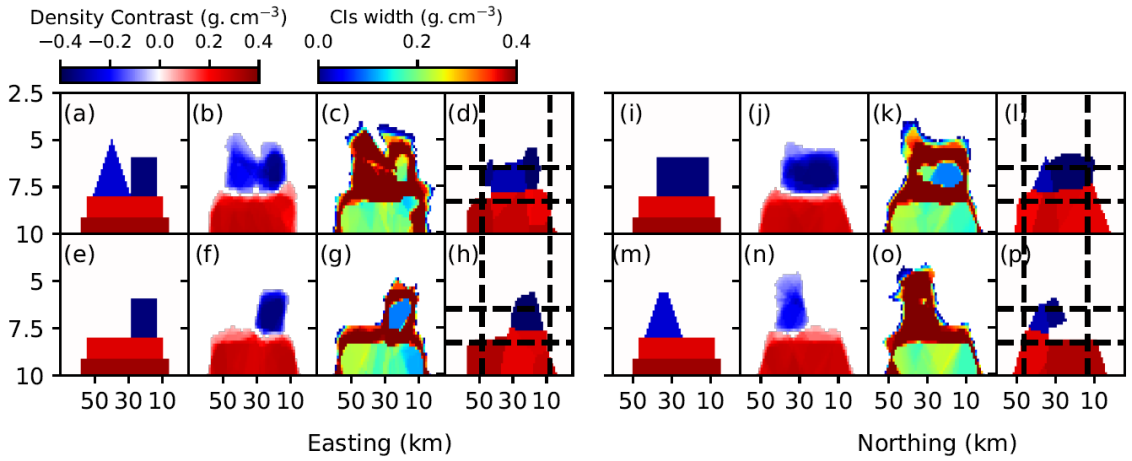

Figure 4.4. Slices at 40-km northing of (a) true, (b) PM, (c) 95% CIs widths, and (d) MAP model with locations of planes (dashed lines). (e-h) Same information for slice at 18-km northing. (i-l) Same information for slice at 24-km easting. (m-p) Same information for slice at 43-km easting.

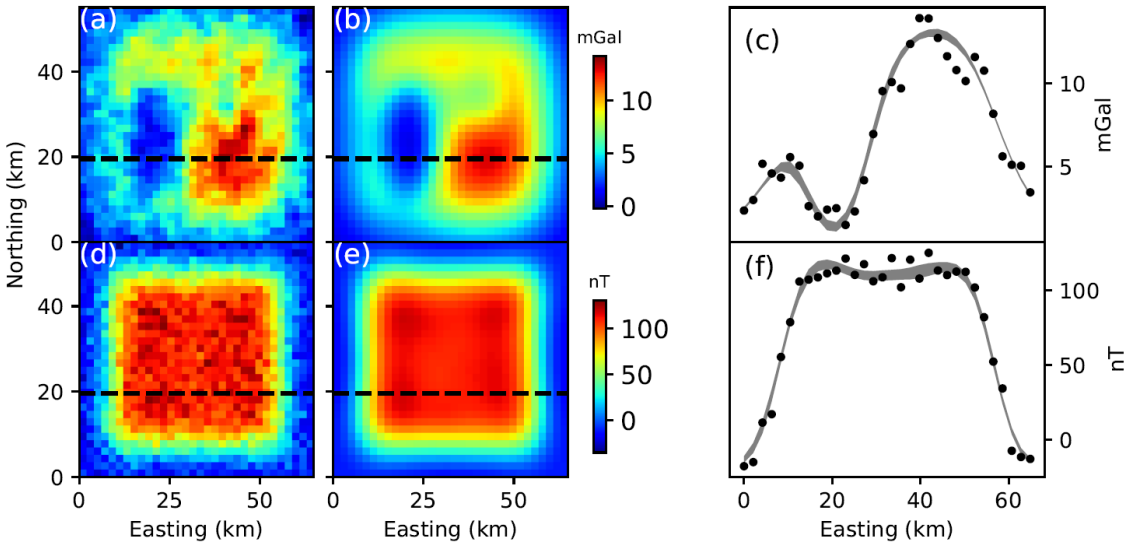

Figure 4.5. (a) Simulated noisy gravity anomaly, (b) PM of predicted gravity data, (c) slice through the 20-km northing (dashed line) of gravity data map showing simulated gravity data (black dots) and 95% CIs width of predicted gravity data (grey lines). (d-f) The same information for the magnetic anomaly.

Figure 4.6 summarizes the results for the noise model in terms of marginal distributions. The simulated gravity data contain correlated noise with true orders of 2, 1, and 1 for $\boldsymbol{ARx}$, $\boldsymbol{ARy}$, and $\boldsymbol{ARxy}$, respectively. These true AR orders are correctly resolved by the trans-D model with only modest uncertainty. The marginal distributions for the 2-D AR coefficients (Fig. 4.6) are also resolved with modes

near true values. For magnetic data, uncorrelated errors were assumed. In that case, the 2-D AR model infers zero-order for $\boldsymbol{ARx}$ and $\boldsymbol{ARy}$ (Fig. 4.6-g to i) and order 1 for $\boldsymbol{ARxy}$. The marginal distributions for coefficients show peaks near zero (Fig. 4.6-j to l) in all cases. Therefore, even where the trans-D model permits higher AR orders, the predictions are nearly uncorrelated.

In order to examine how the trans-D AR model improves inversion results, the autocorrelation of raw and standardized residuals are shown (Fig. 4.7). We can see that gravity raw residuals exhibit significant correlation (Fig. 4.7-a). The application of the trans-D AR model in 2-D successfully reduces correlation in standardized residuals (Fig. 4.7-b). For magnetic data, raw and standardized residuals are uncorrelated (Fig. 4.7-e and f). Finally, histograms for standardized residuals closely match the standard normal distributions (Fig. 4.7-d and h). In summary, the trans-D AR model for 2-D data successfully quantifies the noise process and ensures that assumptions about noise are met in the inversion. This instills confidence that estimated parameter values and uncertainties are appropriate.

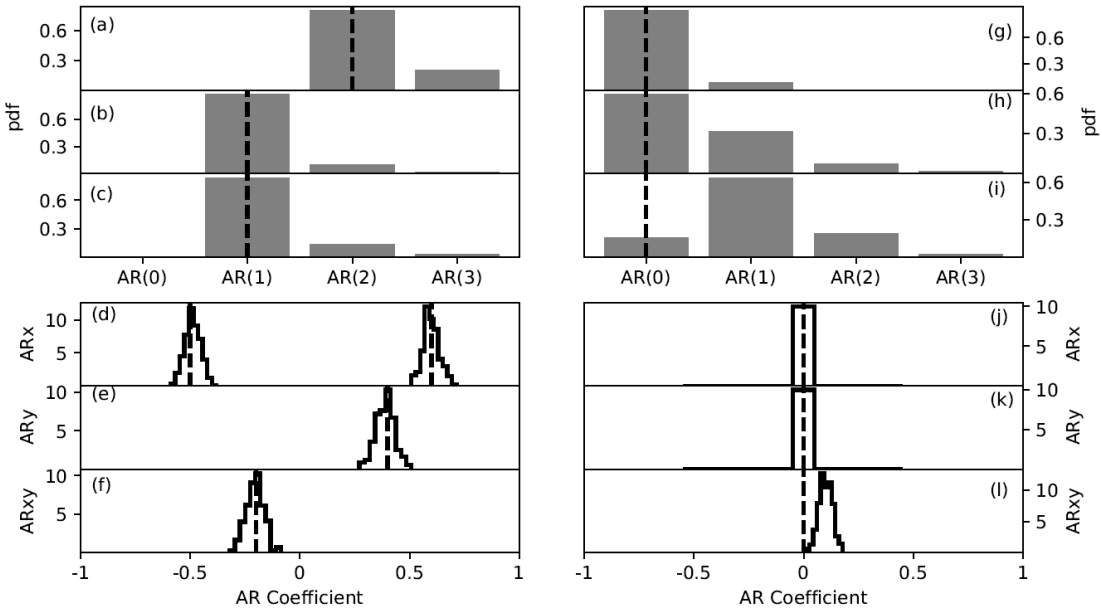

Figure 4.6. Marginal probability distributions of gravity AR model orders for (a) $\boldsymbol{ARx}$, (b) $\boldsymbol{ARy}$, and (c) $\boldsymbol{ARxy}$, and (d-f) marginal probability distributions the corresponding coefficients at mode of the AR order marginals. True AR orders and coefficients are also shown (dashed lines). (g-l) The same information for magnetic AR models.

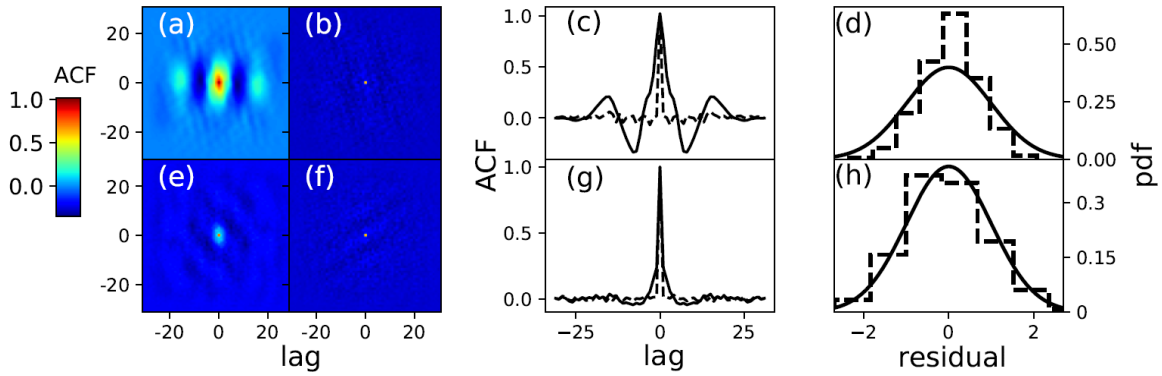

Figure 4.7. Spatial autocorrelation of (a) raw and (b) standardized residuals for gravity. (c) The middle row of maps in (a) and (b) with solid and dashed lines, respectively. (d) Histograms of standardized gravity residuals (dashed line), and the standard normal distribution (solid line). (e-h) The same information for magnetic residuals.

4.4 Field Data in 3-D Application

This section presents results for the application of the 3-D trans-D inversion to aerogravity and aeromagnetic data over the Ghasha oilfield offshore Abu Dhabi, UAE. The study area includes complex salt diapirs and basement topography which makes it an ideal study site for the proposed method. Results are interpreted in terms Earth structure and noise model.

The gravity and magnetic data were acquired by Sander Geophysics Ltd. (SGL) for ADNOC in 2007-2008 (Ali *et al.* 2017). Data corrections were applied in terms of Eötvös, latitude, free air, Bouguer, the curvature of the Earth, terrain, static, and levelling corrections. The terrain correction uses a density of 2.6 g cm^{-3} for land and terrain-topographic data obtained by the Shuttle Radar Topography Mission (SRTM). The seawater-depth correction uses a density of 1.02 g cm^{-3} over marine areas from bathymetric data provided by the Gridded Bathymetric Chart of the Oceans 1-minute grid. Regional effects were computed and removed by applying a low-pass filter with a 3-km half-wavelength and upward continued to 20 km above sea level. Ultimately, data were gridded at 1 km by 1 km.

The aeromagnetic survey applied Caesium optically pumped magnetometers with a 0.001 nano Tesla (nT) sensitivity and sensor noise of 0.02 nT. Data corrections included removal of the International Geomagnetic Reference Field (IGRF), leveling error corrections, and diurnal fluctuation corrections. Ultimately, differentially-reduced-to-the-pole (DRTP) data were calculated (Salem & Ali 2016) and provided to us and are used for the inversion.

We studied a region 65-km E-W extent, and 50-km N-S extend, including the Ghasha oilfield and diapiric island of Sir Bani Yas (Fig. 4.8). The area is sampled by a grid of 32 by 32 points for gravity and magnetic data. The model space spans dimensions of 75 km $\times$ 60 km $\times$ 10 km. The regular grid for forward computations has 64 by 64 by 64 regular prisms. The model space is extended by 5 km beyond the data sampling on all sides in the horizontal direction to reduce the effects from subsurface structures beyond the data region. The depth range of the model space is from 0 to 10 km. The field-data inversion is carried out with the same prior pdfs and assumptions as were applied for simulated data, except for the prior pdf for salt body which is uniform over $(-0.4, -0.05)\ \mathrm{g\,cm^{-3}}$. The MHG sampling with PT was based on 40 chains computed in parallel via MPI. The posterior sample includes 800,000 models and the total run time was 5 days.

Figure 4.8 shows observed and predicted data with good agreement throughout the survey area. For more detailed consideration, EW slices at 2718-km northing and NS slices at 682-km easting are also shown (Fig. 4.8-c and f). The slices illustrate that the predicted data capture the main features of the field data. In addition, the width of the 95% CI of the posterior predictive distribution matches smaller fluctuations in the data. However, some smaller features are not captured by our model. For example, the location of the Sir Bani Yas Island shows a negative gravity anomaly with a spatial extent of about 8 pixels. This feature is not captured in the data prediction.

Figure 4.9 is a 3-D image of the PM model for density contrast and shows a projection of the gravity data at the Earth's surface. In this image, only rock salts with density contrasts lower than -0.13 $\mathrm{g\,cm^{-3}}$ are shown. This aims to better visualize the salt boundary with sedimentary rocks. The value of -0.13 $\mathrm{g\,cm^{-3}}$ is based on the Infracambrian Hormuz salt outcrops in the Jabal Dhanna peninsula and on Sir Bani Yas Island (Geng *et al.* 2020). Interestingly, the 3-D model shows dome shapes for both salt diapirs. The locations of two salt diapirs are consistent with the locations of two negative peaks in the observed gravity anomaly. The basement underlying the salt is undulating, and its minimum depth reaches around 8.5 km.

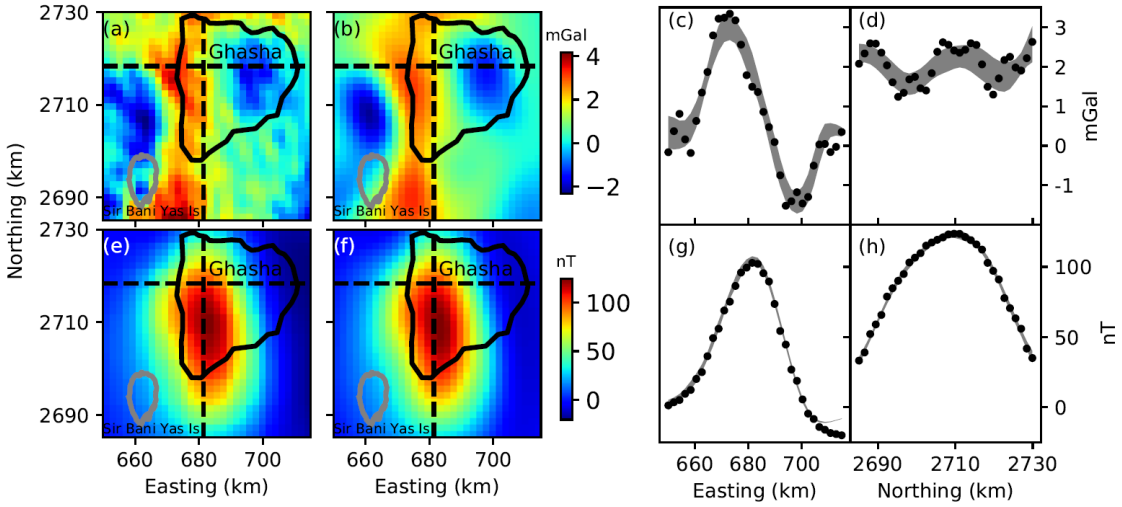

Figure 4.8. (a) Gravity anomaly, (b) PM of predicted gravity data, (c) slice through 2718-km northing (dashed line) of the gravity anomaly map showing observed gravity anomaly (black dots) and 95% CI widths from predicted gravity data (grey area), (d) slice through 682-km easting. (e-h) The same information for the magnetic anomaly. Coastlines (grey) and outlines of the Ghasha oilfield (solid black) are also shown in (a,b,e, and f). The map coordinates are in UTM Zone 39 N, WGS84.

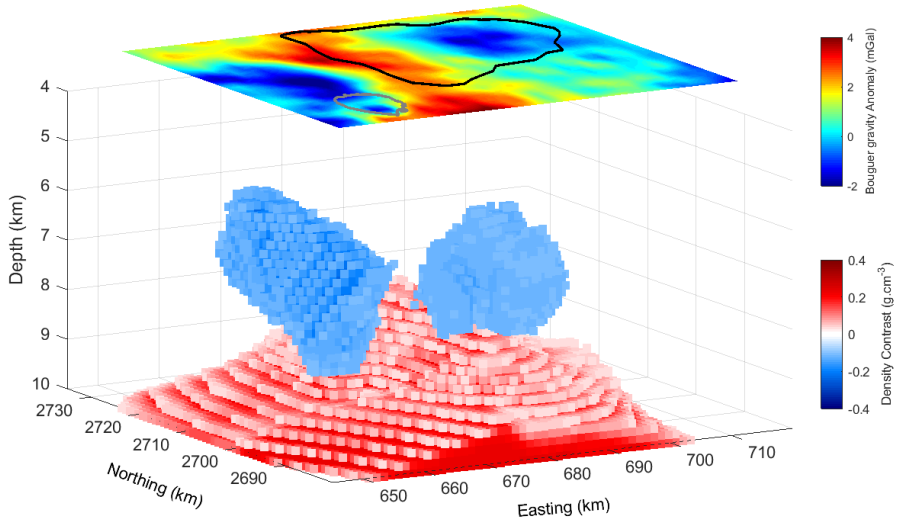

Figure 4.9. 3-D PM model for density contrast, and a projection of the observed gravity anomaly at the Earth's surface. The basement is represented with positive density contrast (red colors), and two salt diapirs are imaged with negative density contrast (blue colors). The background white color shows sedimentary rocks.

Figure 4.10 shows posterior results in terms of 2-D slices through the 3-D volume. The PM models, the width of 95% CIs, and the marginal for the number of nodes are shown. The slice at 2700-km northing shows two salt structures with the shallower at 4.7-km depth. This depth agrees well with the deepest well that reached the Khuff Formation at 4.64-km depth (Geng *et al.* 2020). At this slice, the salt body is imaged with no high negative peak in gravity data because the negative anomaly is compensated with relatively large positive density from the basement topography which can be estimated from the large positive magnetic anomaly at this area. The slice at 662-km easting indicates a salt body with high negative density contrasts and is consistent with the high negative gravity anomaly (from 2700-km to 2720-km northing). Interestingly, the extent of salt in the horizontal slice of the PM model at the depth of 4.7 km matches the boundary of the Ghasha oilfield (Fig. 4.10-e). The maps of the widths of 95% CIs show the largest uncertainty close to the boundary between basement rocks and rock salt due to overlapping of both positive and negative density contrast at the same space in the ensemble of posterior models. The marginal probability distribution of the number of nodes peaks at 45 nodes with uncertainty from 30 to 90 nodes (Fig. 4.10-g).

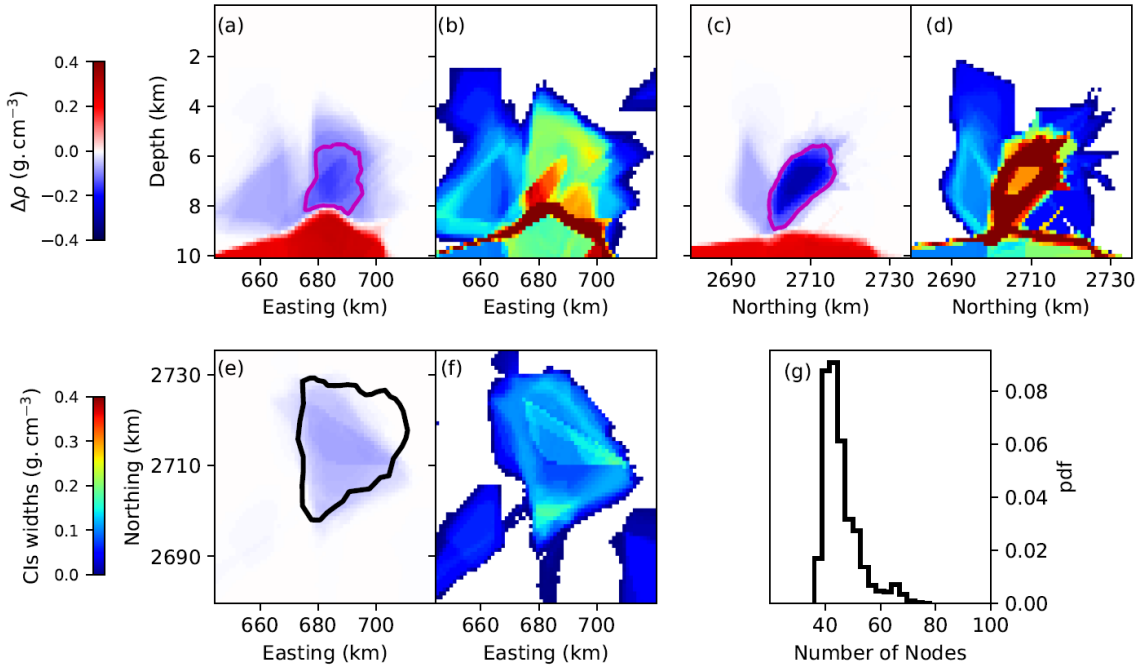

Figure 4.10. Slices through the PM model and 95% CI widths at 2700-km northing, 662-km easting, and 4.7-km depth in (a-b), (c-d), and (e-f), respectively. The density contrast of –0.13 g cm^{-3} (magenta line) and the boundary of Ghasha oilfield (black line) are outlined. (g) Marginal probability distribution of k.

To verify the depth and shape of the salt bodies predicted by the PM model, we extracted cross-sections from the inverted density contrast model along with the seismic profiles that cross the Ghasha field (Fig. 4.11). Location of the profiles are shown in Fig. 4.8 . The seismic profiles and the GH7 well do not image or reach the salt bodies due to thick sedimentary cover. However, they show that the depth and morphology of the salt bodies from the density contrast model are generally consistent with those interpreted from the seismic profiles. For example, the density contrast model along the seismic line 1 (Fig. 4.11-a) indicates very low probability salt bodies (negative density contrasts close to zero), which is in agreement with the seismic profile 1 (Fig. 4.11-b). However, the density contrast model along seismic line 2 suggests a low-density body with density contrast of <-0.13 g cm^{-3} above the basement (Fig. 4.11-c). We interpreted this body as a salt body. Though the body is not imaged by the seismic line 2 (Fig. 4.11-d) due to probably lack of acoustic contrast or the quality of seismic data below the Khuff Formation. Nevertheless, the density contrast model indicates that this body occurs between Khuff Formation and the basement and has a geometry that corresponds well with the shape of the western side of the Ghasha field. Therefore, there appears to be a correlation between the boundaries of the oilfield and the salt body.

The results for the trans-D AR model for 2-D data are shown in Fig. 4.12. Gravity residuals are strongly correlated with modes at third, second, and first order for $\boldsymbol{ARx}$, $\boldsymbol{ARy}$, and $\boldsymbol{ARxy}$, respectively. Magnetic residuals show correlation at the first order in all three directions. The marginal distributions of the AR coefficients imply the first coefficient is at values near 0.9 while the other coefficients are significantly lower. This means that correlations exhibit exponential decay.

Figure 4.13 shows the autocorrelation of raw and standardized residuals to investigate the performance of the spatial trans-D AR model. The results show (Fig. 4.13-a, b, e, and f) that our method successfully reduces the correlation of residuals for gravity and the magnetic data. The exponential decay mentioned previously is clear when considering the autocovariance function of the residuals (Fig. 4.13-c and g). Finally, the Gaussianity of standardized residuals agrees well with the standard normal distribution. Therefore, the trans-D AR model for 2-D spatial data significantly improves noise treatment in this study.

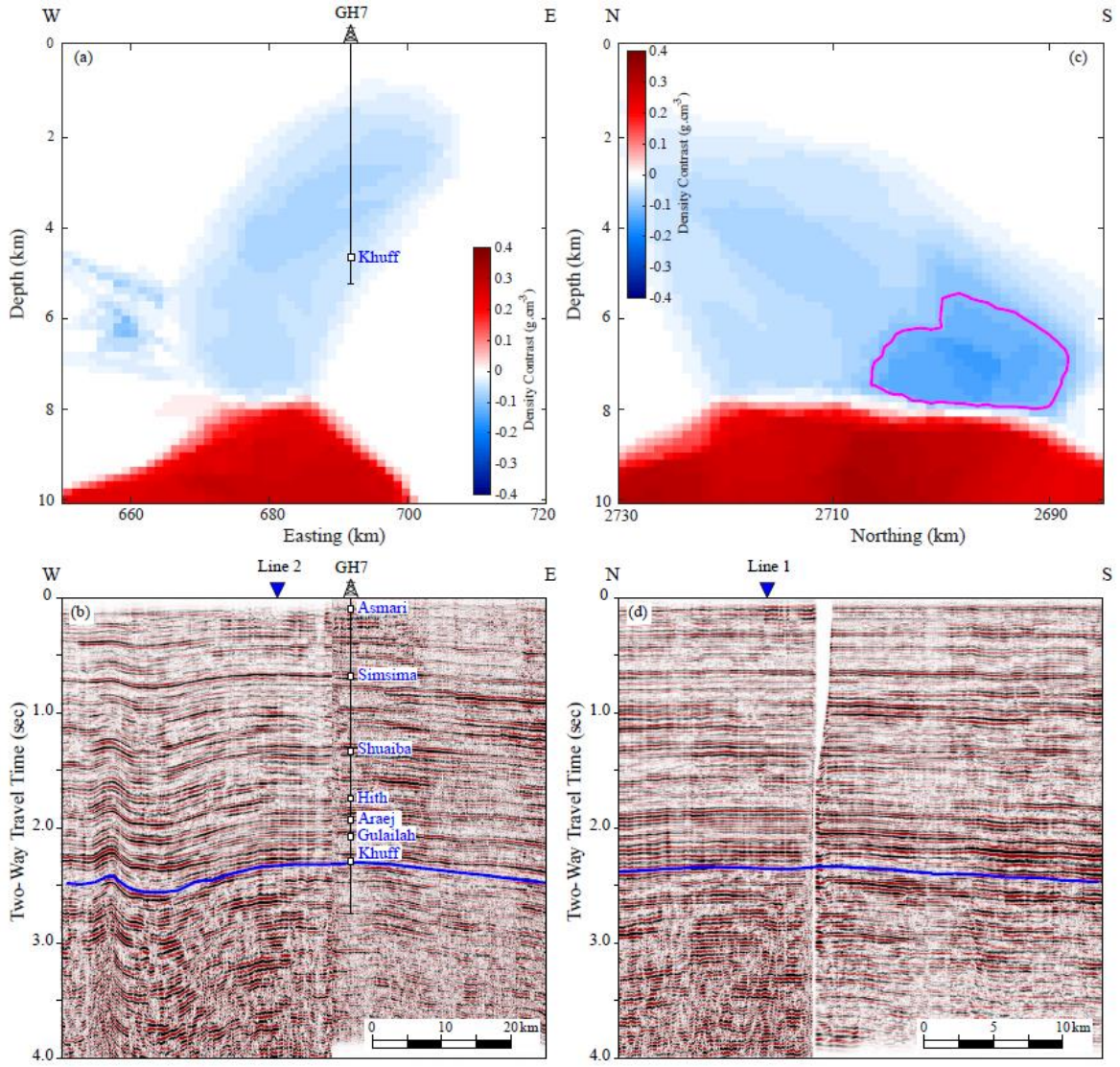

Figure 4.11. (a) PM model showing inverted density along seismic profile 1 at 2718-km Northing. (b) Seismic profile 1, which crosses GH7. (c) PM model showing inverted density along seismic line 2 at 682-km Easting. (d) Seismic profile 2. The magenta line on the density model corresponds on density contrast of -0.13 g cm^{-3}, which is interpreted as the top of the salt body. The blue lines on the seismic profiles depict top Khuff Formation, the deepest formation penetrated by the GH7 well. The inverted triangles on the seismic profiles show seismic lines that cross this profile. For location of the profiles, see Fig. 4.8.

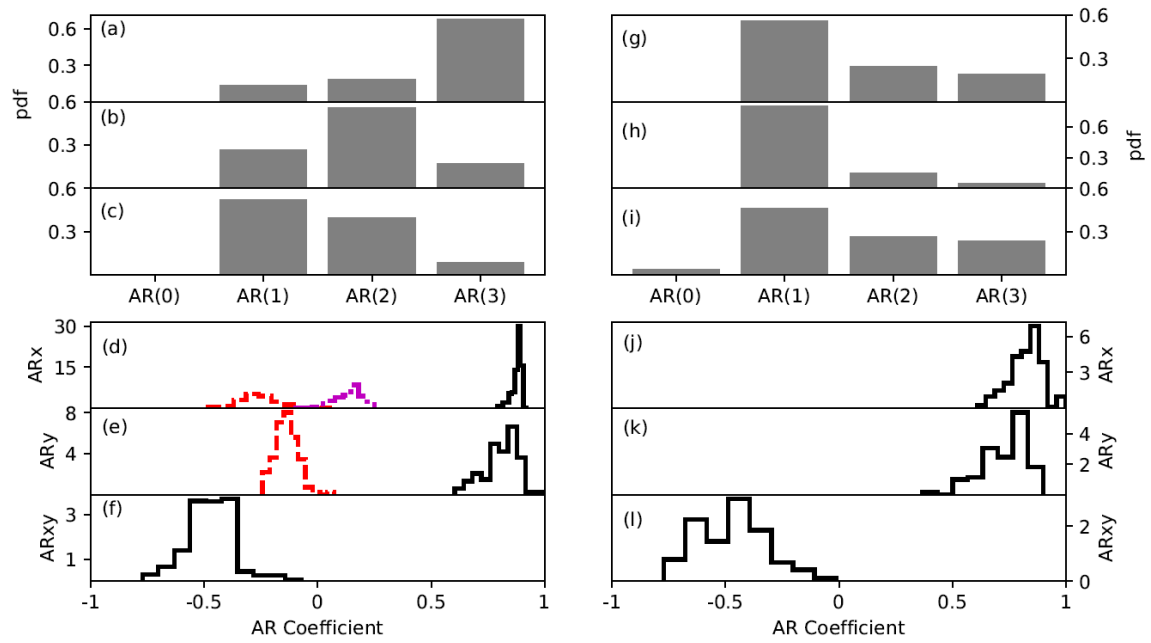

Figure 4.12. The marginal probability distributions of gravity AR model order for (a) $\boldsymbol{ARx}$, (b) $\boldsymbol{ARy}$, and (c) $\boldsymbol{ARxy}$. The marginal probability distributions of sampled gravity AR coefficients for (d) $\boldsymbol{ARx}$, (e) $\boldsymbol{ARy}$, and (f) $\boldsymbol{ARxy}$. The black, red, and magenta distributions are for the first, the second, and the third AR coefficient, respectively. (g-l) The same information but for magnetic AR model.

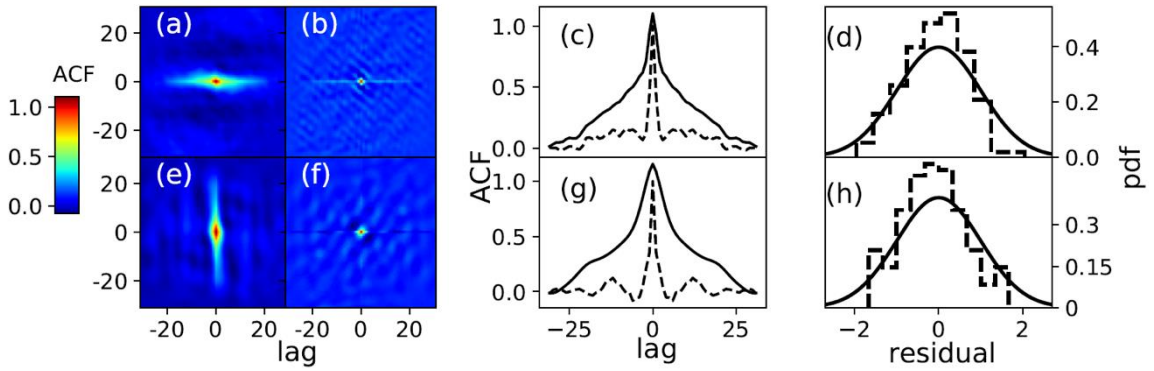

Figure 4.13. Autocorrelation of (a) gravity raw residuals, (b) gravity standardized residuals. (c) A slice through the middle row in map (a) is shown (solid line) and a slice of map (b) is shown (dashed line). (d) Histogram of standardized gravity residuals (dashed line) and the standard normal distribution (solid line). (e-h) The same information for magnetic residuals.

4.5 Conclusions and Discussion

In joint gravity and magnetic inversion, a more complex model of the Earth's subsurface requires a parametrization with a higher spatial resolution. In addition, data spatial resolution varies throughout the model space and a parametrization should locally adapt to the resolving power of the data. Trans-D models provide variable spatial resolution based on data information without requiring regularization.

For the inversion of gravity and magnetic anomalies, we employed hierarchical partitioning of 3-D space based on Voronoi nodes and six planes to parametrize the spatial Earth model. The simulated data and field data inversions produced clear spatial resolution of the basement and multiple salt diapirs and fit data well. These results were achieved with small numbers of Voronoi nodes (peaking at 45 nodes) for the field data. Therefore, the parametrization is parsimonious with far fewer parameters than required for regular grids. As a result, the numerical integration via MHG sampling is possible.

Addressing error correlations in potential field data measured at the Earth's surface is more complex than similar approaches in 1-D data (time series or spatial transects). We introduced a trans-D AR noise model for 2-D data to estimate correlations in two horizontal and one diagonal directions. We showed that this trans-D AR noise model can account for complex noise correlations with up to three AR coefficients in each of the three directions. *A posteriori* residual analysis was applied to show that the trans-D AR model dramatically reduced the correlations in residuals. Therefore, the density estimates account for noise correlations.

A limitation of the method is the requirement to assign rock types to the 27 sub-spaces created by the six planes (Ghalenoei *et al.* 2021c). Other hierarchical models are possible to reduce ambiguity in this process. For example, the combination of linear interpolation and alpha shapes (Ghalenoei *et al.* 2021b) was successfully applied to a 2-D problem. However, the method is associated with higher computational cost. Alternatively, nested Voronoi partitioning (Ghalenoei *et al.* 2021a) may also be applied in 3-D applications, which could be beneficial for 3-D inversions where many diapir structures may be present.

In conclusion, our study demonstrates that data-driven estimation of 3-D density and susceptibility distributions in the Earth is improved by incorporating prior knowledge in the spatial parametrization and by carefully parametrizing the typically highly correlated noise on data.

5 Concluding Remarks

This dissertation presents the use of trans-D models in the inversion of potential field data for the application of basement and salt modeling. To reach the goal of 3-D probabilistic inversion, I first developed trans-D parametrizations for the Earth and data residuals noise in 2-D. Subsequently, the knowledge gained from these 2-D studies informed the design of a method for the probabilistic 3-D inversion in chapter 4. The results reveal basement and salt structures with the advantage of variable spatial resolution based on a parsimonious parametrization. Of note is that general shapes in salt and basement can be recovered and that the non-uniqueness is addressed by Bayesian uncertainty quantification.

This work studied two different forms of spatial partitioning for 2-D inversions to choose a basis for fully nonlinear, probabilistic method for 3-D inversion. Chapter 2 advances the joint inversion of gravity and magnetic data using a nested Voronoi partitioning with three parent nodes (NV3) and empirical estimation of full data covariance matrices that include theory and observational errors to account for spatially correlated noise. I showed that simple trans-D Voronoi partitioning does not produce reasonable models for diapirs on top of the basement topography. With NV3, meaningful prior information can be specified for each rock type which reduces non-uniqueness, leading to better subsurface images. A limitation of this method is that more complex salt structures may not be captured well, and that empirical noise estimation requires tuning which may underestimate parameter uncertainties. Therefore, chapter 3 considers LIAS spatial partitioning and shows that the alpha shapes can capture more complex shapes of subsurface structures with a few parameters and better data fits. In addition, a trans-D AR model more completely captures model uncertainty due to correlated data residuals. We demonstrated that *a posteriori* residual analysis shows a significant reduction in the correlation of residuals while reducing tuning and dependence on initial noise assumptions. The major benefit of the trans-D AR noise model is that it captures noise-model complexity with up to three parameters without requiring empirical damping and scaling that are used for the full data covariance matrix. Note that this trans-D AR model is very general and has the potential to be applied to any spatial or time-series data.

While LIAS holds significant potential, it was not efficient enough for the application to 3-D data. Therefore, Chapter 4 combines hierarchical spatial partitioning with Voronoi cells and planes (VP) for 3-D inversion that showed advantages of reducing non-uniqueness issues and computational convenience. In

addition, I extended the trans-D AR model to address correlated 2-D gravity and magnetic data errors. This study also addressed the computational burden by wavelet compression in the forward model.

Generally, the proposed spatial partitioning forms locally adapt the model complexity based on data information without requiring global or local smoothing or damping constraints. They demonstrated a parsimonious parametrization that avoided under- and/or over-parametrization.

The hierarchical spatial partitioning choices applied in this thesis work well for imaging locations with individual salt diapirs in the presence of basement topography. However, other applications will require additional work. For example, additional modifications are required for large-scale problems where there may be several salt diapirs. Therefore, this thesis recommends the following points to consider in future studies:

- The advantage of different parent node approaches includes the ability to address more rock types (e.g., to describe other tectonic regimes, including those that may be of interest in geothermal exploration). We recommend applying a trans-D parametrization when both the numbers of child and parent nodes are unknown as this can improve the objectivity of the solution in future studies.
- The implementation of LIAS in 2-D inversion was relatively slow. Modification of this model choice to speed up the sampling could be potentially beneficial in 3-D applications. I recommend implementing linear interpolation and alpha shape using one-time Delaunay triangulation to accelerate the convergence.
- Investigating higher orders of AR model for gravity data measured in this case study is also recommended in future research.
- In our 3-D study, a limitation of the method is the requirement to assign rock types to the 27 sub-spaces created by the six planes (Ghalenoei *et al.* 2021c). Other hierarchical models are possible to reduce ambiguity in this process. For example, rock types assigned in subspaces between six planes can be unknown in future works. In addition, the number of planes can also be unknown and derived by data information. This can help to resolve more salt diapirs over larger data regions.
- Alternatively, the nested Voronoi partitioning may also be applied in 3-D applications, which could be beneficial for 3-D inversions where many diapir structures may be present.
- Considering other zero elements of the trans-D AR model in the 2-D array can provide a more objective solution and enhance the decorrelation process and the Gaussianity.

Bibliography

Aitken, A.R.A., Salmon, M.L. & Kennett, B.L.N. (2013) Australia's Moho: A test of the usefulness of gravity modelling for the determination of Moho depth. *Tectonophysics* Moho: 100 years after Andrija Mohorovicic, **609**, 468–479. doi:10.1016/j.tecto.2012.06.049

Al-Garni, M.A., Gobashy, M. & Arabia, S. (2010) Ground Magnetic Investigation of Subsurface Structures Affecting Wadi Thuwal Area, KSA. doi:10.4197/ear.21-2.7

Al-Husseini, M. (2000) Origin of the Arabian Plate Structures: Amar Collision and Najd Rift. *GeoArabia*, **5**, 527–542.

Ali, M.Y., Fairhead, J.D., Green, C.M. & Noufal, A. (2017) Basement structure of the United Arab Emirates derived from an analysis of regional gravity and aeromagnetic database. *Tectonophysics*, **712–713**, 503–522. doi:10.1016/j.tecto.2017.06.006

Ali, M.Y. & Farid, A. (2016) Cretaceous - Neogene Structural Evolution of se Abu Dhabi, United Arab Emirates. *Journal of Petroleum Geology*, **39**, 221–245. doi:10.1111/jpg.12644

Altman, N.S. (1992) An Introduction to Kernel and Nearest-Neighbor Nonparametric Regression. *The American Statistician*, **46**, 175–185, [American Statistical Association, Taylor & Francis, Ltd.]. doi:10.2307/2685209

Amey, R.M.J., Hooper, A. & Morishita, Y. (2019) Going to Any Lengths: Solving for Fault Size and Fractal Slip for the 2016, Mw 6.2 Central Tottori Earthquake, Japan, Using a Transdimensional Inversion Scheme. *Journal of Geophysical Research: Solid Earth*, **124**, 4001–4016. doi:https://doi.org/10.1029/2018JB016434

Arkani-Hamed, J. (2006) Differential reduction to the pole: Revisited. *GEOPHYSICS*, **72**, L13–L20, Society of Exploration Geophysicists. doi:10.1190/1.2399370

Aster, R.C., Borchers, B. & Thurber, C.H. (2016) *Parameter Estimation and Inverse Problems*, Paperback reprint of hardcover 2nd ed., 2011 edition., Amsterdam: Academic Press.

Barnoud, A., Cayol, V., Niess, V., Cârloganu, C., Lelièvre, P., Labazuy, P. & Le Ménédeu, E. (2019) Bayesian joint muographic and gravimetric inversion applied to volcanoes. *Geophysical Journal International*, **218**, 2179–2194. doi:10.1093/gji/ggz300

Bayes, Mr. & Price, Mr. (1763) An Essay towards Solving a Problem in the Doctrine of Chances. By the Late Rev. Mr. Bayes, F. R. S. Communicated by Mr. Price, in a Letter to John Canton, A. M. F. R. S. *Philosophical Transactions (1683-1775)*, **53**, 370–418.

Beaty, K.S., Schmitt, D.R. & Sacchi, M. (2002) Simulated annealing inversion of multimode Rayleigh wave dispersion curves for geological structure. *Geophysical Journal International*, **151**, 622–631. doi:10.1046/j.1365-246X.2002.01809.x

Belcourt, J., Holland, C.W., Dosso, S.E., Dettmer, J. & Goff, J.A. (2020) Depth-Dependent Geoacoustic Inferences With Dispersion at the New England Mud Patch via Reflection Coefficient Inversion. *IEEE Journal of Oceanic Engineering*, **45**, 69–91, Presented at the IEEE Journal of Oceanic Engineering. doi:10.1109/JOE.2019.2900115

Biswas, A. (2015) Interpretation of residual gravity anomaly caused by simple shaped bodies using very fast simulated annealing global optimization. *Geoscience Frontiers* Special Issue: Geoinformation techniques in natural hazard modeling, **6**, 875–893. doi:10.1016/j.gsf.2015.03.001

Blakely, R.J. (1995) *Potential Theory in Gravity and Magnetic Applications*, Cambridge: Cambridge University Press. doi:10.1017/CBO9780511549816

Bodin & Sambridge. (2009) Seismic tomography with the reversible jump algorithm. *Geophysical Journal International*, **178**, 1411–1436. doi:10.1111/j.1365-246X.2009.04226.x

Bodin, Sambridge, M. & Gallagher, K. (2009) A self-parametrizing partition model approach to tomographic inverse problems. *Inverse Problems*, **25**, 055009, IOP Publishing. doi:10.1088/0266-5611/25/5/055009

Bodin, T., Sambridge, M., Tkalčić, H., Arroucau, P., Gallagher, K. & Rawlinson, N. (2012) Transdimensional inversion of receiver functions and surface wave dispersion. *Journal of Geophysical Research: Solid Earth*, **117**. doi:https://doi.org/10.1029/2011JB008560

Bosch, M., Meza, R., Jiménez, R. & Hönig, A. (2006) Joint gravity and magnetic inversion in 3D using Monte Carlo methods. *GEOPHYSICS*, **71**, G153–G156, Society of Exploration Geophysicists. doi:10.1190/1.2209952

Boulanger, O. & Chouteau, M. (2001) Constraints in 3D gravity inversion. *Geophysical Prospecting*, **49**, 265–280. doi:10.1046/j.1365-2478.2001.00254.x

Brooks, S., Gelman, A., Jones, G. & Meng, X.-L. (Eds.). (2011) *Handbook of Markov Chain Monte Carlo*, 1st edition., Boca Raton: Chapman and Hall/CRC.

Camacho, A., Montesinos, F. & Vieira, R. (2000) Gravity inversion by means of growing bodies. *GEOPHYSICS*, **65**, 95–101. doi:10.1190/1.1444729

Chen, L. & Liu, L. (2019) Fast and accurate forward modelling of gravity field using prismatic grids. *Geophysical Journal International*, **216**, 1062–1071. doi:10.1093/gji/ggy480

Chen, X., Du, Y., Liu, Z., Zhao, W. & Chen, X. (2018) Inversion of Density Interfaces Using the Pseudo-Backpropagation Neural Network Method. *Pure Appl. Geophys.*, 1–21. doi:10.1007/s00024-018-1889-7

Darijani, M., Farquharson, C.G. & Lelièvre, P.G. (2021) Joint and constrained inversion of magnetic and gravity data: A case history from the McArthur River area, Canada. *GEOPHYSICS*, **86**, B79–B95, Society of Exploration Geophysicists. doi:10.1190/geo2019-0818.1

Delaunay, B. (1934) Sur la Sphere Vide. *Izv. Akad. Nauk SSSR, Otdelenie Matematicheskii i Estestvennyka Nauk*, **7**, 793–800.

Denison, D. G. T., Adams, N.M., Holmes, C.C. & Hand, D.J. (2002) Bayesian partition modelling. *Comput. Stat. Data Anal.*, **38**, 475–485. doi:10.1016/S0167-9473(01)00073-1

Denison, David G. T., Holmes, C.C., Mallick, B.K. & Smith, A.F.M. (2002) *Bayesian Methods for Nonlinear Classification and Regression*, 1st edition., Chichester, England ; New York, NY: Wiley.

Dettmer, J., Benavente, R., Cummins, P.R. & Sambridge. (2014) Trans-dimensional finite-fault inversion. *Geophys J Int*, **199**, 735–751. doi:10.1093/gji/ggu280

Dettmer, J. & Dosso, S.E. (2012) Trans-dimensional matched-field geoacoustic inversion with hierarchical error models and interacting Markov chains. *The Journal of the Acoustical Society of America*, **132**, 2239–2250. doi:10.1121/1.4746016

Dettmer, J., Dosso, S.E. & Holland, C.W. (2007) Uncertainty estimation in seismo-acoustic reflection travel time inversion. *The Journal of the Acoustical Society of America*, **122**, 161–176. doi:10.1121/1.2736514

Dettmer, J., Molnar, S., Steininger, G., Dosso, S.E. & Cassidy, J.F. (2012) Trans-dimensional inversion of microtremor array dispersion data with hierarchical autoregressive error models. *Geophysical Journal International*, **188**, 719–734. doi:https://doi.org/10.1111/j.1365-246X.2011.05302.x

Edelsbrunner, H., Kirkpatrick, D. & Seidel, R. (1983) On the shape of a set of points in the plane. *IEEE Transactions on Information Theory*, **29**, 551–559, Presented at the IEEE Transactions on Information Theory. doi:10.1109/TIT.1983.1056714

Farquharson, C.G., Ash, M.R. & Miller, H.G. (2008) Geologically constrained gravity inversion for the Voisey's Bay ovoid deposit. *The Leading Edge*, **27**, 64–69, Society of Exploration Geophysicists. doi:10.1190/1.2831681

Farquharson, C.G. & Oldenburg, D.W. (1998) Non-linear inversion using general measures of data misfit and model structure. *Geophys J Int*, **134**, 213–227, Oxford Academic. doi:10.1046/j.1365-246x.1998.00555.x

Fix, E. & Hodges, J.L. (1989) Discriminatory Analysis. Nonparametric Discrimination: Consistency Properties. *International Statistical Review / Revue Internationale de Statistique*, **57**, 238–247, [Wiley, International Statistical Institute (ISI)]. doi:10.2307/1403797

Fournier, D. & Oldenburg, D.W. (2019) Inversion using spatially variable mixed ℓp norms. *Geophys J Int*, **218**, 268–282, Oxford Academic. doi:10.1093/gji/ggz156

Fregoso, E., Palafox, A. & Moreles, M.A. (2020) Initializing Cross-Gradients Joint Inversion of Gravity and Magnetic Data with a Bayesian Surrogate Gravity Model. *Pure Appl. Geophys.*, **177**, 1029–1041. doi:10.1007/s00024-019-02334-w

Fukuda, J. & Johnson, K.M. (2010) Mixed linear—non-linear inversion of crustal deformation data: Bayesian inference of model, weighting and regularization parameters. *Geophysical Journal International*, **181**, 1441–1458. doi:10.1111/j.1365-246X.2010.04564.x

Galetti, E. & Curtis, A. (2018) Transdimensional Electrical Resistivity Tomography. *Journal of Geophysical Research: Solid Earth*, **123**, 6347–6377. doi:https://doi.org/10.1029/2017JB015418

Galley, C.G., Lelièvre, P.G. & Farquharson, C.G. (2020) Geophysical inversion for 3D contact surface geometry. *GEOPHYSICS*, **85**, K27–K45, Society of Exploration Geophysicists. doi:10.1190/geo2019-0614.1

Gamerman, D. & Lopes, H.F. (2006) *Markov Chain Monte Carlo: Stochastic Simulation for Bayesian Inference, Second Edition*, 2nd edition., Boca Raton: Chapman and Hall/CRC.

Geng, M., Ali, M.Y., Fairhead, J.D., Bouzidi, Y. & Barkat, B. (2020) Morphology of the basement and Hormuz salt distribution in offshore Abu Dhabi from constrained 3-D inversion of gravity and magnetic data. *Tectonophysics*, **791**, 228563. doi:10.1016/j.tecto.2020.228563

Geyer, C.J. (1991) Markov Chain Monte Carlo Maximum Likelihood, Interface Foundation of North America. Retrieved from http://conservancy.umn.edu/handle/11299/58440

Ghalenoei, E., Dettmer, J., Ali, M.Y. & Kim, J.W. (2021a) Gravity and magnetic joint inversion for basement and salt structures with the reversible-jump algorithm. *Geophysical Journal International*. doi:10.1093/gji/ggab251

Ghalenoei, E., Dettmer, J., Ali, M.Y. & Kim, J.W. (2021b) Joint Gravity and Magnetic Inversion with Trans-Dimensional Alpha Shape and Noise Models.

Ghalenoei, E., Dettmer, J., Ali, M.Y. & Kim, J.W. (2021c) Trans-Dimensional Gravity and Magnetic Joint Inversion for 3-D Earth. doi:under-review

Gilks, W.R., Richardson, S. & Spiegelhalter, D. (Eds.). (1995) *Markov Chain Monte Carlo in Practice*, 1st edition., Boca Raton, Fla: Chapman and Hall/CRC.

Green, P.J. (1995) Reversible jump Markov chain Monte Carlo computation and Bayesian model determination. *Biometrika*, **82**, 711–732. doi:10.1093/biomet/82.4.711

Gross, L. (2019) Weighted cross-gradient function for joint inversion with the application to regional 3-D gravity and magnetic anomalies. *Geophysical Journal International*, **217**, 2035–2046. doi:10.1093/gji/ggz134

Hajian, A., Zomorrodian, H., Styles, P., Greco, F. & Lucas, C. (2012) Depth estimation of cavities from microgravity data using a new approach: the local linear model tree (LOLIMOT). *Near Surface Geophysics*, **10**, 221–234. doi:10.3997/1873-0604.2011039

Hastings, W.K. (1970) Monte Carlo sampling methods using Markov chains and their applications. *Biometrika*, **57**, 97–109, Oxford Academic. doi:10.1093/biomet/57.1.97

Hawkins, R. & Sambridge. (2015) Geophysical imaging using trans-dimensional trees. *Geophys J Int*, **203**, 972–1000. doi:10.1093/gji/ggv326

Hightower, E., Gurnis, M. & Van Avendonk, H. (2020) A Bayesian 3-D linear gravity inversion for complex density distributions: application to the Puysegur subduction system. *Geophysical Journal International*, **223**, 1899–1918. doi:10.1093/gji/ggaa425

Hinze, W.J., Frese, R.R.B. von & Saad, A.H. (2013) *Gravity and Magnetic Exploration: Principles, Practices, and Applications*, Cambridge University Press.

Hodgson, R.A. (1965) Genetic and Geometric Relations Between Structures in Basement and Overlying Sedimentary Rocks, with Examples from Colorado Plateau and Wyoming. *AAPG Bulletin*, **49**, 935–949, GeoScienceWorld. doi:10.1306/A6633684-16C0-11D7-8645000102C1865D

Hudec, M.R. & Jackson, M.P.A. (2007) Terra infirma: Understanding salt tectonics. *Earth-Science Reviews*, **82**, 1–28. doi:10.1016/j.earscirev.2007.01.001

Izquierdo, K., Lekić, V. & Montési, L.G.J. (2020) A Bayesian approach to infer interior mass anomalies from the gravity data of celestial bodies. *Geophysical Journal International*, **220**, 1687–1699. doi:10.1093/gji/ggz544

Jackson, M.P.A. & Hudec, M.R. (2017) *Salt Tectonics: Principles and Practice*, Cambridge: Cambridge University Press. doi:10.1017/9781139003988

Jaynes, E.T. (2003) *Probability Theory: The Logic of Science*. (G. L. Bretthorst, Ed.), Cambridge, UK ; New York, NY: Cambridge University Press.

Jiang, F., Wu, J. & Wang, J. (2008) Joint inversion of gravity and magnetic data for a two-layer model. *Appl. Geophys.*, **5**, 331–339. doi:10.1007/s11770-008-0042-2

Johnson, J., Douze, M. & Jégou, H. (2017) Billion-scale similarity search with GPUs. *arXiv:1702.08734 [cs]*. Retrieved from http://arxiv.org/abs/1702.08734

Johnson, N.L., Kotz, S. & Balakrishnan, N. (1995) *Continuous Univariate Distributions, Vol. 2*, 2nd edition., New York: Wiley-Interscience.

Jorgensen, G.J. & Kisabeth, J.L. (2000) Joint 3D inversion of gravity, magnetic and tensor gravity fields for imaging salt formations in the deepwater Gulf of Mexico. in *SEG Technical Program Expanded Abstracts 2000* SEG Technical Program Expanded Abstracts, Vols 1-0, pp. 424–426, Society of Exploration Geophysicists. doi:10.1190/1.1816085

Kabirzadeh, H., Ali, M.Y., Lee, G.H. & Kim, J.W. (2021) Determining Infracambrian Hormuz Salt and Basement Structures Offshore Abu Dhabi by Joint Analysis of Gravity and Magnetic Anomalies. *SPE Reservoir Evaluation & Engineering*, **24**, 238–249. doi:10.2118/203826-PA

Kabirzadeh, H., Kim, J.W., Sideris, M.G., Vatankhah, S. & Kwon, Y.K. (2019) Coupled inverse modelling of tight CO2 reservoirs using gravity and ground deformation data. *Geophysical Journal International*, **216**, 274–286. doi:10.1093/gji/ggy424

Kamm, J., Lundin, I.A., Bastani, M., Sadeghi, M. & Pedersen, L.B. (2015) Joint inversion of gravity, magnetic, and petrophysical data — A case study from a gabbro intrusion in Boden, Sweden. *GEOPHYSICS*, **80**, B131–B152, Society of Exploration Geophysicists. doi:10.1190/geo2014-0122.1

Khattab, M.M. (1995) Interpretation of magnetic and gravity surveys in the southern Arabian Gulf, the Strait of Hormuz, and the northwesternmost Gulf of Oman: implications of pre-Permian basement tectonics. *Marine Geology*, **123**, 105–116. doi:10.1016/0025-3227(95)80007-X

Kolb, J.M. & Lekić, V. (2014) Receiver function deconvolution using transdimensional hierarchical Bayesian inference. *Geophysical Journal International*, **197**, 1719–1735. doi:10.1093/gji/ggu079

Krahenbuhl, R. & Li, Y. (2009) Hybrid optimization for lithologic inversion and time-lapse monitoring using a binary formulation. *GEOPHYSICS*, **74**, I55–I65. doi:10.1190/1.3242271

Krahenbuhl, R.A. & Li, Y. (2005) Inversion of gravity data using a binary formulation. *Geophysical Journal International*, **167**, 543–556. doi:10.1111/j.1365-246X.2006.03179.x

Last, B. & Kubik, K. (1983) Compact gravity inversion. *Geophysics*, **48**, 713–721. doi:10.1190/1.1441501

Lee, K.B. & Sung, S.A. (2014) Autoregressive Cholesky Factor Modeling for Marginalized Random Effects Models. *Communications for Statistical Applications and Methods*, **21**, 169–181, The Korean Statistical Society, and Korean International Statistical Society.

Lelièvre, P.G., Barnoud, A., Niess, V., Cârloganu, C., Cayol, V. & Farquharson, C.G. (2019) Joint inversion methods with relative density offset correction for muon tomography and gravity data, with

application to volcano imaging. *Geophysical Journal International*, **218**, 1685–1701. doi:10.1093/gji/ggz251

Lelièvre, P.G. & Farquharson, C.G. (2013) Gradient and smoothness regularization operators for geophysical inversion on unstructured meshes. *Geophysical Journal International*, **195**, 330–341. doi:10.1093/gji/ggt255

Li & Oldenburg, D. (1996) 3-D inversion of magnetic data. *GEOPHYSICS*, **61**, 394–408. doi:10.1190/1.1443968

Li & Oldenburg, D. (1998) 3-D inversion of gravity data. *GEOPHYSICS*, **63**, 109–119, Society of Exploration Geophysicists. doi:10.1190/1.1444302

Li & Oldenburg, D.W. (2003) Fast inversion of large-scale magnetic data using wavelet transforms and a logarithmic barrier method. *Geophysical Journal International*, **152**, 251–265. doi:10.1046/j.1365-246X.2003.01766.x

Li, Y. & Oldenburg, D. (1998) 3-D inversion of gravity data. *Geophysics*, **63**, 109–119. doi:10.1190/1.1444302

Lin, W. & Zhdanov, M.S. (2018) Joint multinary inversion of gravity and magnetic data using Gramian constraints. *Geophysical Journal International*, **215**, 1540–1557. doi:10.1093/gji/ggy351

Lines, L.R. & Treitel, S. (1984) A Review of Least-Squares Inversion and Its Application to Geophysical Problems*. *Geophysical Prospecting*, **32**, 159–186. doi:10.1111/j.1365-2478.1984.tb00726.x

Luo, X. (2010) Constraining the shape of a gravity anomalous body using reversible jump Markov chain Monte Carlo. *Geophys J Int*, **180**, 1067–1079. doi:10.1111/j.1365-246X.2009.04479.x

Maag, E. & Li, Y. (2018) Discrete-valued gravity inversion using the guided fuzzy c-means clustering technique. *GEOPHYSICS*, **83**, G59–G77, Society of Exploration Geophysicists. doi:10.1190/geo2017-0594.1

Maag-Capriotti, E. & Li, Y. (2019) Parameter selection workflow for a discrete-valued gravity inversion with guided fuzzy c-means clustering. in *International Workshop on Gravity, Electrical & Magnetic Methods and Their Applications, Xi'an, China, 19?22 May 2019* SEG Global Meeting Abstracts, Vols 1-0, pp. 444–447, Society of Exploration Geophysicists and Chinese Geophysical Society. doi:10.1190/GEM2019-113.1

MacKay, D.J.C. (2003) *Information Theory, Inference and Learning Algorithms*, 1 edition., Cambridge, UK ; New York: Cambridge University Press.

Malinverno, A. (2002) Parsimonious Bayesian Markov chain Monte Carlo inversion in a nonlinear geophysical problem. *Geophysical Journal International*, **151**, 675–688. doi:10.1046/j.1365-246X.2002.01847.x

Malinverno, A. & Briggs, V.A. (2004) Expanded uncertainty quantification in inverse problems: Hierarchical Bayes and empirical Bayes. *GEOPHYSICS*, **69**, 1005–1016, Society of Exploration Geophysicists. doi:10.1190/1.1778243

Martinez, C., Li, Y., Krahenbuhl, R. & Braga, M. (2010) 3D Inversion of Airborne Gravity Gradiomentry For Iron Ore Exploration In Brazil, Presented at the 2010 SEG Annual Meeting, Society of Exploration Geophysicists. Retrieved from https://www.onepetro.org/conference-paper/SEG-2010-1753

Martinez, C., Li, Y., Krahenbuhl, R. & Braga, M.A. (2013) 3D inversion of airborne gravity gradiometry data in mineral exploration: A case study in the Quadrilátero Ferrífero, Brazil. *GEOPHYSICS*, **78**, B1–B11, Society of Exploration Geophysicists. doi:10.1190/geo2012-0106.1

McKenzie, D. (1978) Some remarks on the development of sedimentary basins. *Earth and Planetary Science Letters*, **40**, 25–32. doi:10.1016/0012-821X(78)90071-7

Menke, W. (2012) *Geophysical Data Analysis: Discrete Inverse Theory: MATLAB Edition*, 3 edition., Academic Press.

Metropolis, N., Rosenbluth, A.W., Rosenbluth, M.N., Teller, A.H. & Teller, E. (1953) Equation of State Calculations by Fast Computing Machines. *The Journal of Chemical Physics*, **21**, 1087–1092. doi:10.1063/1.1699114

Michelini, A. (1995) An adaptive-grid formalism for traveltime tomography. *Geophysical Journal International*, **121**, 489–510. doi:10.1111/j.1365-246X.1995.tb05728.x

Mojiri, A., Waghei, Y., Sani, H.R.N. & Borzadaran, G.R.M. (2018) The stationary regions for the parameter space of unilateral second-order spatial AR model. *Random Operators and Stochastic Equations*, **26**, 185–191, De Gruyter. doi:10.1515/rose-2018-0017

Moral, P.D., Doucet, A. & Jasra, A. (2006) Sequential Monte Carlo samplers. *Journal of the Royal Statistical Society: Series B (Statistical Methodology)*, **68**, 411–436. doi:10.1111/j.1467-9868.2006.00553.x

Mustać, M. & Tkalčić, H. (2016) Point source moment tensor inversion through a Bayesian hierarchical model. *Geophysical Journal International*, **204**, 311–323. doi:10.1093/gji/ggv458

O'Brien, G.D. (1968) Survey of Diapirs and Diapirism1. in *Diapirism and Diapirs: a symposium* eds. Braunstein, J. & O'Brien, G.D., Vol. 8, p. 0, American Association of Petroleum Geologists. doi:10.1306/M8361C1

Oldenburg, D.W. & Li, Y. (1994) Inversion of induced polarization data. *GEOPHYSICS*, **59**, 1327–1341, Society of Exploration Geophysicists. doi:10.1190/1.1443692

Pallero, J.L.G., Fernández-Martínez, J.L., Bonvalot, S. & Fudym, O. (2015) Gravity inversion and uncertainty assessment of basement relief via Particle Swarm Optimization. *Journal of Applied Geophysics*, **116**, 180–191. doi:10.1016/j.jappgeo.2015.03.008

Pallero, J.L.G., Fernández-Martínez, J.L., Bonvalot, S. & Fudym, O. (2017) 3D gravity inversion and uncertainty assessment of basement relief via Particle Swarm Optimization. *Journal of Applied Geophysics*, **139**, 338–350. doi:10.1016/j.jappgeo.2017.02.004

Palumbo, F., Main, I.G. & Zito, G. (1999) The thermal evolution of sedimentary basins and its effect on the maturation of hydrocarbons. *Geophys J Int*, **139**, 248–260, Oxford Academic. doi:10.1046/j.1365-246X.1999.00877.x

Piana Agostinetti, N., Giacomuzzi, G. & Malinverno, A. (2015) Local three-dimensional earthquake tomography by trans-dimensional Monte Carlo sampling. *Geophys J Int*, **201**, 1598–1617. doi:10.1093/gji/ggv084

Pilia, S., Jackson, J.A., Hawkins, R., Kaviani, A. & Ali, M.Y. (2020) The Southern Zagros Collisional Orogen: New Insights From Transdimensional Trees Inversion of Seismic Noise. *Geophysical Research Letters*, **47**, e2019GL086258. doi:10.1029/2019GL086258

Pilkington, M. (2006) Joint inversion of gravity and magnetic data for two-layer models. *GEOPHYSICS*, **71**, L35–L42, Society of Exploration Geophysicists. doi:10.1190/1.2194514

Pizlo, Z. (2001) Perception viewed as an inverse problem. *Vision Research*, **41**, 3145–3161. doi:10.1016/S0042-6989(01)00173-0

Portniaguine, O. & Zhdanov, M.S. (2002) 3-D magnetic inversion with data compression and image focusing. *GEOPHYSICS*, **67**, 1532–1541, Society of Exploration Geophysicists. doi:10.1190/1.1512749

Ray, A. (2021) Bayesian inversion using nested trans-dimensional Gaussian processes. *Geophysical Journal International*, **226**, 302–326. doi:10.1093/gji/ggab114

Ray, A., Kaplan, S., Washbourne, J. & Albertin, U. (2018) Low frequency full waveform seismic inversion within a tree based Bayesian framework. *Geophysical Journal International*, **212**, 522–542. doi:10.1093/gji/ggx428

Ray, A., Key, K., Bodin, T., Myer, D. & Constable, S. (2014) Bayesian inversion of marine CSEM data from the Scarborough gas field using a transdimensional 2-D parametrization. *Geophysical Journal International*, **199**, 1847–1860. doi:10.1093/gji/ggu370

Reis, D.S., Stedinger, J.R. & Martins, E.S. (2005) Bayesian generalized least squares regression with application to log Pearson type 3 regional skew estimation. *Water Resources Research*, **41**. doi:10.1029/2004WR003445

Rücker, C., Günther, T. & Spitzer, K. (2006) Three-dimensional modelling and inversion of dc resistivity data incorporating topography — I. Modelling. *Geophysical Journal International*, **166**, 495–505. doi:10.1111/j.1365-246X.2006.03010.x

Salem, A. & Ali, M.Y. (2016) Mapping basement structures in the northwestern offshore of Abu Dhabi from high-resolution aeromagnetic data. *Geophysical Prospecting*, **64**, 726–740. doi:10.1111/1365-2478.12266

Sambridge. (2014) A Parallel Tempering algorithm for probabilistic sampling and multimodal optimization. *Geophys J Int*, **196**, 357–374. doi:10.1093/gji/ggt342

Sambridge, Braun, J. & McQueen, H. (1995) Geophysical parametrization and interpolation of irregular data using natural neighbours. *Geophys J Int*, **122**, 837–857, Oxford Academic. doi:10.1111/j.1365-246X.1995.tb06841.x

Sambridge, Gallagher, K., Jackson, A. & Rickwood, P. (2006a) Trans-dimensional inverse problems, model comparison and the evidence. *Geophys J Int*, **167**, 528–542. doi:10.1111/j.1365-246X.2006.03155.x

Sambridge, Gallagher, K., Jackson, A. & Rickwood, P. (2006b) Trans-dimensional inverse problems, model comparison and the evidence. *Geophysical Journal International*, **167**, 528–542. doi:10.1111/j.1365-246X.2006.03155.x

Sambridge, M. & Mosegaard, K. (2002) Monte Carlo Methods in Geophysical Inverse Problems. *Reviews of Geophysics*, **40**, 3-1-3–29. doi:https://doi.org/10.1029/2000RG000089

Shi, Q., Wei, S. & Chen, M. (2018) An MCMC multiple point sources inversion scheme and its application to the 2016 Kumamoto Mw 6.2 earthquake. *Geophysical Journal International*, **215**, 737–752. doi:10.1093/gji/ggy302

Shirman, B., Rybakov, M., Beyth, M., Mushkin, A. & Ginat, H. (2015) Deep structure of the Mount Amram igneous complex, interpretation of magnetic and gravity data. *Geophys J Int*, **200**, 1362–1373, Oxford Academic. doi:10.1093/gji/ggu461

Shumway, R.H. & Stoffer, D.S. (2000) *Time Series Analysis and Its Applications*. Springer Texts in Statistics, New York: Springer-Verlag. doi:10.1007/978-1-4757-3261-0

Silva Dias, F.J.S., Barbosa, V.C.F. & Silva, J.B.C. (2011) Adaptive learning 3D gravity inversion for salt-body imaging. *GEOPHYSICS*, **76**, I49–I57, Society of Exploration Geophysicists. doi:10.1190/1.3555078

Steininger, G., Dettmer, J., Dosso, S.E. & Holland, C.W. (2013) Trans-dimensional joint inversion of seabed scattering and reflection data. *The Journal of the Acoustical Society of America*, **133**, 1347–1357, Acoustical Society of America. doi:10.1121/1.4789930

Stenerud, V.R., Lie, K.-A. & Kippe, V. (2009) Generalized travel-time inversion on unstructured grids. *Journal of Petroleum Science and Engineering*, **65**, 175–187. doi:10.1016/j.petrol.2008.12.030

Sun, J. & Li, Y. (2014) Adaptive Lp inversion for simultaneous recovery of both blocky and smooth features in a geophysical model. *Geophys J Int*, **197**, 882–899, Oxford Academic. doi:10.1093/gji/ggu067

Talbot, C.J. & Jackson, M.P.A. (1987) Salt Tectonics. *Scientific American*, **257**, 70–79, Scientific American, a division of Nature America, Inc.

Tarantola. (2005) *Inverse Problem Theory and Methods for Model Parameter Estimation*. Other Titles in Applied Mathematics, Society for Industrial and Applied Mathematics. doi:10.1137/1.9780898717921

Telford, W.M., Geldart, L.P. & Sheriff, R.E. (1990) *Applied Geophysics*, 2 edition., Cambridge: Cambridge University Press.

Thomas, R.J., Ellison, R., Goodenough, K.M., Roberts, N. & Allen, P.A. (2015) Salt domes of the UAE and Oman: probing eastern Arabia. doi:10.1016/j.precamres.2014.10.011

Tikhonov, A.N. & Arsenin, V.I. (1977) *Solutions of ill-posed problems*. Scripta series in mathematics, Washington : New York: Winston ; distributed solely by Halsted Press.

Uieda, L. & Barbosa, V.C.F. (2012) Robust 3D gravity gradient inversion by planting anomalous densities. *GEOPHYSICS*, **77**, G55–G66, Society of Exploration Geophysicists. doi:10.1190/geo2011-0388.1

Uieda, L. & Barbosa, V.C.F. (2017) Fast nonlinear gravity inversion in spherical coordinates with application to the South American Moho. *Geophysical Journal International*, **208**, 162–176. doi:10.1093/gji/ggw390

Vatankhah, S., Liu, S., Renaut, R.A., Hu, X. & Baniamerian, J. (2020) Improving the use of the randomized singular value decomposition for the inversion of gravity and magnetic data. *GEOPHYSICS*, **85**, G93–G107, Society of Exploration Geophysicists. doi:10.1190/geo2019-0603.1

Voronoi, G. (1908) Nouvelles applications des paramètres continus à la théorie des formes quadratiques. Deuxième mémoire. Recherches sur les parallélloèdres primitifs. *Journal für die reine und angewandte Mathematik*, **134**, 198–287.

Wu, L. (2016) Efficient modelling of gravity effects due to topographic masses using the Gauss–FFT method. *Geophysical Journal International*, **205**, 160–178. doi:10.1093/gji/ggw010

Ye, Z., Tenzer, R. & Sneeuw, N. (2018) Comparison of methods for a 3-D density inversion from airborne gravity gradiometry. *Stud Geophys Geod*, **62**, 1–16. doi:10.1007/s11200-016-0492-6

Zhao, B.B. & Chen, Y.Q. (2011) Singular value decomposition (SVD) for extraction of gravity anomaly associated with gold mineralization in Tongshi gold field, Western Shandong Uplifted Block, Eastern China. *Nonlinear Processes in Geophysics*, **18**, 103–109. doi:10.5194/npg-18-103-2011

Zhou, H., Li, L., Bjorklund, T. & Thornton, M. (2010) A comparative analysis of deformable layer tomography and cell tomography along the LARSE lines in southern California. *Geophysical Journal International*, **180**, 1200–1222. doi:10.1111/j.1365-246X.2009.04472.x

Appendix

Appendix A: Forward model equations

In this appendix, gravity and magnetic forward model equations are presented. Gravity surveying involves measuring the gravitational attraction exerted by the Earth at the surface, airborne platform, aboard a marine vessel, or in a borehole station. Anomalies in the Earth's gravitational field originate from density anomalies in the subsurface and their distance to the point of measurement.

A.1. Gravity Forward Model

The vertical component of the gravity effect related to a density anomaly $\rho(r_j)$ at coordinate $r_j(x_j, y_j, z_j)$ can be expressed by

$$g_z(r_i) = \gamma \int_{V_j} \rho(r_j) \frac{z_j - z_i}{|r_j - r_i|^3} dV_j, \qquad \text{A1}$$

where integration is over V_j, the volume actually occupied by the density anomaly, $r_i(x_i, y_i, z_i)$ is the coordinate of measured data and γ is the universal gravitational constant (6.674×10^{-11} $m^3 \cdot kg^{-1}.s^{-2}$).

A collection of 3-D prisms is often used that can approximate the volume of a body. In this way, each prism can have a different density. Therefore, the total gravity effect of the body can be predicted by a summation of the effects of all the prisms. Here, we predict gravity anomaly data with a 3-D parametrization of N_m prisms with centers (x_j, y_j, z_j), dimensions $(\Delta x_j, \Delta y_j, \Delta z_j)$ and density contrast values. The forward model is

$$\mathrm{dg}_i^{\mathrm{pre}} = \sum_{j=1}^{N_m} G_{i,j}^{g} \, \Delta\rho_j, \qquad i = 1,2,\dots,N, \qquad \text{A2}$$

where $\mathrm{dg}_i^{\mathrm{pre}}$ are gravity predicted data at station i, N is number of data, $G_{i,j}^{g}$ is the gravity kernel of the jth prism and the ith datum, and $\Delta\rho_j$ is the density contrast ($\rho_j - 2.6$ g.cm^{-3}) of the jth prism. The exact formulation for the kernel in 3-D forward modeling can be expressed as (Blakely 1995)

$$G_{i,j}^{g-3D} = \gamma \sum_{a=1}^{2} \sum_{b=1}^{2} \sum_{c=1}^{2} \mu_{abc} \left[z_k \arctan \frac{x_a y_b}{z_c R_{abc}} - x_a \log(R_{abc} + y_b) - y_b \log(R_{abc} + x_a) \right], \qquad \text{A3}$$

where $x_1 = x_i - x_j - \Delta x_j/2$ and $x_2 = x_i - x_j + \Delta x_j/2$. Similarly, it can be written for y_1, y_2, z_1, and z_2. Moreover, $R_{abc} = \sqrt{x_a^2 + y_b^2 + z_c^2}$ and $\mu_{abc} = (-1)^a (-1)^b (-1)^c$.

Masses can be treated as 2-D distributions if we assume that they are infinitely extended in one dimension (also called $2\frac{1}{2}$D model). We predict gravity anomaly data with a 2-D parametrization of N_m rectangular blocks with centers (x_j, z_j), dimensions $(\Delta x_j, \Delta z_j)$, and density contrast values. The forward model can be employed using Eq. A2. The exact formulation for $G_{i,j}^{g-2D}$ in 2-D gravity forward modeling can be expressed as (Last & Kubik 1983)

$$G_{i,j}^{g-2D} = 2\gamma\left[\left(x_i - x_j + (\Delta x_j/2)\log(r_2 r_3/r_1 r_4)\right.\right. \\ \left.\left. + w\log(r_4/r_3) - \left(z_j + \frac{\Delta z_j}{2}\right)(\theta_4 - \theta_2) + \left(z_j - \frac{\Delta z_j}{2}\right)(\theta_3 - \theta_1)\right], \quad \text{A4}$$

where

$$r_1^2 = \left(z_j - \Delta z_j/2\right)^2 + \left(x_i - x_j + \Delta x_j/2\right)^2,$$
$$r_2^2 = \left(z_j + \Delta z_j/2\right)^2 + \left(x_i - x_j + \Delta x_j/2\right)^2,$$
$$r_3^2 = \left(z_j - \Delta z_j/2\right)^2 + \left(x_i - x_j - \Delta x_j/2\right)^2,$$
$$r_4^2 = \left(z_j + \Delta z_j/2\right)^2 + \left(x_i - x_j - \Delta x_j/2\right)^2,$$
$$\theta_1 = \arctan\left(x_i - x_j + \Delta x_j/2\right)/\left(z_j - \Delta z_j/2\right),$$
$$\theta_2 = \arctan\left(x_i - x_j + \Delta x_j/2\right)/\left(z_j + \Delta z_j/2\right),$$
$$\theta_3 = \arctan\left(x_i - x_j - \Delta x_j/2\right)/\left(z_j - \Delta z_j/2\right),$$
$$\theta_4 = \arctan\left(x_i - x_j - \Delta x_j/2\right)/\left(z_j + \Delta z_j/2\right).$$

A.2. Magnetic Forward Model

The total field magnetic anomaly related to a volume of a magnetic body can be described as (Blakely 1995)

$$\mathrm{dT}_i^{\mathrm{pre}} = -C_m \widehat{\boldsymbol{F}}.\nabla_i \int_V \boldsymbol{M}.\nabla_j \frac{1}{r} dV, \quad \text{A5}$$

where $C_m = 10^{-7}$ (henry/m) in SI, $\boldsymbol{M}$ is magnetization (ampere/m), ∇ is the gradient operator, and r is distance from the measured data to element dV of the body. $\widehat{\boldsymbol{F}}$ is a unit vector in the direction of the geomagnetic field $\boldsymbol{H}$ with the intensity of H. Here, we assume that induced magnetization ($\boldsymbol{M}$) is in direction of $\boldsymbol{H}$ and equals to $\chi\boldsymbol{H}$, where χ is magnetic susceptibility of the body.

Similar to 3-D gravity forward modeling, we can describe a body in N_m number of 3-D prisms and take the sum of magnetization of each prism as

$$\mathrm{dT}_i^{\mathrm{pre}} = \sum_{j=1}^{N_m} G_{i,j}^{T} \chi_j, \qquad i = 1,2,\dots,N, \tag{A6}$$

where $\mathrm{dT}_i^{\mathrm{pre}}$ are predicted magnetic anomaly, χ_j is susceptibility value at the jth prism and $G_{i,j}^{T}$ is the magnetic kernel that can be expressed by (Blakely 1995)

$$\begin{aligned} & G_{i,j}^{T-3D} \\ & = C_m H \left[\frac{\alpha_{23}}{2} \log\left(\frac{r - x'}{r + x'}\right) \right. \\ & + \frac{\alpha_{13}}{2} \log\left(\frac{r - y'}{r + y'}\right) - \alpha_{12} \log(r + z') - \widehat{M}_x \widehat{F}_x \arctan\left(\frac{x'y'}{x'^2 + rz' + z'^2}\right) \\ & - \widehat{M}_y \widehat{F}_y \arctan\left(\frac{x'y'}{r'^2 + rz' - x'^2}\right) \\ & \left. + \widehat{M}_z \widehat{F}_z \arctan\left(\frac{x'y'}{rz'}\right) \right] \Bigg|_{x' = x_j + \frac{\Delta x_j}{2} - x_i}^{x' = x_j - \frac{\Delta x_j}{2} - x_i} \Bigg|_{y' = y_j + \frac{\Delta y_j}{2} - y_i}^{y' = y_j - \frac{\Delta y_j}{2} - y_i} \Bigg|_{z' = z_j + \frac{\Delta z_j}{2} - z_i}^{z' = z_j - \frac{\Delta z_j}{2} - z_i}, \end{aligned} \tag{A7}$$

where $\alpha_{12} = \widehat{M}_x \widehat{F}_y + \widehat{M}_y \widehat{F}_x$, $\alpha_{13} = \widehat{M}_x \widehat{F}_z + \widehat{M}_z \widehat{F}_x$, $\alpha_{23} = \widehat{M}_y \widehat{F}_z + \widehat{M}_z \widehat{F}_y$, $r^2 = x'^2 + y'^2 + z'^2$.

By representing the body into 3-D prisms, arbitrary geometry can be obtained using the inverse method to capture vector M from the magnetic measured anomaly.

In likewise fashion to the gravity forward modeling, a magnetic body can be parametrized in 2-D regular grid cells and therefore 2-D magnetic forward modeling can be written as (Telford *et al.* 1990)

$$G_{i,j}^{T-2D} = C_m H \sin 2I \sin\beta \ln\frac{r_2 r_3}{r_1 r_4} + (\cos^2 I \sin^2\beta - \sin^2 I)(\theta_1 - \theta_2 - \theta_3 + \theta_4) \tag{A8}$$

where r_i and θ_i are given in Eq. A4.

Appendix B: rjMcMC Algorithm

In this section, we give an overview of the rjMcMC algorithm to computing the prior ratio, proposal ratio, the Jacobian determinant, and the acceptance probability.

Appendix B1: Prior Ratio

According to Eq. (2.11), the prior ratio for adding $(\boldsymbol{m}_k, k) \rightarrow (\boldsymbol{m'}_{k'}, k+1)$ is

$$\left[\frac{P(\boldsymbol{m'}_{k'})}{P(\boldsymbol{m}_k)}\right]_{\text{adding}} = \frac{\left[\frac{(\Delta\rho_1\Delta\chi_1)^{-k_1'}(\Delta\rho_2\Delta\chi_2)^{-k_2'}(\Delta\rho_3\Delta\chi_3)^{-k_3'}}{\Delta k \binom{M}{3}\binom{M}{k+1}}\right]}{\left[\frac{(\Delta\rho_1\Delta\chi_1)^{-k_1}(\Delta\rho_2\Delta\chi_2)^{-k_2}(\Delta\rho_3\Delta\chi_3)^{-k_3}}{\Delta k \binom{M}{3}\binom{M}{k}}\right]}, \tag{B1}$$

after some simplifications, it yields

$$\left[\frac{P(\boldsymbol{m'}_{k'})}{P(\boldsymbol{m}_k)}\right]_{\text{adding}} = \frac{(k+1)}{(M-k)(\Delta\rho_1\Delta\chi_1)^{k_1'-k_1}(\Delta\rho_2\Delta\chi_2)^{k_2'-k_2}(\Delta\rho_3\Delta\chi_3)^{k_3'-k_3}}. \tag{B2}$$

We show that once a new child node is added, it will have only three possible rock types as sediment or salt or basement. We, therefore, can write

$$\mathrm{k'-k} = \begin{cases} k_1'-k_1=1, k_2'-k_2=0, k_3'-k_3=0, & \text{if new child node is sediment,} \\ k_1'-k_1=0, k_2'-k_2=1, k_3'-k_3=0, & \text{if new child node is salt,} \\ k_1'-k_1=0, k_2'-k_2=0, k_3'-k_3=1, & \text{if new child node is basement.} \end{cases} \tag{B3}$$

Thus, Eq. (B2) can be written as

$$\left[\frac{P(\boldsymbol{m'}_{k'})}{P(\boldsymbol{m}_k)}\right]_{\text{adding}} = \begin{cases} \dfrac{(k+1)}{(M-k)(\Delta\rho_1\Delta\chi_1)}, & \text{if new child node is sediment,} \\ \dfrac{(k+1)}{(M-k)(\Delta\rho_2\Delta\chi_2)}, & \text{if new child node is salt,} \\ \dfrac{(k+1)}{(M-k)(\Delta\rho_3\Delta\chi_3)}, & \text{if new child node is basement.} \end{cases} \tag{B4}$$

Similarly, the prior ratio for deleting $(\boldsymbol{m}_k, k) \rightarrow (\boldsymbol{m'}_{k'}, k-1)$ is

$$\left[\frac{P(\boldsymbol{m}'_{k'})}{P(\boldsymbol{m}_k)}\right]_{\text{deleting}} = \begin{cases} \dfrac{(M-k+1)(\Delta\rho_1\Delta\chi_1)}{k}, & \text{if new child node is sediment,} \\ \dfrac{(M-k+1)(\Delta\rho_2\Delta\chi_2)}{k}, & \text{if new child node is salt,} \\ \dfrac{(M-k+1)(\Delta\rho_3\Delta\chi_3)}{k}, & \text{if new child node is basement.} \end{cases} \tag{B5}$$

Finally, the prior ratio for perturbation ($k \to k$) remains constant since it is not a function of k

$$\left[\frac{P(\boldsymbol{m}'_{k'})}{P(\boldsymbol{m}_k)}\right]_{\text{perturbation}} = 1. \tag{B6}$$

Appendix B2: Proposal Ratio

Coordinates of child nodes (x, z) are driven from uniform distribution of x and z, and are independent of density contrast $(\Delta\rho)$ and susceptibility (χ). Hence, we can write

$$\frac{Q(\boldsymbol{m}_k|\boldsymbol{m}'_{k'})}{Q(\boldsymbol{m}'_{k'}|\boldsymbol{m}_k)} = \frac{Q(x, z \mid \boldsymbol{m}'_{k'})}{Q(x', z'|\boldsymbol{m}_k)} \frac{Q(\Delta\rho, \chi|\boldsymbol{m}'_{k'})}{Q(\Delta\rho', \chi'|\boldsymbol{m}_k)}, \tag{B7}$$

the probability of adding at coordinate (x'_{k+1}, z'_{k+1}) is given by

$$Q(x', z'|\boldsymbol{m}_k) = \frac{1}{M-k}\ , \tag{B8}$$

the probability of assigning a new density contrast $\Delta\rho'_{k+1}$ and new susceptibility (χ'_{k+1}) is given by

$$Q(\Delta\rho', \chi'|\boldsymbol{m}_k) = \begin{cases} \dfrac{1}{(\Delta\rho_1\Delta\chi_1)}, & \text{if new child node is sediment,} \\ \dfrac{1}{(\Delta\rho_2\Delta\chi_2)}, & \text{if new child node is salt,} \\ \dfrac{1}{(\Delta\rho_3\Delta\chi_3)}, & \text{if new child node is basement,} \end{cases} \tag{B9}$$

the probability of removing a node at coordinate (x'_{k+1}, z'_{k+1}) (reverse step)

$$Q(x, z \mid \boldsymbol{m}'_{k'}) = \frac{1}{k+1}, \tag{B10}$$

the probability of removing a density contrast and susceptibility when the node is removed (reverse step)

$$Q(\Delta\rho, \chi|\boldsymbol{m}'_{k'}) = 1. \tag{B11}$$

Inserting all Eqs. (B8), (B9), (B10), and (B11) into Eq. (B7), we have

$$\left[\frac{Q(\boldsymbol{m}_k|\boldsymbol{m'}_{k'})}{Q(\boldsymbol{m'}_{k'}|\boldsymbol{m}_k)}\right]_{\text{adding}} = \begin{cases} \dfrac{(M-k)(\Delta\rho_1\Delta\chi_1)}{(k+1)}, & \text{if new child node is sediment,} \\ \dfrac{(M-k)(\Delta\rho_2\Delta\chi_2)}{(k+1)}, & \text{if new child node is salt,} \\ \dfrac{(M-k)(\Delta\rho_3\Delta\chi_3)}{(k+1)}, & \text{if new child node is basement.} \end{cases} \tag{B12}$$

For the deleting step, the transition is to pick up a random child node from k existing nodes and remove it.

The probability of deleting at coordinate (x'_{k-1}, z'_{k-1}) is given by

$$Q(x'_{k-1}, z'_{k-1}|\boldsymbol{m}_k) = \frac{1}{k}\ , \tag{B13}$$

the probability of removing the density contrast $(\Delta\rho'_{k-1})$ and susceptibility (χ'_{k-1}) when the node is removed is given by

$$Q(\Delta\rho'_{k-1}, \chi'_{k-1}|\boldsymbol{m}_k) = 1, \tag{B14}$$

the probability of adding a node at coordinate (x_k, z_k) (reverse step)

$$Q(x_k, z_k|\boldsymbol{m'}_{k'}) = \frac{1}{M-(k-1)} = \frac{1}{M-k+1}\ , \tag{B15}$$

the probability of generating a new density contrast $(\Delta\rho_k)$ and new susceptibility (χ_k) (reverse step)

$$Q(\Delta\rho_k, \chi_k|\boldsymbol{m'}_{k'}) = \begin{cases} \dfrac{1}{(\Delta\rho_1\Delta\chi_1)}, & \text{if new child node is sediment,} \\ \dfrac{1}{(\Delta\rho_2\Delta\chi_2)}, & \text{if new child node is salt,} \\ \dfrac{1}{(\Delta\rho_3\Delta\chi_3)}, & \text{if new child node is basement.} \end{cases} \tag{B16}$$

Inserting all Eqs. (B13), (B14), (B15), and (B16) into Eq. (B7), we have

$$\left[\frac{Q(\boldsymbol{m}_k|\boldsymbol{m'}_{k'})}{Q(\boldsymbol{m'}_{k'}|\boldsymbol{m}_k)}\right]_{\text{deleting}} = \begin{cases} \dfrac{k}{(M-k+1)(\Delta\rho_1\Delta\chi_1)}, & \text{if new child node is sediment.} \\ \dfrac{k}{(M-k+1)(\Delta\rho_2\Delta\chi_2)}, & \text{if new child node is salt,} \\ \dfrac{k}{(M-k+1)(\Delta\rho_3\Delta\chi_3)}, & \text{if new child node is basement.} \end{cases} \tag{B17}$$

The perturbation step is implemented along the rjMcMC chain to perturb a current parameter by a Cauchy distribution function. As mentioned, the perturbation does not change k, and the Cauchy distribution is a symmetric proposal, i.e., $Q(\boldsymbol{m}_k|\boldsymbol{m'}_{k'}) = Q(\boldsymbol{m'}_{k'}|\boldsymbol{m}_k)$, and hence

$$\left[\frac{Q(\boldsymbol{m}_k|\boldsymbol{m'}_{k'})}{Q(\boldsymbol{m'}_{k'}|\boldsymbol{m}_k)}\right]_{\text{perturbation}} = 1. \tag{B18}$$

Interestingly, the prior ratio and proposal ratio cancel out each other for the adding step, i.e., Eqs. (B4) and (B12), and similarly for the deleting step, i.e., Eqs. (B5) and (B17) and for perturbation step, i.e., Eqs. (B6) and (B18).

Appendix B3: Jacobian Determinant

The Jacobian determinant is required to be computed when a jump happens in the model dimension, i.e., for adding and deleting steps. For the perturbation step that does not change the model size, the Jacobian determinant is unity (Bodin & Sambridge 2009). In the adding step, the transformation h between $\boldsymbol{m}_k$ and $\boldsymbol{m'}_{k'}$ can be written as

$$\boldsymbol{m'}_{k'} = h(\boldsymbol{m}_k, \boldsymbol{u}), \tag{B19}$$

or

$$(\boldsymbol{x}_k, \boldsymbol{z}_k, \boldsymbol{\Delta\rho}_k, \boldsymbol{\chi}_k, \boldsymbol{u}_x, \boldsymbol{u}_z, \boldsymbol{u}_{\Delta\rho}, \boldsymbol{u}_\chi) \rightleftharpoons (\boldsymbol{x'}_k, \boldsymbol{z'}_k, \boldsymbol{\Delta\rho'}_k, \boldsymbol{\chi'}_k, x'_{k+1}, z'_{k+1}, \Delta\rho'_{k+1}, \chi'_{k+1}) = \boldsymbol{m'}_{k'}, \tag{B20}$$

where $\boldsymbol{u} = \{\boldsymbol{u}_x, \boldsymbol{u}_z, \boldsymbol{u}_{\Delta\rho}, \boldsymbol{u}_\chi\}$ are random variables used to propose new coordinates x, z, density contrast, and susceptibility, respectively. The current child nodes stay untouched as

$$x_i = x'_i, \qquad i = 1, \dots, k, \tag{B21}$$

$$z_i = z'_i, \qquad i = 1, \dots, k, \tag{B22}$$

$$\Delta\rho_i = \Delta\rho'_i, \quad i = 1, \dots, k, \tag{B23}$$

$$\chi_i = \chi'_i, \qquad i = 1, \dots, k. \tag{B24}$$

For the case that new coordinates are driven from a discrete distribution defined on the integers $[1, 2, \dots, M - k]$, the Jacobian determinant is always unity (D. G. T. Denison *et al.* 2002). Even if, the new coordinates are driven from a uniform distribution, we can write $x'_{k+1} = u_x$, where u_x refers to a random variable between a bounded uniform distribution, i.e., $\text{Unif}(x_{\min}, x_{\max})$. Similarly, it yields

$$x'_i = u_x \qquad i = k + 1, \tag{B25}$$

$$z'_i = u_{\boldsymbol{z}} \qquad i = k + 1, \tag{B26}$$

$$\Delta\rho_i' = u_{\Delta\rho} \quad i = k+1, \tag{B27}$$

$$\chi_i' = u_{\chi} \qquad i = k+1. \tag{B28}$$

By definition, the Jacobian is a matrix with size of $k+1$ by $k+1$, that is,

$$\begin{aligned} J = \frac{\partial(\boldsymbol{m}'_{k'})}{\partial(\boldsymbol{m}_k, \boldsymbol{u})} &= \frac{\partial(\boldsymbol{x}'_k, \boldsymbol{z}'_k, \boldsymbol{\Delta\rho}'_k, \boldsymbol{\chi}'_k, x'_{k+1}, z'_{k+1}, \Delta\rho'_{k+1}, \chi'_{k+1})}{\partial(\boldsymbol{x}_k, \boldsymbol{z}_k, \boldsymbol{\Delta\rho}_k, \boldsymbol{\chi}_k, \boldsymbol{u}_x, \boldsymbol{u}_z, \boldsymbol{u}_{\Delta\rho}, \boldsymbol{u}_{\chi})} \\ &= \frac{\partial(\boldsymbol{x}'_k, \boldsymbol{z}'_k, \boldsymbol{\Delta\rho}'_k, \boldsymbol{\chi}'_k)}{\partial(\boldsymbol{x}_k, \boldsymbol{z}_k, \boldsymbol{\Delta\rho}_k, \boldsymbol{\chi}_k, \boldsymbol{u}_x, \boldsymbol{u}_z, \boldsymbol{u}_{\Delta\rho}, \boldsymbol{u}_{\chi})} \frac{\partial(x'_{k+1}, z'_{k+1}, \Delta\rho'_{k+1}, \chi'_{k+1})}{\partial(\boldsymbol{x}_k, \boldsymbol{z}_k, \boldsymbol{\Delta\rho}_k, \boldsymbol{\chi}_k, \boldsymbol{u}_x, \boldsymbol{u}_z, \boldsymbol{u}_{\Delta\rho}, \boldsymbol{u}_{\chi})}. \end{aligned} \tag{B29}$$

From Eqs. (B21), (B22), (B23), and (B24), it yields

$$\frac{\partial(\boldsymbol{x}'_k, \boldsymbol{z}'_k, \boldsymbol{\Delta\rho}'_k, \boldsymbol{\chi}'_k)}{\partial(\boldsymbol{x}_k, \boldsymbol{z}_k, \boldsymbol{\Delta\rho}_k, \boldsymbol{\chi}_k, \boldsymbol{u}_x, \boldsymbol{u}_z, \boldsymbol{u}_{\Delta\rho}, \boldsymbol{u}_{\chi})} = I, \tag{B30}$$

where I is an identity matrix, and its determinant is unity. For the second term, we know that $\frac{\partial x'_{k+1}}{\partial \boldsymbol{x}_k} = 0$, and $\frac{\partial x'_{k+1}}{\partial \boldsymbol{u}_x} = 1$, similarly, for other variables we can write

$$\frac{\partial(x'_{k+1}, z'_{k+1}, \Delta\rho'_{k+1}, \chi'_{k+1})}{\partial(\boldsymbol{x}_k, \boldsymbol{z}_k, \boldsymbol{\Delta\rho}_k, \boldsymbol{\chi}_k, \boldsymbol{u}_x, \boldsymbol{u}_z, \boldsymbol{u}_{\Delta\rho}, \boldsymbol{u}_{\chi})} = I. \tag{B31}$$

So, it turns out that for the adding step the Jacobian determinant is unity. Since Jacobian for deleting is the inverse of adding, it also yields unity. As a result, the Jacobian determinant is unity for all steps and can be ignored.

Appendix B4: Acceptance Probability

Finally, we can show the acceptance probability for all adding, deleting and perturbation steps as

$$\alpha(\boldsymbol{m}'_{k'}|\boldsymbol{m}_k) = \min\left[1, \frac{\mathcal{L}(\boldsymbol{m}'_{k'})}{\mathcal{L}(\boldsymbol{m}_k)}\right]. \tag{B32}$$

Equivalently it can be shown in log-space to avoid numerical instabilities as

$$\alpha(\boldsymbol{m}'_{k'}|\boldsymbol{m}_k) = \min[1, \exp\{\log\mathcal{L}(\boldsymbol{m}'_{k'}) - \log\mathcal{L}(\boldsymbol{m}_k)\}]. \tag{B33}$$

In general, it is acknowledged that the expression of acceptance probability is non-trivial for trans-D frameworks. In the Appendix C, we indicate a test to validate the correctness of this framework.

Appendix C: Validation of Algorithm by Sampling the Prior

A key test to indicate validation of the algorithm and the acceptance probability is to turn off the likelihood ratio by setting it to unity and let the sampler accept all steps (Brooks *et al.* 2011). The results must represent the prior defined in this study. To do so, we implemented an inversion by collecting 200,000 models in which all steps are considered as accepted transitions. The uniform prior for the number of nodes is set between 6 and 30 and the result is shown in Fig. S1-a, which represents an expected histogram as a uniform distribution. Sampled density contrasts are also plotted in Figs. S1-b and c, which represents that the sampled posterior density contrast probability distribution closely matches the input prior. Overall, three sampled histograms are reasonably consistent with the prior and give confidence that the proposed method does not violate the detailed balance and therefore will correctly sample the posterior probability distribution.

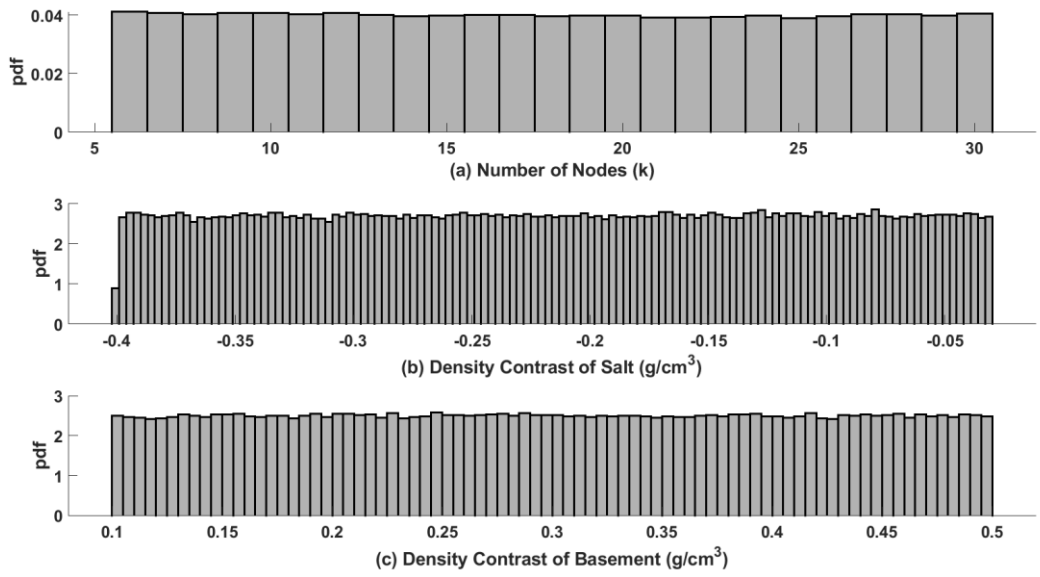

Figure S1. (a) Histogram of the number of nodes (k) showing a bounded uniform distribution over 6 and 30. The histogram of sampled density contrast for (b) salt and (c) basement.

Appendix D: Simulation with a Narrower Uniform Distribution

In this test, we present the results for a prior uniform distribution associated with salt structures with bounds as $\mathrm{Unif}(-0.4, -0.15)\ \mathrm{g/cm^3}$ that is narrower than the prior width used in the simulation of the

main article. Note that other prior distributions are kept untouched to only show the effect of this change. The posterior mean models for density contrast and susceptibility are represented in Fig. S2. The main difference between the posterior mean density contrast model obtained here and the simulation section is the compactness within salt structures. The top of the sharp salt-dome is derived at a depth around 5 km, which is 1 km deeper than the true model and around >2 km deeper than the model obtained in the simulation section. It can be then concluded that enlarging the magnitude of density contrast form $-0.03\ \mathrm{g/cm^3}$ to $-0.15\ \mathrm{g/cm^3}$ in the upper bound of the prior resulted in a more compact salt structure in deeper regions. This was reasonably expected because two bodies will approximately generate similar gravity anomalies if the denser (more compact) body is located at deeper depth (Hinze *et al.* 2013). Model uncertainties are shown in Fig. S2-c, which indicate lower CI widths comparing to the simulation section. This is owing to narrowing the prior bounds and reducing the non-uniqueness of the problem.

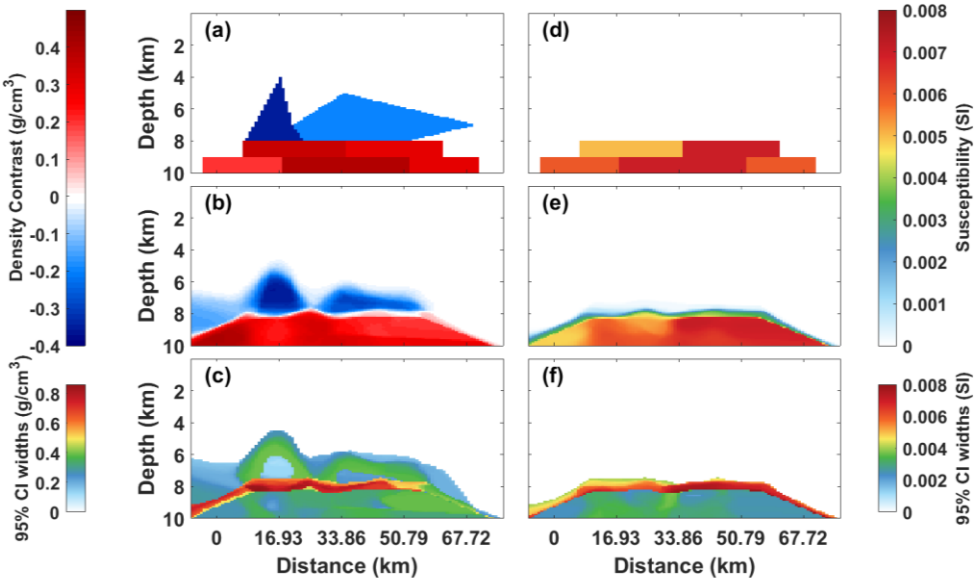

Figure S2. (a) True density contrast model for simulation, (b) posterior mean density contrast model for inversion with nested Voronoi partitioning, and (c) 95% CI widths. (d-f) The same information but for susceptibility.

Appendix E: Supportive Materials for Simulation Study

We terminated the algorithm by comparing the similarity between the posterior mean models of the first 1/3 of chains and the last 1/3 of chains. In Figs. S3-a and b, we showed that two models are similar with no significant changes, hence this approves the convergence.

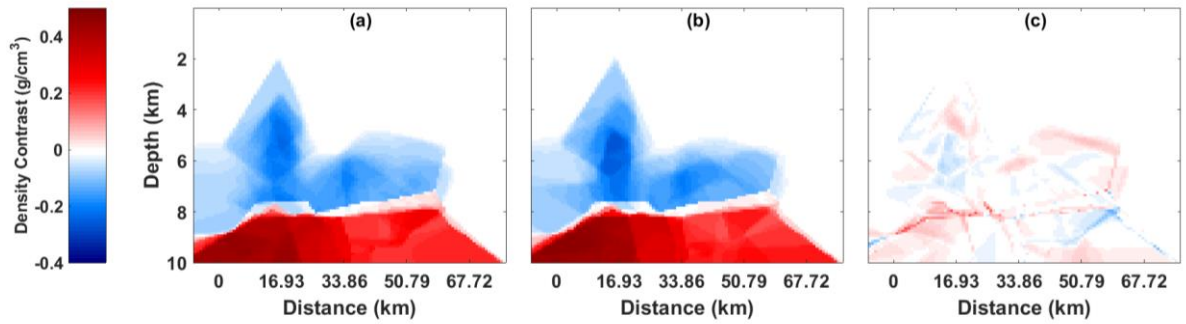

Figure S3. The posterior mean density contrast model from (a) the first 1/3 of chains, and from (b) the last 1/3 of chains. (c) The difference between (a) and (b).

Figure S4 shows 95% CI and posterior mean values along two vertical transects of X1 = 16.93 km, X2 = 41.5 km, and two horizontal transects of Z1 = 9.5 km and Z2 = 6.5 km. This figure represents that the posterior mean values mainly captured the true density contrast and susceptibility values, also the true profiles are within 95% CI.

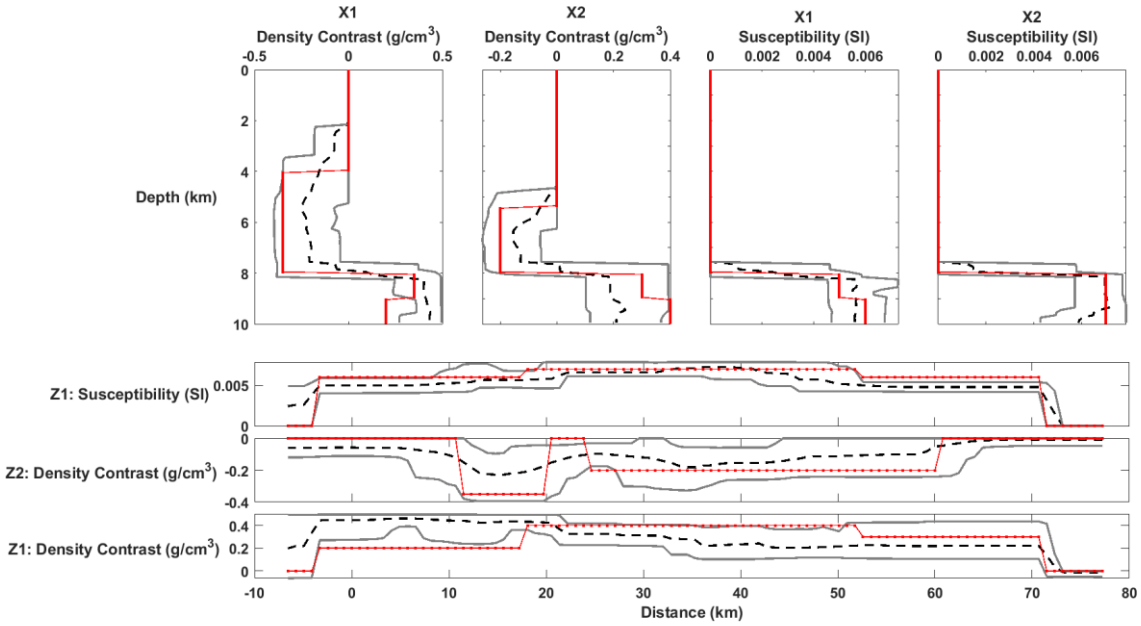

Figure S4. Each panel shows the 95% CI (gray lines), the true model (dotted red line), and the posterior mean (dashed black line). The transects (e.g., X1, X2, Z1, and Z2), and the physical properties (e.g., density contrast and susceptibility) are labeled for each panel.

Appendix F: Supportive Materials for Field Data Application

Two posterior mean models from the first and the last 1/3 of chains are compared to show the convergence of algorithm in Fig. S5. In addition, a different criterion as a convergence decision in this inversion was comparing the histogram of log-likelihood values during the first 1/3 of chains and the last 1/3 of chains. Two consistent histograms of log-likelihood values are shown in Fig. S6-a implying that the algorithm converged.

Separate histograms for sediments, salt and the basement are represented in Figs. S6-b, c, and d. These figures show a larger number of sediment nodes (peak~15) in comparison to salt (peak~9) and basement (peak~7). This is, at least in part, due to the uniform prior distributions of density contrast and susceptibility for basement and salt being wider than those for the sediment which is centered on zero. Narrowing the uniform prior distribution results in increasing the acceptance rate for new nodes. In addition, adding a new node with zero density contrast and susceptibility may not change the likelihood value, increasing the acceptance probability for new nodes. The lower number of basement nodes is likely due to the basement being constrained by both gravity and magnetic data. That is, acceptance of new and deleted nodes must meet requirements for two data sets.

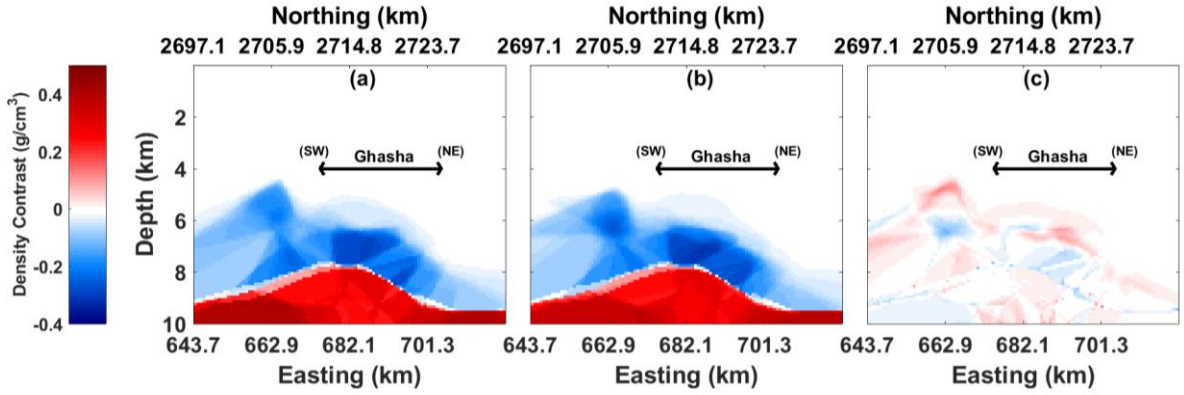

Figure S5. The posterior mean density contrast model from (a) the first 1/3 of chains, and from (b) the last 1/3 of chains. (c) The difference between (a) and (b).

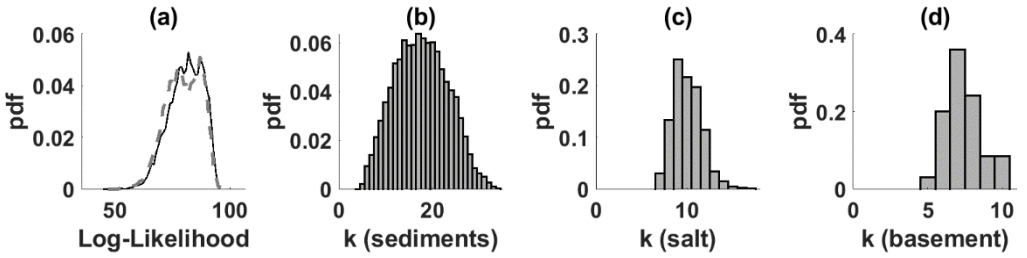

Figure S6. (a) Two consistent histograms of log-likelihood values during the first 1/3 of chains (solid line) and the last 1/3 of chains (dashed line). Histogram of number of nodes are shown separately for (b) sediments, (c) salt, and (d) the basement.

Appendix G: Demonstrating Degree of Robustness in Nested Voronoi Partitioning

Here, we evaluate the robustness of our algorithm by applying four simulated inversions from different data noise levels. To present a general view of the whole point, we only show the posterior mean density contrast models, while the derived statements can be also extended to the susceptibility model. In Fig. S7, we represented four posterior mean density contrast models each derived from a different data noise level. We can see that higher noise level results in curvier subsurface structures, from (a) to (d), respectively. This is owing to a higher data noise level allows the predicated data to fit only general features of observed data. Regardless of the details, proposed models (irregular Voronoi polygons) with different numbers of sides, angles, or orientations are more likely to be accepted in higher data noise levels. Therefore, the posterior mean model is the total average of all sampled irregular polygons approximately with the same center but different shapes, which ideally tends to be a circle in 2D or a sphere in 3D. Note that this finding is also in compliance with Ockham's razor theorem implying a solution with a simpler qualitative preference (here a circle or point mass). In addition, this test signifies the robustness of the algorithm in case of bad data (outliers from human or instrument sources) exist in the observation. The higher noise level still indicates a satisfactory resolution of general structures, without violating depths of bodies.

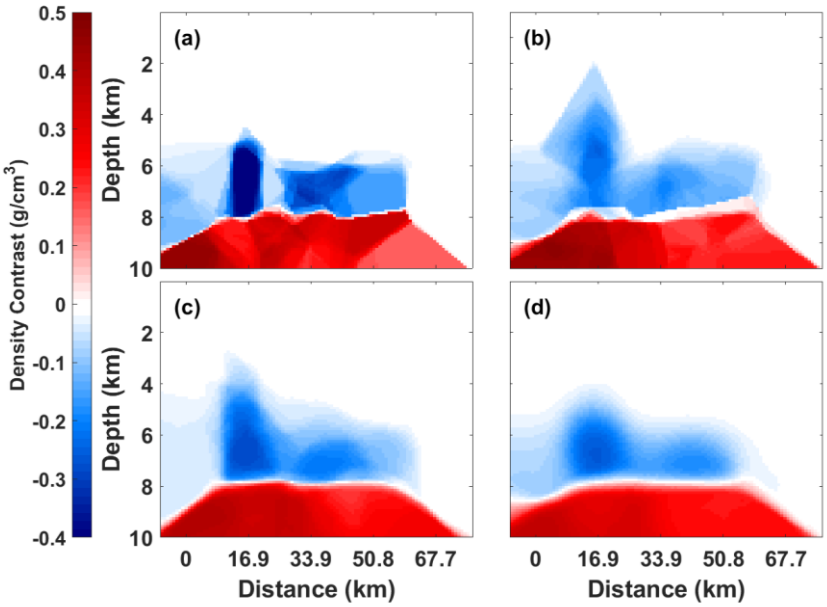

Figure S7. Posterior mean density contrast models derived from different data noise levels. (a) 2% for gravity noise and 0.3% for magnetic noise. (b) 4% for gravity noise and 1% for magnetic noise. (c) 10% for gravity noise and 4% for magnetic noise. (d) 20% for gravity noise and 7% for magnetic noise.

Appendix H: Prior for AR coefficients

An AR model must satisfy the stationary condition. We applied a preliminary test to exhibit the appropriate prior bounds of AR coefficients to meet the condition. The AR model is hierarchical and multi-resolution; therefore, the general correlation structure can be captured by the first coefficient that is the dominant coefficient. The next coefficients at orders 2 and 3 will capture the details of correlation. In order to mathematically adjust this multi-resolution model, we assumed a wider uniform prior distribution for the first coefficient comparing with the next coefficients. In our test, we set [-0.85, 0.9] as the uniform prior distribution (shown in x-axis of Fig. S8). We then uniformly examined the same distribution for the second coefficient to find which bounds meet the stationary condition. From Fig. S8, we can see that black regions violate the stationary condition; hence it must be excluded from the distribution. Although, both white and grey regions meet the condition well, but we chose the white region only since this can be expressed as a perfect uniform bounded distribution such as [-0.85, 0.1].

Here, we assumed that prior distributions are fixed for the first and the second coefficient and we applied another test for the third coefficient to see which bounds can satisfy the condition. The estimated bounds

were calculated as [-0.05, 0.01]. This distribution can provide a perfect stationary AR model. However, this is particularly problematic in the posterior distribution for the third coefficient as it might look truncated due to its too narrow width. Hence, we chose a wider uniform distribution for the third coefficient as [-0.25, 0.25]. As mentioned above, coefficients at higher orders are less effective. Therefore, modification to the bounds of the third distribution does not produce significant impact.

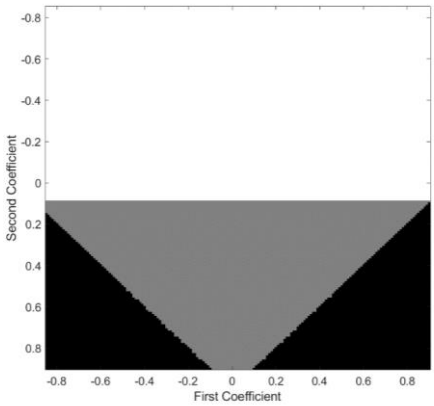

Figure S8. The white and grey regions show the realm of AR(2) that satisfies the stationary condition.

Appendix I: Validation of Algorithm

According to the acceptance probability, if we set the Likelihood a constant value, the likelihood ratio will be unity and all rjMcMC steps will be accepted. The posterior distributions in this case must represent the prior distributions. By doing this, we turn off the effect of data information and the rjMcMC algorithm unbiasedly samples the prior distribution. This test can assure the validity of the algorithm if all posterior distributions show the uniform prior distributions as we chose for the parameters in this paper.

Figure S9 shows the algorithm can sample all four AR orders with the same pdf (1/4 = 0.25) for gravity and magnetic in (a) and (e), respectively. This assures that the algorithm can unbiasedly sample each AR order. This figure also represents the posterior distributions of sampled AR coefficients that agree well with the uniform prior distributions defined for each AR coefficient in (b), (c), and (d). The marginal distributions of sampled density contrast for the salt and the basement are shown in (f) and (g), respectively, that both illustrate a uniform distribution. Finally, to validate the probabilities of proposed jumps in spatial discretization, the marginal distribution of number of nodes during rjMcMC is represented in Fig. S9-h that captured a uniform distribution between 6 and 50 nodes. We can now see that the algorithm can capture all prior distributions defined in the inversion and it completely validates the posterior distributions.

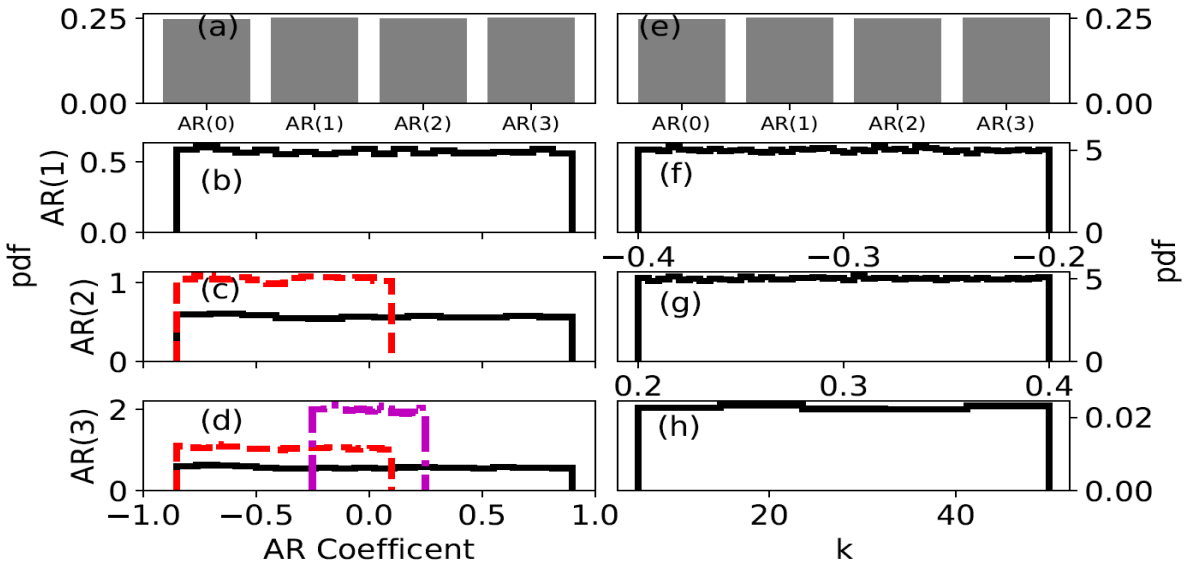

Figure S9. Marginal probability distributions of sampled orders for (a) gravity AR models and for (e) magnetic. Sampled AR coefficients for (b) AR1 (black), (c) AR2 (red), and (d) AR3 (magenta). Sampled prior distribution for density contrast for (f) the salt and for (g) the basement. (h) Marginal probability distribution for the number of nodes.

Appendix J: Rights and Permissions

RE: copyright permission

JP JOURNALS PERMISSIONS
To Emad Ghalenoei

Reply | Reply All | Forward

Tue 10/19/2021 5:49 AM

You forwarded this message on 10/20/2021 9:09 AM.

[△EXTERNAL]

Dear Emad,

Thank you for your recent email requesting permission to reuse all or part of your article in a new publication, a thesis or as part of your teaching.

As part of your copyright agreement with Oxford University Press you have retained the right, after publication, to use all or part of the article and abstract, in the preparation of derivative works, extension of the article into book-length or in other works, provided that a full acknowledgement is made to the original publication in the journal. As a result, you should not require direct permission from Oxford University Press to reuse you article.

For full details of our publication and rights policy please see the attached link to our website:

http://www.oxfordjournals.org/access_purchase/publication_rights.html

If you have any other questions or queries, please feel free to contact us.

Best wishes,

The Journals Permissions Team
Oxford University Press